$CuInSe_2$: ELECTRONIC ACTIVITIES OF GRAIN BOUNDARIES AND SOLAR CELL FABRICATION STUDIES

by

MEHMET ERAY ERKAN

Presented to the Faculty of the Graduate School of

The University of Texas at Arlington in Partial Fulfillment

of the Requirements

for the Degree of

DOCTOR OF PHILOSOPHY

THE UNIVERSITY OF TEXAS AT ARLINGTON

August 2012

Dedicated to my parents *Fatma Tülay* and *Mustafa Erkan.*

ACKNOWLEDGEMENTS

First of all, I would like to express my gratitude to my advisor Dr. Michael H.-C. Jin for his endless encouragement, guidance and patience under any circumstances during my PhD study as well as for sharing his knowledge and experience generously. My confidence for pursuing a research career is due to the tools that Dr. Jin provided to me.

I would like to thank Dr. Pranesh B. Aswath, who was my first advisor at the University of Texas at Arlington (UTA), for the invaluable experience I gained in his laboratory. I learned a lot from him on research and the experience I gained in Dr. Aswath's laboratory helped me in progressing fast in Dr. Jin's laboratory later on. Also, thank you for being a committee member. I also wish to thank Dr. Yaowu Hao, Dr. Seong Jin Koh and Dr. Muhammad N. Huda for being committee member and for sharing their valuable knowledge and time.

I must acknowledge Dr. Clifford H. Champness, Dr. Ishiang Shih and their recently graduated student Dr. Hadley F. Myers of McGill University (Canada) for providing the sample for the work presented in Chapter 3 and for answering any question I had on the sample. Appreciation also goes out to Dr. Mowafak Al-Jassim of National Renewable Energy Laboratory (NREL, USA) for the collaboration on the project presented in Chapter 3 and for connecting us with the experts in his characterization group at NREL. A big thank you goes out to Dr. Helio R. Moutinho and Dr. Manuel J. Romero of NREL for the electron backscatter diffraction (EBSD) and cathodoluminescence measurements they did, respectively, also for useful discussions on these techniques. I also thank Dr. Chun-Sheng Jiang of NREL for answering my questions on Kelvin probe force microscopy. Moreover, I would like to thank Dr. Glenn Teeter and Dr. Joel Pankow of NREL for the X-ray photoelectron spectroscopy measurement. In addition, I wish to thank Dr. Benoit Beausir of Université de Lorraine (France) for sharing his EBSD software (EBSDmcf©) and answering my questions on the software.

I would like to thank Dr. Kyungkon Kim and Mr. Chun-Young Lee of Korea Institute of Science and Technology (KIST) (Republic of Korea) for the synthesis of selenoamide, and Dr. Donggun Lim and Mr. Jong-Youb Lim of Chungju National University (Republic of Korea) for their help with the solar cell fabrication and characterization for the study presented in Chapter 4. I also would like to acknowledge Mr. Jeremiah McNatt of NASA Glenn Research Center for his help with the X-ray diffraction analysis of CdS thin films in the study presented in Chapter 5.

I must acknowledge Dr. Efstathios Meletis, the Chair of Materials Science and Engineering (MSE) Department, for his help while I was in transition between the research groups I worked at UTA. I always felt lucky that I had a chance to use a great characterization facility at UTA, Characterization Center for Materials and Biology, and I would like to thank the facility manager Dr. Jiechao Jiang and facility staff Mr. David Yan for their support with the characterization tools in the facility. Life at MSE Department would not be easy without Ms. Jennifer L. Standlee and Ms. Libia Cuauhtli; I always appreciate their support and friendship. I also would like to thank Mr. Dennis Bueno and Mr. Kevin Chambers of NanoFab at UTA for training me on the deposition tools in the cleanroom and helping me whenever I need.

I would like to thank my friends Dr. Hande Demirkıran, Mr. Jose Barona and Mr. Kipchirchir Kiprop for their support, friendship and for the fun time we had together. Moreover, I wish to thank my colleagues at Dr. Jin's laboratory, Dr. Ki-Hyun Kim, Dr. Jong-Kwan Lee, Dr. Ameena, Mr. Shenbin Daniel Wu, Mr. Soo Kim, Mr. Yu-Nung (Alex) Huang and Mr. Yacob Getachew as well as to my former colleagues at Dr. Aswath's laboratory, Dr. BoHoon Kim, Dr. Mihir Patel, Dr. Anuradha Somayaji, Dr. Ramoun Mourhatch, Dr. Xin Chen, Ms. Arunya Suresh, Ms. Hansika Parekh, Ms. Beibei Wang and Mr. Tonye Adeogba. It was very fun to work with all of you.

I have met with lots of people at UTA, mostly at MSE Department, during last six years. Other than learning research-related knowledge from them, I also had chance to learn about different cultures and different aspects of life. Unfortunately my space here does not allow me to

mention all of them name by name; however, I would like to thank, particularly, Dr. Punnapob (Poon) Punnakitikashem, Dr. Vishwas Bedekar, Dr. Liangshan Chen, Dr. Emil Zin, Mr. Alex Alphonse, Ms. Chivarat (Mook) Muangphat and Ms. Orathai (Koi) Thumthan. And, thank you many other beautiful people I have met for coloring my life; I hope I colored your lives as well.

I would like to thank the financial support provided by UTA, KIST and an industrial fund for the studies presented in Chapter 3, 4 and 5 of this dissertation, respectively.

Last but not least, I would like to thank my parents Fatma Tülay and Mustafa Erkan, my brother İbrahim Koray Erkan as well as my relatives and friends in Turkey for their endless love and support.

August 13, 2012

ABSTRACT

$CuInSe_2$: ELECTRONIC ACTIVITIES OF GRAIN BOUNDARIES AND SOLAR CELL FABRICATION STUDIES

Mehmet Eray Erkan, PhD

The University of Texas at Arlington, 2012

Supervising Professor: Michael H.-C. Jin

This dissertation is composed of three studies related to chalcopyrite solar cells. The first study is on electronic activities of grain boundaries (GBs) in $CuInSe_2$ (CIS). Despite being polycrystalline, chalcopyrite thin film solar cells have reached record power conversion efficiencies. This is against the classical understanding on the effect of GBs in semiconductor materials. Because GBs are expected to be recombination centers and barriers against the carrier flow, reducing the device efficiency. Therefore, a complete understanding on the electronic behavior of chalcopyrite GBs is missing. Moreover, the high efficiency chalcopyrite solar cells are grown with Na impurities which positively affect the performance of the solar cell, so-called *sodium effect*. Research on chalcopyrite GBs has been coupled with the effect of Na impurities, because Na has been found segregated at the GBs. The study presented in this dissertation was performed on GBs in a Na-free CIS. It is important to study the GBs in a Na-free chalcopyrite to avoid any uncontrolled effects of Na segregation at the GBs, for instance a possible Na-related secondary phase formation which would affect the conclusions drawn on the natural behavior of chalcopyrite GBs. In addition, it is known that Σ3 GBs in chalcopyrite solar cells are abundant; therefore, it is meaningful to investigate the differences between Σ3

and non- Σ3 GBs. For this purpose, Σ3, ~Σ3 and Σ9 GBs in a Bridgman-grown multicrystalline Na-free CIS wafer were identified by electron backscatter diffraction and their electronic properties were investigated by Kelvin probe force microscope and cathodoluminescence in scanning electron microscope. It is shown that the Σ3 GB is neutral and it does not behave as a recombination center, whereas once the geometry of a GB deviates from the Σ3 geometry, such as ~Σ3 and Σ9 GBs, the GB becomes charged and behaves as a recombination center. This result was concluded to be due to the increase in the amount of defects at the GB that introduce midgap states as the Σ value increases. Our results indicate that the surprising high performance seen in the polycrystalline chalcopyrite solar cells is possibly due to the abundance of electrically inactive Σ3 GBs in this material. To investigate the effect of Na on CIS GBs, projected work includes the characterization of Σ3 and non-Σ3 GBs in CIS wafers grown with increasing Na concentration. Consequently, it will be possible to answer the following questions on the impact of sodium-effect on GBs: Is there a certain Na concentration for Na to affect the GB electrical properties and how does it affect both Σ3 and non-Σ3 GBs?

In the second study, the use of selenoamide instead of direct use of H_2Se for atmospheric pressure selenization reaction is proposed and its feasibility is shown by fabricating CIS solar cells with up to 1.6% power conversion efficiency. In addition, observed In and Ga segregation towards the bottom of the CIS and CIGS thin films, respectively, are investigated through phase transformations occurring during the selenization and systematically designed annealing processes.

The third study is on the effect of flow type on the growth kinetics of CdS thin films deposited by chemical bath deposition. CdS thin films are deposited on glass substrates under turbulent and laminar flow conditions only by changing the substrate's alignment with respect to the bottom of the beaker in unstirred bath. It is shown that the flow condition of the bath does not change the optical and structural properties of CdS; however, deposition under laminar flow is explained to be diffusion-limited, whereas it is feed-limited under turbulent flow.

TABLE OF CONTENTS

LIST OF ILLUSTRATIONS

Figure Page

LIST OF TABLES

CHAPTER 1

INTRODUCTION AND BACKGROUND

1.1 Introduction

This dissertation is composed of six chapters, three of which present separate studies on chalcopyrite solar cells. In this subsection (1.1 Introduction), an overview of all chapters is given, and in the next subsection 1.2 Background, general background information about chalcopyrite materials and solar cells are provided. Detailed background information on the three studies presented in this dissertation is included in their respective chapters.

Principles of experimental methods are provided in Chapter 2. The methods used for sample preparation are explained in the subsection 2.1 Principles of Material Preparation Methods; whereas the working principles of the characterization tools used are explained in subsection 2.2 Principles of Material Characterization Methods.

Chapter 3 presents a study on the electronic activities of grain boundaries (GBs) in chalcopyrites. Polycrystalline chalcopyrite thin film solar cells have reached ~20% power conversion efficiency [1, 2] in the laboratory, and they have the highest efficiency among other thin film solar cell technologies prepared in the laboratory [3]. Obtaining a high efficiency device from a polycrystalline semiconductor is surprising according to the classical view on semiconductor GBs [4-6]. Because GBs are expected to affect carrier transport and behave as recombination centers in the semiconductor due to the extra electronic states form by the defects at GBs [5, 7]. Therefore, there is a research interest on explaining this unexpected electronic behavior of chalcopyrite GBs. Moreover, the high efficiency chalcopyrite solar cells are grown with Na impurities which diffuse from the soda-lime glass (SLG) substrate into the chalcopyrite film during high temperature growth (typically ≥ 500 °C). Na impurities have a

positive impact on the device performance, so-called *sodium effect*, through increasing the open circuit voltage of the solar cell. Experimental and theoretical studies found that Na segregates to the GBs [8-10]. Therefore, the existence of the Na impurities at the GBs needs to be taken into account for a complete understanding on the electronic behavior of chalcopyrite GBs. In this study, Σ3, ~Σ3 and Σ9 GBs in a Bridgman-grown multicrystalline Na-free $CuInSe_{2.1}$ (CIS) wafer was investigated. This was necessary to study the electronic properties of chalcopyrite GBs in their natural form by preventing any uncontrolled effect of Na on the electronic properties of GBs. For example, a Na-related secondary phase can segregate at the GBs as was theoretically predicted [11]. The GBs in the Na-free CIS wafer were identified crystallographically by electron backscatter diffraction measurement and their electronic properties were studied by Kelvin probe force microscopy and cathodoluminescence in scanning electron microscopy. It is shown that the electronic behavior of the GBs in a Na-free CIS wafer is governed by the extent of defects existing at a particular GB. Because the Σ3 GB is found to be neutral, i.e. does not have a band bending over it, and does not behave as a recombination center. As the Σ value deviates from Σ3, such as in ~Σ3 GB, or increases, such as Σ9, the GB becomes gradually charged, i.e. GB band bending occurs, and behaves as a recombination center.

The purpose of the study presented in Chapter 4 is two-fold: demonstrating the feasibility of using selenoamide as a Se source for selenization reaction and studying the phase transformations taking place during selenization. A common method for fabrication of chalcopyrite absorber is selenization which consists of reaction of pre-deposited metal layers in a Se atmosphere at high temperature (typically ~550 °C). H_2Se is a commonly used gas for the selenization reaction. However, it is highly toxic and creates transportation and handling issues [12]. In this study, the use chalcogen amides in general, and particularly selenoamide, are proposed instead of direct use of H_2Se. Selenoamide used in this study is a solid compound at room temperature and liberates H_2Se upon its decomposition at ~150 °C [13]. Cu-In and In-

CuGa metal bilayers were successfully selenized forming CIS and Cu(In,Ga)Se_2 (CIGS) thin films at 400 °C in an atmospheric pressure tube furnace. Observed In and Ga segregation to the bottom of the CIS and CIGS thin films, respectively, and their re-distribution are studied and explained through the phase transformations occurring during the selenization and systematically designed annealing processes. Two different Ga concentration profiles resulted in the CIGS films after selenization and post-selenization annealing are discussed in terms of their possible effects on solar cell performance. Finally, up to 1.6% power conversion efficiency is demonstrated in the first batch of CIS solar cells prepared with SLG/Mo/CIS/CdS/ZnO/ZnO:Ga/Al structure.

The study presented in Chapter 5 is on chemical bath deposition (CBD) of CdS thin films (CBD-CdS). *p*-*n* junction of a chalcopyrite solar cell is formed by depositing ~50 nm thick *n*-type CdS thin film onto *p*-type chalcopyrite absorber by CBD. During CBD, the solution is usually stirred to prevent unnecessary concentration gradient in the chemical bath and precipitates sticking onto the CdS film surface. Stirring rate can affect the CdS deposition kinetics by changing the hydrodynamic condition of the bath. Depending on the stirring rate thickness of the boundary layer over the substrate changes, i.e. the diffusion length of the reactants towards the substrate changes, affecting the deposition kinetics. Moreover, boundary layer type over the substrate can change between laminar and turbulent depending on the stirring rate. Nonetheless, there is no agreement on the effect of stirring rate on the deposition kinetics of CBD-CdS in the literature. In this study, CdS thin films are deposited under laminar and turbulent flow conditions only by changing the alignment of the substrate with respect the bottom of the beaker in an unstirred bath. The flow in the bath is naturally driven by placing a hot plate under the beaker. Therefore, when the substrate is aligned parallel to the bottom of the beaker turbulent flow is obtained, whereas a substrate aligned perpendicular to the bottom of the beaker is under the laminar flow condition. It is shown that while the optical and structural properties of the deposited CdS thin films do not depend on the flow type over the substrate; the

deposition rate is significantly affected by the flow, being higher when turbulent flow exits. It is concluded that while the reaction is diffusion-limited in case of laminar flow due to the laminar boundary layer over the substrate, deposition becomes feed-limited when the turbulent flow is present, increasing the CdS deposition rate.

Finally, Chapter 6 provides a summary of the three studies presented in this dissertation.

1.2 Background

1.2.1 Chalcopyrite Solar Cell Materials and Thin Film Solar Cells

$CuInSe_2$ (CIS) is a member of I-III-VI_2 semiconductor material group that crystallizes in tetragonal chalcopyrite structure (Fig 1.1). Chalcopyrite is a similar structure to sphalerite with the group I and III elements of chalcopyrite are orderly placed on the sites of the group II element of sphalerite. Chalcopyrite demonstrates tetragonal distortion, i.e. c/a is not exactly 2, due to the different strengths of the Cu-Se and In-Se bonds [12, 14]. Some of the material properties of CIS are listed in Table 1.1.

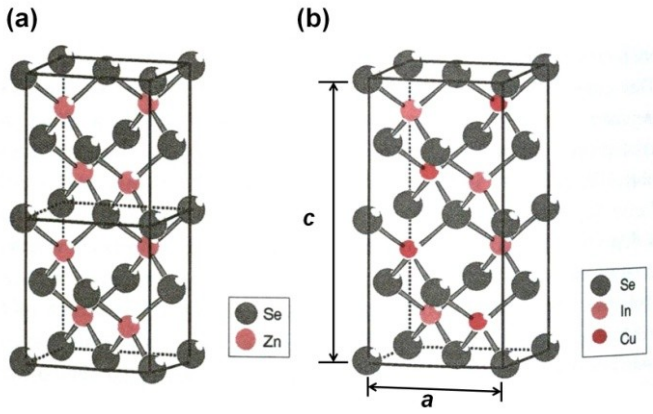

Figure 1.1 Unit cells of (a) sphalerite or zinc blende ZnSe (two unit cells) and (b) chalcopyrite $CuInSe_2$ (After Ref. [14]).

Table 1.1 Selected material properties of $CuInSe_2$ (After Ref. [12]).

Lattice constants (Å)	a = 5.78
	c = 11.62
Density (g/cm^3)	5.75
Melting temperature (°C)	986
Bandgap (eV)	1.04

In the Cu-In-Se ternary phase diagram (Fig. 1.2) CIS is located on the tie-line between Cu_2Se and In_2Se_3 together with ordered defect compounds (ODC). An ODC has the chalcopyrite crystal structure with structurally ordered intrinsic defects. Cu_2Se - In_2Se_3 pseudobinary phase diagram (Fig. 1.3) detailing the tie-line close to CIS phase shows that CIS phase does not include stoichiometric composition of 25% Cu at low temperatures. Device quality CIS thin films have 22 – 24 at.% Cu which is a composition range in the single CIS phase region at thin film growth temperatures (typically ~500°C). However, phase separation should be expected at room temperature [12, 14].

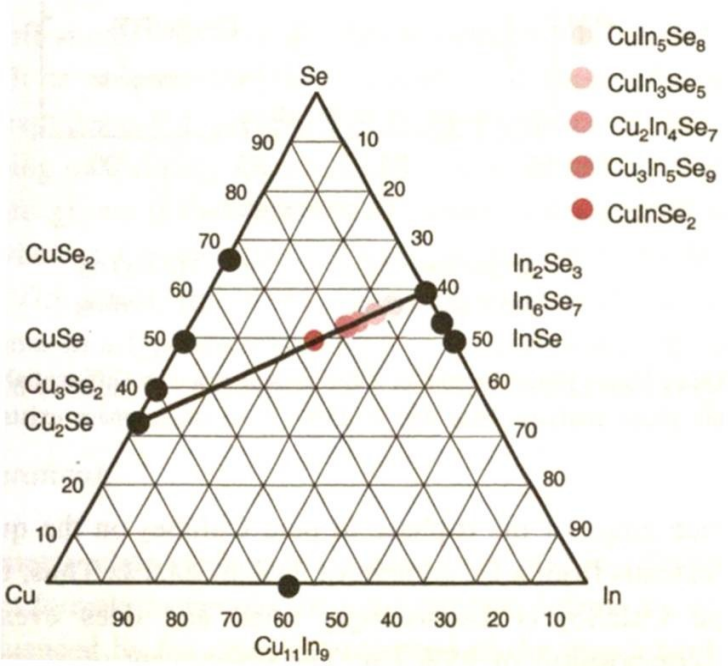

Figure 1.2 Cu-In-Se ternary phase diagram [14].

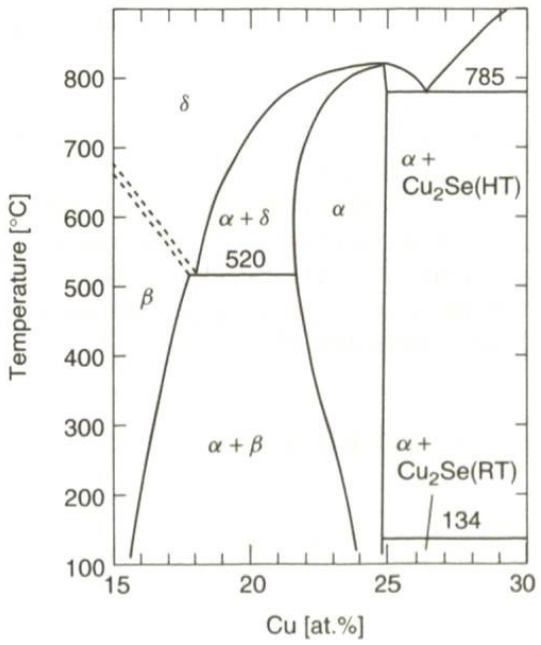

Figure 1.3 Pseudobinary Cu_2Se-In_2Se_3 equilibrium phase diagram close to chalcopyrite $CuInSe_2$ phase (α). δ: High temperature sphalerite phase. β: An ordered defect phase. RT: Room temperature. HT: High temperature.[12]

CIS has a high absorption coefficient (> 3 x 10^4/cm for 1.3 eV and higher photon energies) which makes it suitable to be used as an absorber layer in thin film solar cell applications, because 95% of the solar illumination can be absorbed within 1μm film thickness due to its high absorption coefficient. Moreover, CIS can be alloyed with other Cu-chalcopyrites, such as $CuInS_2$, $CuGaSe_2$ (CGS) and $CuGaS_2$, in any proportion, because a miscibility gap in this system does not exist. Therefore, bandgap (E_g) of the absorber layer can be engineered in a range between 1.04 eV (in CIS) to 2.4 eV (in $CuGaS_2$) (Fig. 1.4). Bandgap engineering has an importance for matching the bandgap of the absorber layer with the predicted bandgap values for high efficiency solar cells (Fig.1.5) and for fabricating tandem solar cells [12, 14].

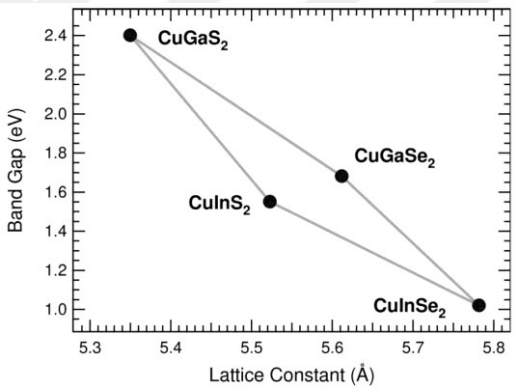

Figure 1.4 Bandgaps and lattice parameters of the $Cu(In,Ga)(Se,S)_2$ alloy system. Lines connecting the dots are guide to the eye. [15]

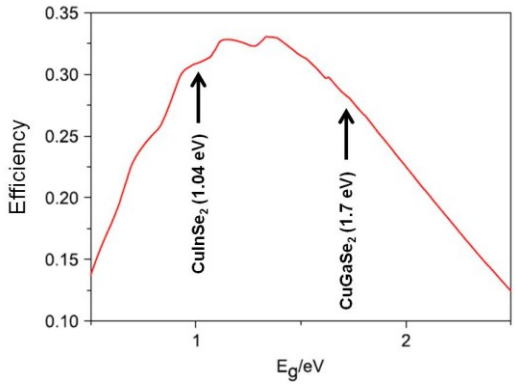

Figure 1.5 Maximum efficiency as a function of semiconductor bandgap (E_g) drawn for a *p*/*n* junction solar cell under AM1.5 illumination. After Ref. [16].

Nonetheless, the highest power conversion efficiency from a thin film chalcopyrite solar cell has been obtained by alloying CIS and CGS, i.e. $Cu(In,Ga)Se_2$ (CIGS), with a Ga/(In+Ga) ratio of typically 0.2 – 0.3. In addition, Cu/(In+Ga) ratios of the device quality CIGS thin films range between 0.7 to ~1, i.e. the film composition is Cu-poor/In-rich. The large compositional variation can be accommodated by CIGS without compromising optoelectronic properties. Because it was shown that $2V_{Cu} + In_{Cu}$ (V_{Cu}: Cu vacancy, In_{Cu}: In on Cu antisite) defect complex has a low formation energy and expected to be electrically inactive. In addition, the existence of ODC phases shown in Figure 1.2 can be explained by the $2V_{Cu} + In_{Cu}$ defect complex formation, because crystallographic ordering of this defect complex was predicted. However, Ga and Na addition to the film suppresses ODC formation and expands the chalcopyrite phase region. Because, Ga_{Cu} antisite defect has higher formation energy than In_{Cu} antisite defect, and Na can replace In_{Cu} and can also occupy V_{Cu}, resulting in a reduced tendency to form $2V_{Cu} + In_{Cu}$ defect complex [12, 14].

Device quality CIGS thin films are grown under excess Se and are *p*-type semiconductors. While CGS and Cu-rich CIS are always *p*-type, In-rich CIS can be *n*-type or *p*-type depending on the amount of Se. For instance, when an *n*-type CIS material is annealed under Se overpressure, it becomes *p*-type, and if a *p*-type CIS material is annealed under low Se pressure it becomes *n*-type. This is thought to be due to the change in the concentration of the Se vacancies, V_{Se} during annealing, because V_{Se} acts as compensating donors in *p*-type chalcopyrite films. Chalcopyrite materials are doped by native defects, and in addition to V_{Se}, a number of native defects exist. Depending on the composition of the chalcopyrite material, the defects with lowest formation energies are V_{Se}, V_{Cu}, V_{In} or V_{Ga}, Cu_{In} or Cu_{Ga}, and In_{Cu} or Ga_{Cu}. Although it is nontrivial to match the results of theoretical and experimental defect studies, Figure 1.6 shows transition energies of intrinsic defects in CIS observed in both theoretical and experimental studies [12, 14].

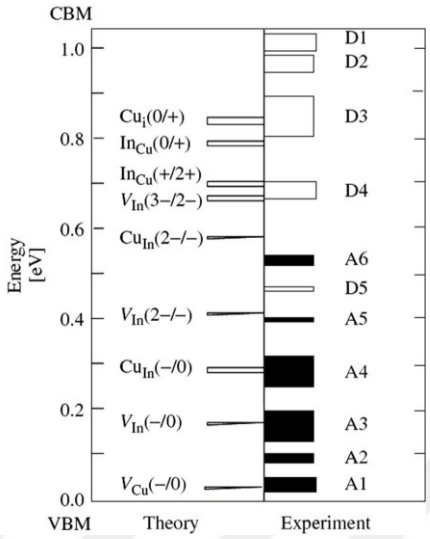

Figure 1.6 Theoretically and experimentally found transition energies of intrinsic defects in $CuInSe_2$. *V*: Vacancy, A_B: A on B antisite, Cu_i: Interstitial Cu, A: Acceptor, D: Donor, VBM: Valence band maximum, CBM: Conduction band minimum. [17]

Schematics of layers in a complete CIGS thin film solar cell and thin film CIGS module manufacturing steps can be seen in Figures 1.7a and 1.7b, respectively. CIGS solar cell fabrication begins with substrate cleaning step. The most commonly used substrate for CIGS thin film solar cells is soda-lime glass (SLG). The initial purposes of using SLG as a substrate were its low cost and the thermal coefficient match between SLG and CIGS. However, it is now well-known that Na diffusing out from SLG substrate during CIGS thin film growth at a high temperature (usually at ~550 °C) has positive effects on the solar cell performance. This is called *sodium effect* and more information on the sodium effect is given in Chapter 3 of this dissertation. Flexible substrates, such as polyimide web and stainless steel foil, are also used for CIGS solar cell fabrication, and they have the advantage of allowing continuous roll-to-roll processing and lightweight solar cell fabrication. Because Na addition to the CIGS film has become a necessity to obtain a high efficiency device, Na is incorporated into the film by other means, when a Na-free substrate is used. This can be performed by depositing a Na-containing precursor, for instance NaF with ~10 nm thickness, onto the Mo back contact layer or by co-depositing Na during CIGS deposition.

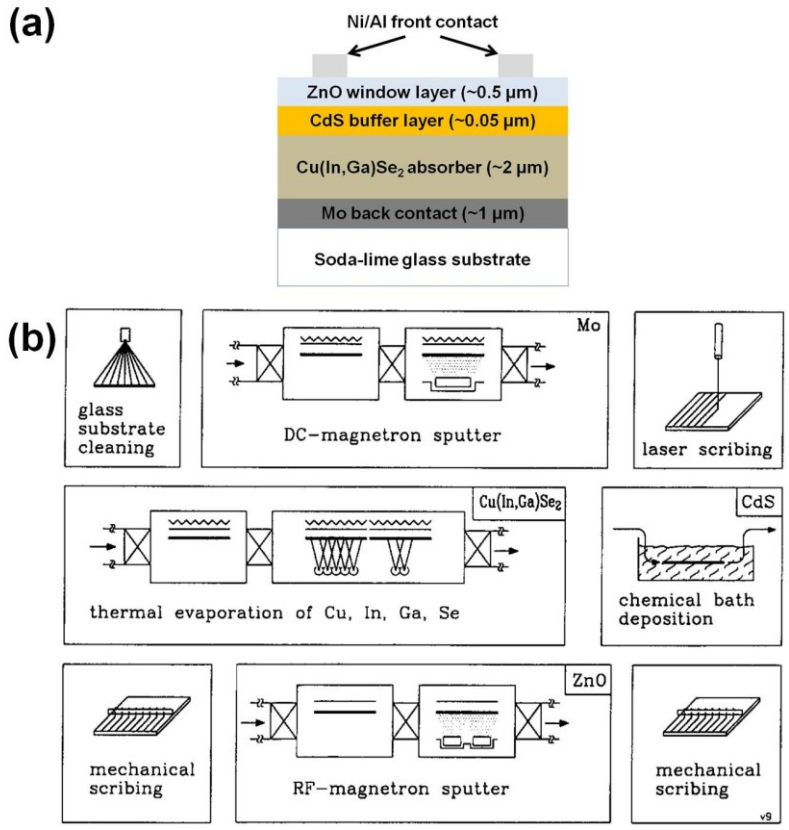

Figure 1.7 Schematics of (a) typical layers in a $Cu(In,Ga)Se_2$ (CIGS) solar cell and (b) thin film CIGS module manufacturing steps with CIGS deposition by in line evaporation [18].

Mo is a typical back contact material in CIGS solar cells which is deposited by direct current (DC) sputtering with a typical thickness of ~1 μm. Its exact thickness is determined by resistance requirements for a specific device configuration. During CIGS layer growth on Mo back-contact, $MoSe_2$ layer forms at the Mo/CIGS interface which is not detrimental for solar cell operation and, in fact, can promote an ohmic contact formation.

CIGS absorber layer can be deposited by vacuum-based methods, such as evaporation, or non-vacuum-based methods, such as electrodeposition. Absorbers prepared by vacuum-based methods have been resulted in higher efficiency solar cells than the ones prepared by non-vacuum based methods; therefore, focus will be on the vacuum-based methods in this section. Two common vacuum-based methods are co-evaporation and two-step precursor reaction process. In co-evaporation, constitutional elements are co-evaporated from

elemental sources onto a substrate heated to 450 – 600 °C. Co-evaporation process allows composition of the film to be varied through its thickness by adjusting the relative evaporation rates of the elements according to a growth scheme. For instance, a graded bandgap CIGS absorber can be deposited by varying the evaporation rates of In and Ga, because the bandgap of CIGS depends on $x \equiv$ Ga/(Ga+In) and it can be calculated by using the following empirical equation

$$E_g = 1.04 + 0.65x - 0.26x(1 - x), \tag{1.1}$$

where the bowing parameter is 0.264 and the bandgap of CIS is 1.035 eV. Se is always evaporated in excess during co-evaporation, because it has a high vapor pressure, and a lack of Se can cause loss of In or Ga due to formation of volatile In_2Se or Ga_2Se secondary phases. Although various CIGS deposition schemes can be utilized during co-evaporation, the so-called "three-stage process" has proved to yield high efficiency CIGS solar cells. The three-stage process is basically a sequential process (Fig. 1.8).

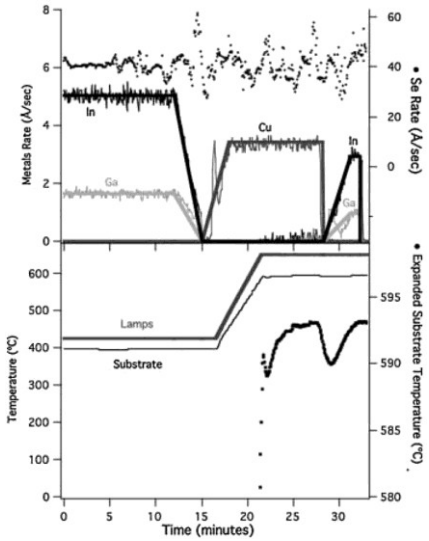

Figure 1.8 Three-stage deposition data for CIGS absorber yielded 19.9% efficient solar cell. In the upper graph, thick lines show Cu, In and Ga deposition rate setpoints and the thin lines show rate monitor data. In the lower graph, the dip in the expanded substrate temperature plot indicates the sample emissivity change when the film composition became Cu-rich at the end of the second stage [1].

In the first stage, In and Ga are co-evaporated without Cu, and Cu evaporation in the second stage brings the overall composition to Cu-rich regime, finally in the last stage the composition is brought to a Cu-poor composition by Ga and In co-evaporation. CIGS growth occurs by interdiffusion of the deposited layers during the process while Se is continuously delivered in excess to the growing film. The main asset of the three-stage process is formation of quasi-liquid Cu-Se binary phase during the second stage which behaves as a flux and favors growth of large grains.

On the other hand, a typical CIGS growth by a two-step precursor reaction process consists of selenization of pre-deposited metal layers. Metal layers can be deposited by various methods, such as physical vapor deposition methods and electrodeposition. Selenization reaction is performed by annealing the metal layers in a selenium atmosphere, such as Se vapor and H_2Se gas, at 400 – 600 °C. Alternatively, Se can also be provided as a layer deposited onto the metal layers and CIGS reaction can be performed by rapid thermal processing in an inert or Se atmosphere. The final film composition is determined by the composition of the metal layers. According to the *in situ* XRD measurements performed during CIS growth from stacked Cu-In-Se layers, CIS growth reactions start with formation of Cu-In intermetallic compounds which react with Se and form binary selenide compounds. Growth reactions proceed as follows

$$CuSe + InSe \rightarrow CuInSe_2 \quad (1.1)$$

$$1/2Cu_2Se + InSe + 1/2Se \rightarrow CuInSe_2 \quad (1.2)$$

When Ga is included in the stacked layers, the following reaction also occurs

$$1/2Cu_2Se + 1/2Ga_2Se_3 \rightarrow CuGaSe_2 \quad (1.3)$$

And, CIGS phase forms by intermixing of CIS and CGS phases. Ga accumulation close to the Mo back contact and hence a two-phase CGS/CIS formation in the resulting film is commonly

observed. Due to its faster formation rate, CIS phase forms at the top of the film where Se exists. Consequently, Ga accumulates close to the Mo back contact and the resulting film consists of CGS/CIS structure. This is explained by the higher stability of Ga-Se binary compound than that of In-Se compound. Therefore, benefits of Ga addition to CIS, such as bandgap increase, cannot be gained entirely. In fact, Ga improves the adhesion of the CIS film to the Mo back contact and results in higher solar cell performance possibly due to its structure with fewer defects. A homogenous Ga distribution, and hence uniform bandgap, in the film can be achieved by interdiffusion of CIS and CGS by annealing the film at 500 – 600 °C. Also, formation of Cu(In,Ga)(Se,S) by S incorporation to the surface of the CIGS film is a method used for increasing the bandgap and hence enhancing the open circuit voltage of a solar cell.

p-n junction is formed by depositing ~0.05 μm CdS buffer layer onto CIGS thin film by chemical bath deposition (CBD) method. Although physical vapor deposition methods can also be used for CdS deposition, CBD is preferred due to ease of depositing a conformal thin CdS film on rough CIGS surface by CBD. In addition, ammonia used in the chemical bath cleans the native oxides from the CIGS surface. More information on CBD of CdS can be found in Chapter 2 of this dissertation. In fact, there is an effort to replace CdS with a Cd-free buffer material due to increasing restrictions on Cd usage in electronic materials as well as due to the desire to use a material with a higher bandgap (E_g) than CdS (E_g = 2.4 eV) to gain short circuit current. Therefore, use of alternative buffer layers, such as Zn(S,O,OH) (E_g = 3.0 - 3.8 eV), and deposition of the ZnO ($E_g \approx$ 3.5 eV) window layer directly onto CIGS absorber without a buffer layer are two main approaches being investigated.

Doped ZnO is the most commonly used transparent contact material as window layer in CIGS solar cells for lateral current collection. Although other transparent conducting oxide materials, such as In_2O_3:Sn, can also be used for the same purpose, ZnO is cheaper, hence preferred. Radio frequency (RF) and reactive DC sputtering are common methods for depositing ZnO window layer, although chemical vapor deposition is also used. For instance,

ZnO:Al window layer can be deposited by RF sputtering from ZnO:Al_2O_3 targets or by reactive DC sputtering from Al/Zn targets in an Ar:O_2 mixture. Sheet resistance (typically 20 – 50 Ω/sq for small area cells) of the window layer depends on the specific application and controlled by its thickness (0.1 – 0.5 μm for small area cells). It is also common practice to deposit a 0.05 μm thick undoped high-resistivity ZnO (1 – 100 Ωcm) by RF sputtering before doped ZnO (resistivity: 10^{-4} – 10^{-3} Ωcm) deposition. An explanation for the beneficial effect of using undoped ZnO is reducing the undesirable effects of local electronic nonuniformities of CIGS absorber that cause high recombination current by series resistance of undoped ZnO.

A metal grid on laboratory cells is deposited by evaporation of, first, Ni (tens of nanometers) and then Al (~1 μm). Ni is deposited to avoid formation of high resistance oxide layer. Device isolation is done by removing the layers on Mo outside the cell area by mechanical scribing or laser patterning. Optionally, a ~0.1 μm thick MgF_2 can be evaporated as an anti-reflection coating. An anti-reflection coating is not used for modules, because modules are encapsulated. In addition, modules are usually manufactured without a metal grid, and instead a thicker window layer than that is used for a laboratory cell is deposited [12, 14].

1.2.2 Basic Working Principle and Characteristics of a p/n Junction Solar Cell

A solar cell can be defined as a semiconductor diode which produces electricity by utilizing the photons from the Sun [19-21]. The working principle of a solar cell consists of photogeneration and separation of charge carriers followed by their collection. In the photogeneration step, photon-induced electron-hole (e-h) pairs are created in the semiconductor material. If an incident photon on a semiconductor material has an energy hv (h: Planck's constant, v: frequency of the light) bigger than the bandgap (E_g) of the semiconductor, it creates an e-h pair by destroying a covalent bond in the semiconductor material (Fig. 1.9). To utilize the photogenerated e-h pair for current (photocurrent) generation, the e-h pair must be separated and then collected at their respective contacts, before they recombine.

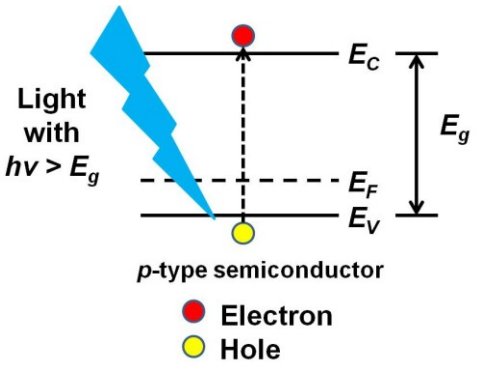

Figure 1.9 Schematic of photogeneration process in a *p*-type semiconductor. *hv*: Energy of the incident light (*h*: Planck's constant, *v*: frequency of the light). E_g: Bandgap of the semiconductor. E_C, E_F and E_V are the energy levels of the conduction band minimum, Fermi level and valence band maximum, respectively.

Because the electron and hole concentrations at thermal equilibrium is maintained at a constant value; therefore, when their concentrations are increased by generation of extra e-h pairs, such as by photogeneration, the concentrations of electron and holes are need to be reduced back to their equilibrium value by recombination. Separation requires diffusion of the e-h pair to the space charge region (SCR), if it was not created in the SCR. A built-in electric field existing at the SCR separates the e-h pair by sweeping the electron and hole towards opposite directions [19, 22].

The SCR and accompanying built-in electric field is created when a junction between *p*- and *n*-type semiconductor materials (*p*/*n* junction) is formed (Fig. 1.10). When a *p*-type and *n*-type semiconductors are brought into contact, equilibrium requires their Fermi energy levels (E_F) agree. The difference in the E_F of p-type semiconductor and n-type semiconductor is due to the difference in their average electron energy which is higher in the *n*-type than in the *p*-type. Therefore, in the initial step of a *p*/*n* junction formation, electrons from the *n*-type semiconductor diffuse into the *p*-type semiconductor, and holes diffuse to the opposite direction until equilibrium reached.

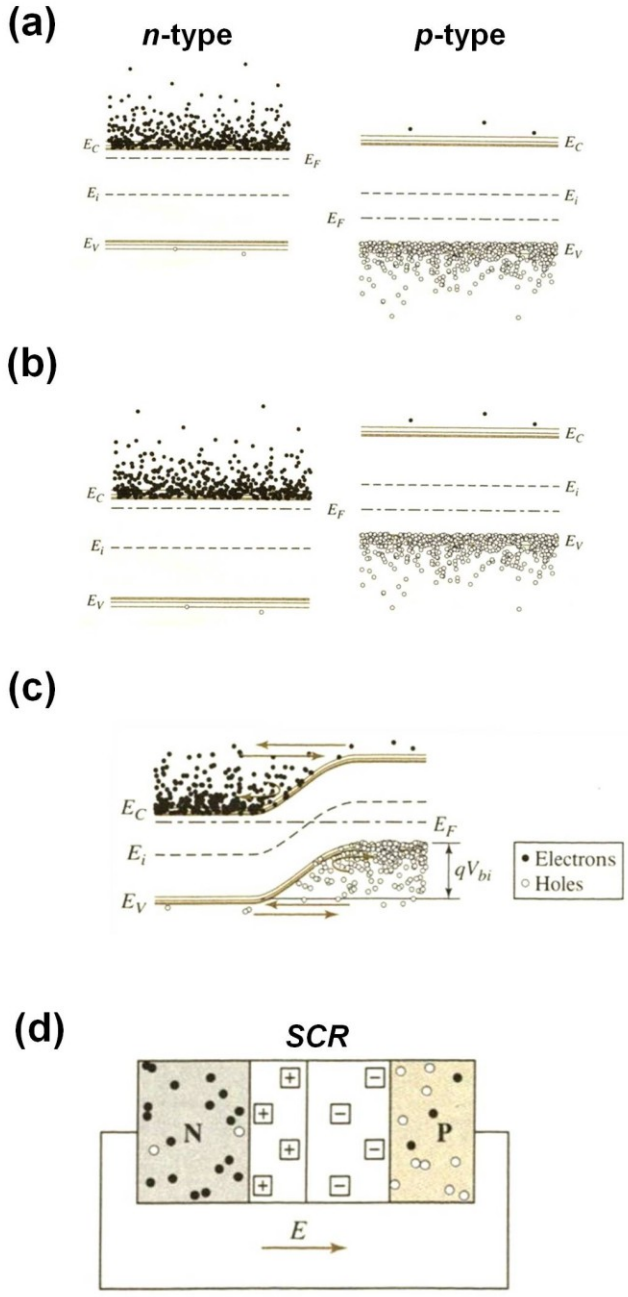

Figure 1.10 Schematic of *p*/*n* junction formation. *n*- and *p*-type semiconductors (a) before contact and (b) after contact. (c) Energy band diagram of the formed *p*/*n* junction showing the built-in energy barrier (qV_{bi}). (d) Cross-section of the *p*/*n* junction shown in (c). E_C, E_i, E_F and E_V are the energy levels of the conduction band minimum, Fermi level in the intrinsic semiconductor, Fermi level in the doped semiconductor and valence band maximum, respectively. Plus and minus signs indicate uncompensated donor and acceptor ions, respectively, located in the space charge region (SCR) which create a built-in electric field (*E*). After Ref. [22].

This diffusion process creates a SCR at the *p*/*n* junction together with a built-in electric field. Because electrons diffusing out from the *n*-type side of the junction leave uncompensated positively charged donor ions behind, meanwhile holes leave negatively charged acceptor ions in the *p*-type side of the junction. SCR forms by these fixed uncompensated donor and acceptor ions. The uncompensated fixed ions in the SCR create a built-in electric field which increases as the charge carrier diffusion proceeds and it prevents further carrier diffusion once the equilibrium reached. The built-in electric field in turn causes an electric potential difference at the edges of the SCR which forms a built-in energy barrier (qV_{bi}, q is the elementary charge and V_{bi} is the built-in voltage) [22, 23].

Equivalent electrical circuit of a solar cell can be viewed as a current source connected in parallel with a diode (Fig.1.11).

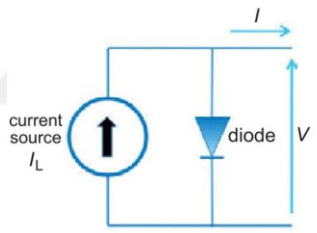

Figure 1.11 Equivalent circuit of a solar cell. *I*: Current. I_L: Photogenerated current. *V*:Voltage. [21]

A voltage (*V*) is developed between the terminals of a solar cell under illumination. Under open circuit condition, i.e. when load resistance (*R*) is infinite and current (*I*) is zero, the voltage developed is called open circuit voltage (V_{OC}). V_{OC} is the maximum voltage that can be obtained from a solar cell. On the other hand, when the solar cell is short circuited, i.e. when *V* is zero, the *I* drawn from the solar cell is called short circuit current (I_{SC}). Consequently, *V* is between 0 and V_{OC} for any *R* in the circuit, and the current drawn can be found by the Ohm's law

$$V = IR. \tag{1.2}$$

I_{SC} is approximately proportional to the illuminated area; therefore, short circuit current density (J_{SC}) can be used instead of I_{SC} for comparison purposes. In addition, I_{SC} depends on the spectrum of the incident light, and J_{SC} can be related to the spectrum of the incident light through the quantum efficiency (*QE*) of the solar cell. *QE* is defined as the probability that a photon with energy *E* delivers an electron to the external circuit. The relation between J_{SC} and *QE (E)* can be expressed as

$$J_{SC} = q \int b_s(E) QE(E) dE, \tag{1.3}$$

where q is the electronic charge and $b_s(E)$ is the incident photon flux density. While *QE* depends on the absorption coefficient of the solar cell material and the charge separation and collection efficiency of the solar cell, it does not depend on the incident light spectrum.

I – V characteristics of a solar cell under a particular illumination can be performed by sweeping an external voltage or current source. When *I – V* measurement of a solar cell is performed under dark, i.e. there is no photocurrent, the solar cell behaves like a diode. Therefore, it permits a larger current to flow when it is forward biased (V > 0) than reverse biased (V < 0). Consequently, *I – V* curve of a solar cell obtained under dark is the same as *I – V* curve of a diode under dark (Fig. 1.12).

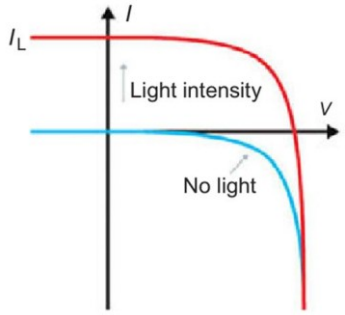

Figure 1.12 Current (*I*) – Voltage (*V*) curve of a solar cell under dark (blue) and light (red). I_L: Photogenerated current. [21]

Once the light is incident upon the solar cell, photocurrent is generated and *I* – *V* curve shifts down into the fourth quadrant due to power generation. The current drawn from a solar cell is always reduced from its I_{SC} value due to a dark current (I_{Dark}) flowing towards opposite direction. Generation of I_{Dark} is represented with the diode symbol in Fig. 1.11. The source of I_{Dark} is the potential difference created between the terminals of the solar cell, when a load is connected. As a result, the net current density can be expressed as

$$J(V) = J_{sc} - J_{Dark}(V) \tag{1.3}$$

This is due to the superposition approximation, i.e. overall response of a solar cell can be represented by the sum of I_{SC} and I_{Dark}. Moreover, the sign convention in photovoltaics requires photocurrent and voltage to be positive. Therefore, $J(V)$ is expressed as in Equation (1.3). In addition, although *I* – *V* curve of a solar cell is obtained in the fourth quadrant, it is presented in the first quadrant by flipping it over the *V* axis due to the sign convention in photovoltaics mentioned above.

$J_{Dark}(V)$ in Equation (1.3) can be written for an ideal diode as

$$J_{Dark}(V) = J_0(e^{\frac{qV}{k_B T}} - 1), \tag{1.4}$$

where J_0 is a constant, k_B is Boltzmann constant and *T* is temperature in Kelvin. Hence, for an ideal diode Equation (1.3) becomes

$$J = J_{sc} - J_0\left(e^{\frac{qV}{k_B T}} - 1\right). \tag{1.5}$$

An expression for V_{OC} can be obtained from the Equation (1.5), considering that under open circuit condition I_{SC} and I_{Dark} are equal [5],

$$V_{OC} = \frac{k_B T}{q} In\left(\frac{J_{SC}}{J_0} + 1\right). \quad (1.6)$$

Performance of a solar cell can be characterized by the parameters extracted from its *I* – *V* curve. The power (*P)* generated and delivered by a solar cell can be calculated by

$$P = IV. \quad (1.7)$$

According to the Equation (1.7), *P* is zero at I_{SC} and V_{OC}. The maximum power (P_{MAX}) point is reached between I_{SC} and V_{OC} at a particular *I* and *V* which are named current at P_{MAX} (I_{MP}) and voltage at P_{MAX} (V_{MP}) (Fig. 1.13).

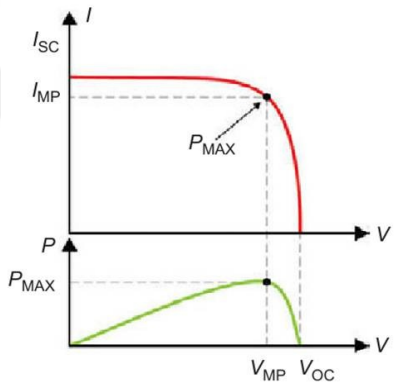

Figure 1.13 Current (*I*) – Voltage (*V*) and Power (*P*) – V curves of a solar cell. I_{SC}: Short-circuit current. P_{MAX}: Maximum power point. I_{MP}: Current at P_{MAX}. V_{MP}: Voltage at P_{MAX}. V_{OC}: Open circuit voltage. [21].

The fill factor (*FF*) is the ratio of P_{MAX} to theoretical power (P_T) (Fig. 1.14). P_T is the power generated when I_{SC} and V_{OC} exist together in a solar cell. Therefore, *FF* shows how close the *I* – *V* curve is to make a square together with *I* and *V* axes, and it indicates the quality of a solar cell.

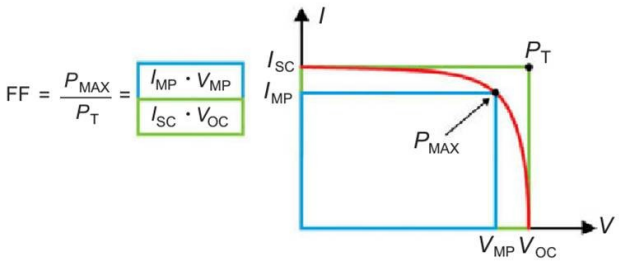

Figure 1.14 Fill factor (*FF*) determination from the current (*I*) – voltage (*V*) curve of a solar cell. I_{SC}: Short-circuit current. P_{MAX}: Maximum power point. P_T: Theoretical power. I_{MP}: Current at P_{MAX}. V_{MP}: Voltage at P_{MAX}. V_{OC}: Open circuit voltage. [21]

The power conversion efficiency (η) is the ratio of electrical power output (P_{OUT}) to solar power input (P_{IN}, irradiance of incident light (Wm^{-2}) x solar cell surface area (m^2)). The maximum η_{MAX} is obtained when P_{OUT} is equal to P_{MAX}; therefore,

$$\eta = \frac{P_{OUT}}{P_{IN}} \tag{1.8}$$

$$\eta_{MAX} = \frac{P_{MAX}}{P_{IN}} \tag{1.9}$$

In a real solar cell P_{MAX}, and hence η_{MAX}, is reduced due to resistance of the solar cell material and current leakage through the solar cell which are represented in the equivalent circuit diagram of a solar cell by a series resistance (R_S) and a parallel shunt resistance (R_{SH}), respectively (Fig. 1.15). Ideally, R_S should be zero so that there is not an additional voltage drop before the load, whereas R_{SH} should be infinite so that there is not a shunting path through the solar cell [5, 21]. Effects of R_S and R_{SH} on an *I* – *V* curve can be seen in Figure 1.16.

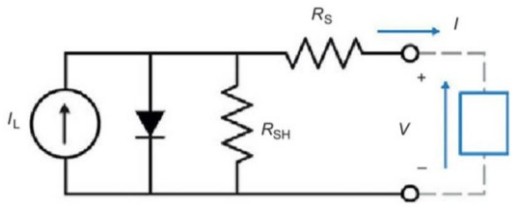

Figure 1.15 Equivalent circuit of a solar cell in Figure 1.11 with components for series resistance (R_S) and parallel shunt resistance (R_{SH}), and an external load (blue box) added. I: Current. I_L: Photogenerated current. V: Voltage. [21]

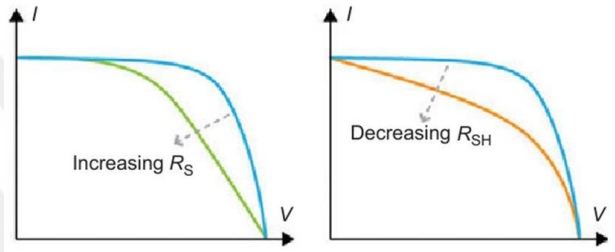

Figure 1.16 Effects of series resistance (R_S) and shunt resistance (R_{SH}) on I – V curve of a solar cell [21].

CHAPTER 2

PRINCIPLES OF EXPERIMENTAL METHODS

The basic principles of experimental methods used in this dissertation study are divided and explained in two sections: material preparation and material characterization methods.

2.1 Principles of Material Preparation Methods

2.1.1 Thin Film Deposition Methods

A thin film can be defined as a solid or a liquid material with one of its dimensions is much smaller than the other two [24, 25]. In this dissertation study, only solid films are prepared and characterized, and the term “thin film” is used for a film thinner than 5 μm.

Thin films can be deposited either by chemical methods, such as chemical vapor deposition, chemical bath deposition and sol-gel, or by physical methods, such as thermal evaporation and sputter deposition [24-27]. Thermal evaporation, sputter deposition and chemical bath deposition are the methods used to deposit thin films in this dissertation study and their principles are detailed below.

2.1.1.1 Thermal Evaporation

Thermal evaporation is a widely used and a convenient thin film deposition method which is based on transport and condensation of thermally evaporated source material onto a substrate under a high vacuum (usually $\leq 10^{-5}$ torr). In a typical thermal evaporation practice, a source material placed in an evaporation source is heated by passing an electrical current through the evaporation source until the source material evaporates or sublimes, and the material condenses on the substrate placed above the evaporation source forming a thin solid film in a vacuum chamber (Fig. 2.1). Having a high vacuum during thermal evaporation helps evaporation of the source material at a lower temperature than its boiling temperature at

atmospheric pressure. In addition, a longer mean free path for the vapor atoms than substrate-evaporation source distance (typically 10-50 cm) can be obtained, and oxidation of the deposited film or the source material can be prevented under a high vacuum. Evaporation source can be a boat or a wire coil made out of a refractory metal, such as Ta, Mo or W, that has a low vapor pressure at the operating temperature which can be defined as the temperature that is required obtaining ~10^{-2} torr vapor pressure of the source material to achieve sufficient deposition rates [24-28].

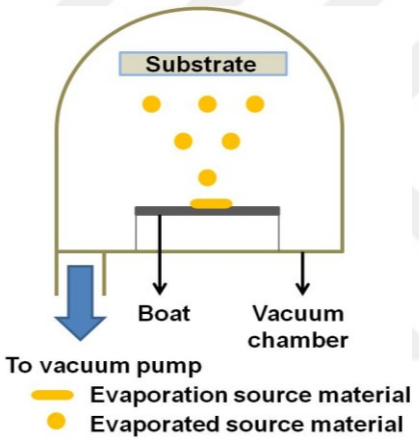

Figure 2.1 Schematic of a thermal evaporator. Source material in an evaporation source, boat in the figure, is heated by passing an electrical current through the boat in a vacuum chamber. A thin film forms on the substrate by condensation of evaporated source material.

2.1.1.2 Sputter Deposition

Sputter deposition is based on accumulation of ejected atoms from a target material to be deposited onto a substrate (Fig. 2.2). Ejection of target atoms is accomplished by bombardment of the target with positive ions which results in a momentum transfer from the positive ions to the target atoms and subsequently target atoms ejection. Positive ions necessary for sputtering the target is obtained by forming plasma of a noble gas (usually Ar) between the target and substrate. A noble gas introduced between a negatively biased target and a ground substrate ionizes under the high electric field and a neutral plasma forms which consists pairs of negatively charged electrons and positively charged ions. Impingement of the positive ions accelerated towards the negatively charged target under high electric field results

in removal of neutral target atoms that deposit onto the substrate. In addition to removing the target atoms, ion bombardment also causes emission of electrons from the target. These emitted electrons are necessary to obtain self-sustained plasma. Because while the emitted electrons accelerate towards the substrate, they collide with the sputter gas atoms and ionize them, and hence plasma can exist continuously.

The pressure in the sputter chamber is maintained usually around 20 mtorr which is adjusted by the rate of sputter gas flow into the chamber and a throttle valve placed between the vacuum pump and the chamber. A conductive target can be sputtered by applying a direct current (DC) voltage (1-5 kV) to the target (DC sputtering). However, an insulating target is sputtered by radio frequency (RF) sputtering method in which an alternating current (AC) voltage (typically at 13.56 MHz) is applied to the target. Because in case of an insulating target, electrons lost from the target due to positive ion impinging during sputtering are not replenished. Lack of electron replenishment causes front surface of the target to accumulate positive charge and consequently decrease in the potential difference between the target and substrate. As a result, the plasma cannot be self-sustained. In RF sputtering, the accumulated charge on the target surface is dissipated during the second half of the cycle, and hence, self-sustained plasma can be obtained.

In fact, majority of the electrons emitted from the target during both DC and RF sputtering are not utilized for sputter gas ionization. These non-utilized electrons cause undesired heating or damage of the locations they are collected upon, for instance substrate, and also a lower deposition rate when compared to the case where they are utilized for sputter gas ionization. These limitations are overcome by using a magnetron sputtering system in which a magnetic field is used to confine the movement of the emitted target electrons close to the target surface where they undergo ionizing collisions with the sputter gas atoms. The necessary magnetic field is obtained by placing a permanent magnet behind the target. The physical principle behind the magnetron sputtering is a magnetic field applies force on moving charged

particles; therefore, both the ionized sputter gas atoms and the emitted electrons are subject to the magnetic force (Fig. 2.2). While the magnetic field confines the movement of the electrons close to the target surface, the ionized gas atoms are not significantly affected due to their heavier mass. These electrons significantly increase the amount of ionized sputter gas atoms close to the target surface, resulting in increased sputter rate and reduced damage to the substrate. Because the electrons are used efficiently for sustaining the plasma during a magnetron sputtering, applied target voltage and the minimum pressure necessary to sustain the plasma can be in the range of 0.3-0.7 kV and a few mtorr, respectively, which are lower than the parameters used for a non-magnetron sputtering system explained above [24-28].

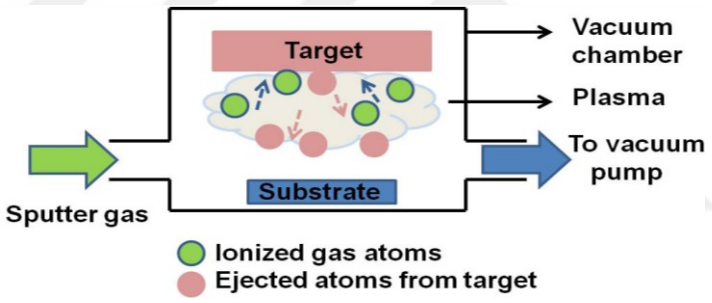

Figure 2.2 Schematic of a sputter deposition system. A thin film by sputter deposition forms by accumulation of neutral target material atoms ejected from the target material due to its bombardment by positively charged gas atoms in a vacuum chamber. Positively charged gas atoms necessary for sputtering are obtained by forming plasma between the negatively biased target and ground substrate. Plasma is charge neutral since it consists of positively charged gas atoms and negatively charged electrons.

2.1.1.3 Chemical Bath Deposition

A thin film by chemical bath deposition (CBD) is formed by a reaction occurring between precursor molecules or ions in a solution (usually aqueous) at a low temperature (30–80 °C), and the CBD process can be considered as an analogue to chemical vapor deposition. The advantage of CBD is being an inexpensive and convenient thin film deposition method such that a CBD apparatus in a laboratory can be set up by using a beaker for the chemical bath solution, a hot plate with magnetic stirrer, water or oil bath to immerse the beaker for a homogenous solution temperature (Fig. 2.3). A thin film by CBD is deposited by dipping a

substrate into a heated solution containing precursors of the material to be deposited. The solution is often stirred by a magnetic bar to avoid concentration gradient. The beaker containing the chemical bath can preferably be placed into a water bath to obtain a homogenous temperature distribution in the chemical bath and temperature can be measured by a thermometer inserted into the water bath. Although CBD method has been mostly used for deposition of various binary and ternary metal chalcogenide thin films, such as CdS and $CuInSe_2$, any compound can be deposited by CBD method provided that the compound can be prepared by a reaction with controllable rate to avoid its precipitation without forming a film on the substrate immersed into the solution, and the compound is insoluble and chemically stable in the solution used [12, 29-31].

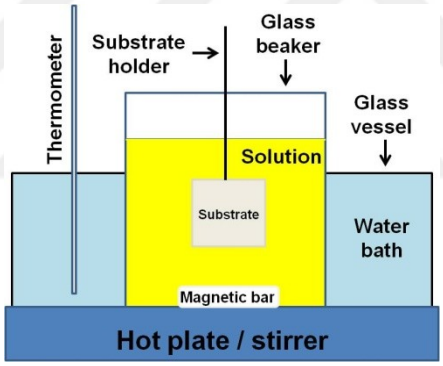

Figure 2.3 Schematic of a chemical bath deposition set-up.

Because CdS is a relevant material to this dissertation study, details on CBD is given here by taking CdS deposition by CBD (CdS-CBD) as an example. A typical CdS-CBD is made in an alkaline solution containing a cadmium salt, a sulfur source and a complexing agent, for which $CdSO_4$, $SC(NH_2)_2$, and NH_4OH are commonly used, respectively. A complexing agent is necessary to prevent precipitation of $Cd(OH)_2$ as well as to control the concentration of free Cd^{2+} in the solution to prevent rapid precipitation of CdS during CBD. CdS formation in a CBD process can be represented by the following reaction

$$Cd(NH_3)_4^{2+} + SC(NH_2)_2 + 2OH^- \rightarrow CdS + CN_2H_2 + 4NH_3 + 2H_2O \qquad (2.1)$$

Reaction (2.1) is the net reaction in a CdS-CBD process and it is commonly divided into the following reactions:

- release of cadmium ions by dissociation of cadmium salt

$$CdSO_4 \rightarrow Cd^{2+} + SO_4^{2-} \quad (2.2)$$

- equilibrium between NH_3 and H_2O

$$NH_3 + H_2O \leftrightarrow NH_4^+ + OH^- \quad (2.3)$$

- formation and dissociation of a complex between cadmium ion and ammonia

$$Cd^{2+} + 4NH_3 \leftrightarrow Cd(NH_3)_4^{2+} \quad (2.4)$$

- release of sulfur ions by hydrolysis of thiourea

$$SC(NH_2)_2 + 2OH^- \rightarrow S^{2-} + CN_2H_2 + 2H_2O \quad (2.5)$$

- CdS formation

$$Cd^{2+} + S^{2-} \rightarrow CdS \quad (2.6)$$

A CdS thin film by CBD can grow either by ion-by-ion or by cluster-by-cluster mechanisms. Ion-by-ion growth mechanism is based on heterogeneous nucleation of CdS on the substrate and subsequent growth of the film by addition of cadmium and sulfur ions. On the other hand, cluster-by-cluster growth mechanism is due to formation of CdS clusters in the solution by homogenous nucleation followed by adsorption and coagulation of these clusters onto the substrate forming a thin film. A third growth mechanism includes both ion-by-ion and cluster-by-cluster mechanisms, i.e. the CdS thin film first forms on the substrate by ion-by-ion

growth mechanism and then the film growth proceeds by addition of the clusters that form in the solution to the film [12, 29-36].

Deposition kinetics of CdS-CBD is mainly affected by the concentration of NH_3 and deposition temperature because both of them have an influence on the concentrations of both Cd^{2+} and S^{2-}. The concentration of NH_3 controls the concentration of $Cd(NH_3)_4^{2+}$ forming as well as the pH of the solution, which, in turn, affects the hydrolysis rate of $SC(NH_2)_2$. Additionally, stability constant of $Cd(NH_3)_4^{2+}$ and hydrolysis rate of $SC(NH_2)_2$ are affected by the temperature [29, 33, 36]. A relatively less investigated aspect of the deposition kinetics is the solution stirring rate during CdS-CBD, i.e. hydrodynamic condition of the solution during CBD, which is detailed and studied in Chapter 5 of this dissertation.

2.1.2 Bulk Crystal Growth by Bridgman Method

Bridgman method is a crystal growth technique from the liquid phase of a material. It is based on freezing a melt by cooling it below its melting point gradually from one end to the other in a two-zone furnace. Bridgman growth can be performed in a vertical or a horizontal configuration. In a typical vertical Bridgman method, a molten charge in an ampoule is solidified by lowering it from the upper hot zone where the charge is melt to the lower cooler zone which is below the material's melting temperature with a growth rate in the range of 0.1-30 mm/h (Fig. 2.4). Either the crucible or the furnace can be moved to progress the solid/liquid interface by maintaining a large temperature gradient at the interface. Silica, graphite and some of metals (e.g. Mo) are used as crucible material, and the crucibles are commonly prepared with a tapered tip to nucleate one crystal or a seed can also be used. Bridgman method can be performed by a simple set-up with little supervision and growth can be made at a high rate; however, nucleation at the crucible walls, dislocation formation, twinning and deviation from stoichiometric composition are the common problems affecting the crystal quality. Nucleation at the crucible walls can be prevented by making the solid/liquid interface concave into the melt,

and dislocation density can be reduced by maintaining a low radial temperature gradient [37, 38].

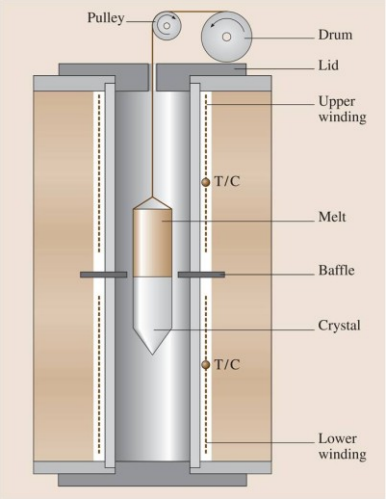

Figure 2.4 Schematic of a two-zone vertical Bridgman growth set-up. The two zones of the furnace can be separated by baffles for thermal isolation [37].

2.2 Principles of Material Characterization Methods

2.2.1 Scanning Probe Microscopy Techniques: Atomic Force Microscopy, Electrostatic Force Microscopy and Kelvin Probe Force Microscopy

Kelvin probe force microscopy (KPFM) is an atomic force microscopy (AFM) based technique that is used to measure a contact potential difference (CPD) between a conductive AFM tip and a sample. Because it is based on AFM, it is possible to obtain the work function or the surface potential map of a sample with a high spatial resolution. KPFM is an extension of the macroscopic Kelvin probe (KP) technique introduced by Lord Kelvin in 1898 [39] to the AFM set-up. CPD measurement in the KP technique is based on nullifying the alternating current (AC) generated in the circuit connecting the plates of a vibrating parallel plate capacitor. In the KP set-up, a sample serves as one of the plates and a metal plate with known work function is vibrated over the sample. Capacitance between the plates changes due to the changing distance between them and it results in an AC in the circuit which is nullified by applying a direct current (DC) voltage (V_{DC}) to one of the plates. Applied V_{DC} is equal to the CPD between these

two materials. Although KPFM stems from the KP technique, it is important to note that, in KPFM, the electrostatic force between the materials is nullified by a V_{DC} instead of a current. Because, the size of the plates becomes smaller in an AFM set-up, hence the current generated is not large enough to be measured [40, 41]. Since KPFM is based on AFM, first of all, operation principles of AFM will be introduced followed by those of KPFM.

2.2.1.1 Operation Principles of Atomic Force Microscopy

AFM was introduced in 1986 [42] making high resolution surface imaging of non-conductive materials possible. Because AFM operates by measuring force between a probe and a sample unlike its parent technique, scanning tunneling microscopy (STM) [43], which operates by measuring tunneling current between the probe and sample [44, 45]. An AFM set-up basically consists of a cantilever with a sharp tip located at its end, a laser source and a position sensitive photodiode (PSPD) (Fig. 2.5).

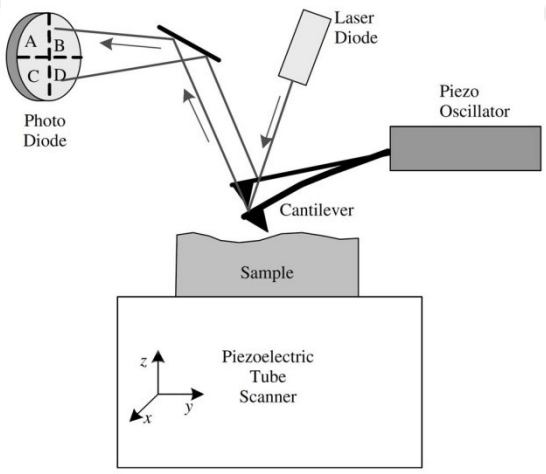

Figure 2.5 Schematic of an atomic force microscope (AFM) set-up [44].

The cantilever can be a single beam type (Fig. 2.6a) or a triangular beam type (Fig. 2.6b). Single beam cantilevers are usually made out of silicon (typically 100-500 μm long and 0.5-5 μm wide), whereas triangular cantilevers are usually made out of silicon nitride by microfabrication processes. The tip is generally cone-shaped with a 10-20 nm tip radius. The scan is performed by keeping the tip stationary and moving the sample by a piezoelectric

scanner or vice versa depending on the design of a particular AFM set-up. The laser beam and PSPD is used for detecting the force between the tip and sample (tip-sample force). The laser beam is generated from a solid-state diode and is cast to the backside of the cantilever from where it is reflected onto the PSPD. As the cantilever scans the sample surface, it is elastically bent due to the tip-sample force. Bending of the cantilever causes the position of the laser beam on the PSPD change and on a four-segmented PSPD, vertical and horizontal motions of the cantilever can be detected by Z = (A+C) – (B+D) and X = (A+B) – (C+D) signals, respectively. Topographical information of the sample is obtained by varying the distance between the tip and sample (*z*) by the piezoelectric tube scanner to keep the signal Z constant, i.e. by keeping cantilever's deflection constant, by a feedback loop. The signal X can be used to measure local friction [44-48].

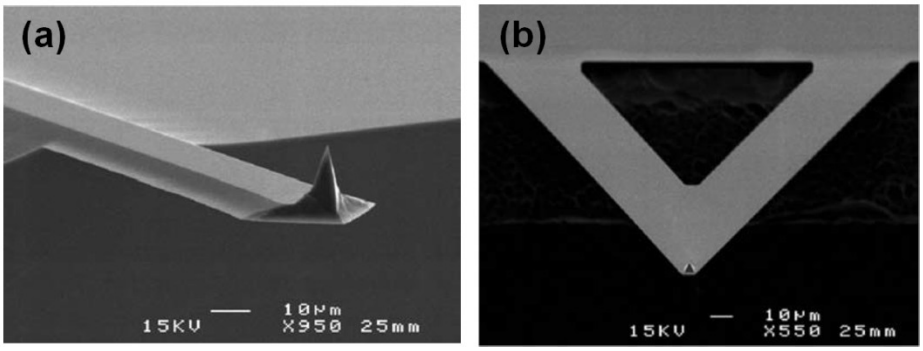

Figure 2.6 SEM micrographs of (a) single beam and (b) triangular beam cantilevers. After Ref. [46].

Topographic imaging by an AFM can be performed by one of these three modes: contact, non-contact and intermediate contact. A distinction between these three modes can be made by considering whether the tip-sample interaction forces (F_{ts}) are attractive, repulsive or consist of both (Fig. 2.7).

Contact AFM is operated in the repulsive force regime. The tip is in contact with the sample surface during scan, and cantilever deflection due to the repulsive force is measured and kept constant at a set value by the feedback loop. In non-contact AFM (NC-AFM) and

intermediate contact AFM, the cantilever is mechanically excited to oscillate at or close to its resonance frequency (f_0) by a piezoelectric crystal.

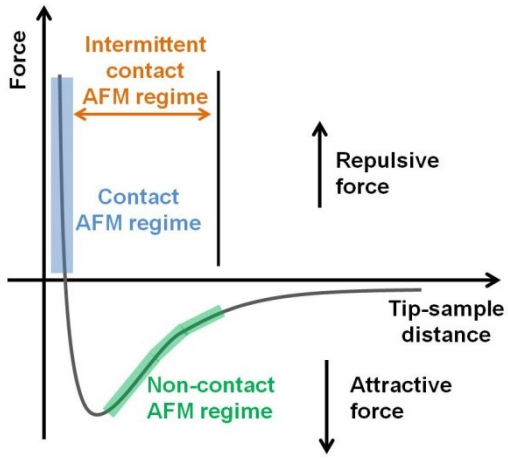

Figure 2.7 AFM modes shown on a schematic force vs. tip-sample distance plot. After Ref. [49].

NC-AFM is operated in the attractive tip-sample interaction force regime and resonance frequency f_0 shifts to a lower frequency (effective frequency, f_{eff}) due to the tip-sample interaction force as the cantilever approaches to the sample. Initial oscillation amplitude A_0 of the cantilever at the drive frequency f_1 reduces to A_1 due to the frequency shift Δf_0 (Fig. 2.8).

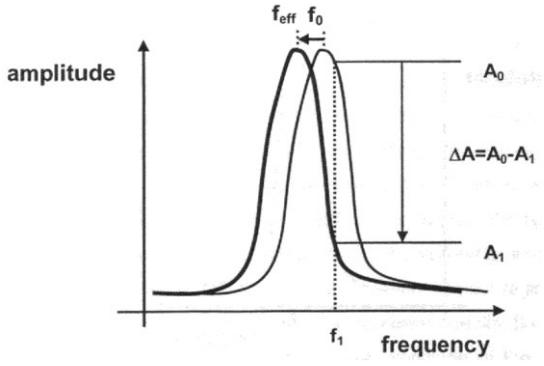

Figure 2.8 Shift in the amplitude vs. frequency curve of a cantilever due to attractive tip-sample interaction forces [50].

In the attractive tip-sample interaction force regime, because the force gradient, $\partial F_{ts}/\partial z$ is positive, the effective spring constant of the cantilever, k_{eff} becomes smaller than the intrinsic spring constant, k according to the following relation,

$$k_{eff} = k - (\partial F_{ts}/\partial z). \tag{2.1}$$

Consequently, a smaller effective spring constant results in a lower f_{eff} in the attractive tip-sample interaction regime and vice versa, since the following equation holds for a beam cantilever

$$f_0 = 1/2\pi \sqrt{k/m}, \tag{2.2}$$

where f_0 is the resonance frequency of the cantilever, and k and m are its spring constant and mass, respectively [40, 41, 44, 46, 48-50]. The approximate frequency shift, Δf_0 can be written as

$$\Delta f_0 = f_{eff} - f_0 = -\frac{f_0}{2k}\frac{\partial F_{ts}}{\partial z}. \tag{2.3}$$

Detection in NC-AFM can be performed by either amplitude modulation (AM) or frequency modulation (FM) techniques. In AM technique (AM-AFM), the cantilever is oscillated at a fixed driving frequency which is close to its resonance frequency. The shift in the resonance frequency due to tip-sample interaction causes the oscillation amplitude at the fixed driving frequency to change, and the feedback loop adjusts the tip-sample distance to keep the oscillation amplitude constant. In FM technique (FM-AFM) (Fig. 2.9), the cantilever is oscillated at its resonance frequency (setpoint frequency), f_0 and an FM demodulator in the frequency regulation system determines the frequency shift Δf_0 occurring due to tip-sample interaction by comparing the set frequency, f_0 and the oscillation frequency, f sent from the preamplifier. Obtained Δf_0 is then fed into the z regulator to maintain a constant z and consequently to obtain

a topography image. At the same time, amplitude regulation system excites the cantilever to keep the amplitude of the cantilever oscillation at the setpoint amplitude, A_0 after comparing it with the amplitude of the signal sent from the preamplifier.

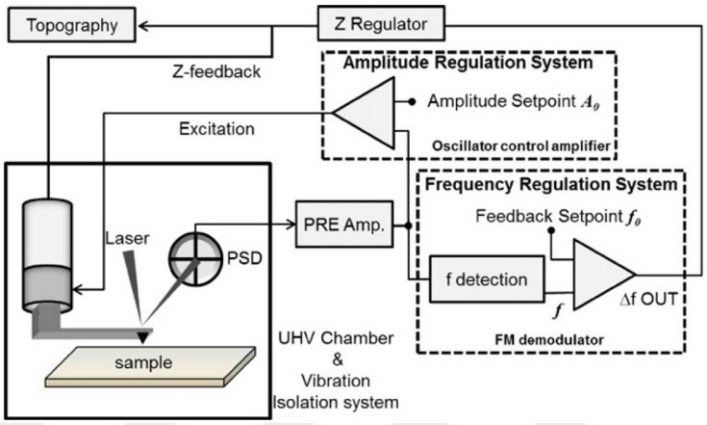

Figure 2.9 Block diagram of an atomic force microscope (AFM) operated by frequency modulation (FM) detection technique in an ultrahigh vacuum (UHV) chamber. Signal from position sensitive photodiode (PSD) is amplified by a preamplifier (PRE Amp.) before it was sent to the frequency regulation system for obtaining topographical information and to the amplitude regulation system for maintaining the cantilever oscillation amplitude constant at the setpoint amplitude, A_0 [41].

To make high-resolution imaging, it is desirable to operate an AFM under an ultra-high vacuum (UHV). Because resolution of AFM depends on the quality factor (Q) which is defined as

$$Q = \frac{f_0}{\Delta f}, \tag{2.4}$$

where Δf is the full-width-half-maximum of the cantilever resonance curve. And minimum detectable force gradient (δF_{min}) by an AFM can be represented by

$$\delta F_{min} = \sqrt{\frac{2k_L k_B T B}{\omega_0 Q \langle z_{osc}^2 \rangle}}, \tag{2.5}$$

where k_L is the cantilever's force constant, k_BT is the thermal energy at temperature, *T*, B is the measurement bandwidth, ω_0 ($2\pi f_0$) is the cantilever angular resonance frequency, and $\langle z_{osc}^2 \rangle$ is the mean square amplitude of the driven cantilever vibration. If we consider that typical *Q* of a cantilever in air is around 100, whereas it is around 50,000 in UHV, the Equation 2.5 clearly indicates that when an AFM is operated under UHV condition, it has 20-25 times higher resolution than when operated in air. However, while FM-KPFM is suitable for AFM operations under UHV, AM-KPFM is not. Because increased *Q* under UHV results in a very slow amplitude change response in AM-KPFM, since the time scale of the amplitude change (τ_{AM}) is linearly dependent on the *Q* ($\tau_{AM} \approx 2Q/f_0$). , whereas that of frequency change in FM-AFM technique (τ_{FM}) is independent of *Q* ($\tau_{FM} \approx 1/f_0$) [40, 41].

Intermediate contact AFM is operated in both attractive and repulsive tip-sample interaction force regimes, i.e. the oscillating cantilever's tip lightly taps the sample surface. Cantilever's oscillation amplitude reduces due to the light tapping while the oscillation frequency is kept constant during scan. The feedback loop adjusts *z* to maintain the oscillation amplitude shift constant [40, 41, 44, 46, 48-50].

2.2.1.2 Operation Principles of Kelvin Probe Force Microscopy

KPFM is a NC-AFM based technique used to acquire a CPD map of a sample with a high spatial resolution [51]. CPD can be defined as the work function (ϕ) difference between two materials. If an AFM tip and a sample with different ϕ are considered, their vacuum levels (E_{vac}) will be aligned, whereas their Fermi energy levels (E_f) will have a difference (Fig. 2.10a). Once the tip and sample are in electrical contact, equilibrium is established by electron current flow and their E_f agree (Fig. 2.10b). At the same time, CPD developed upon contact is illustrated by a difference between their E_{vac}. An electrostatic force is generated between the tip and sample since both of them become charged due to the electron current flow necessary for reaching equilibrium. This CPD, and hence the electrostatic force, between the tip and sample can be nullified by applying an external V_{DC} with equal magnitude with CPD, but with opposite sign (Fig.

2.10c). Consequently, the applied external V_{DC} corresponds to the ϕ difference between the tip and sample, and if the tip's work function ϕ_{Tip} is known, sample's work function ϕ_{Sample} can be determined [40, 41, 52].

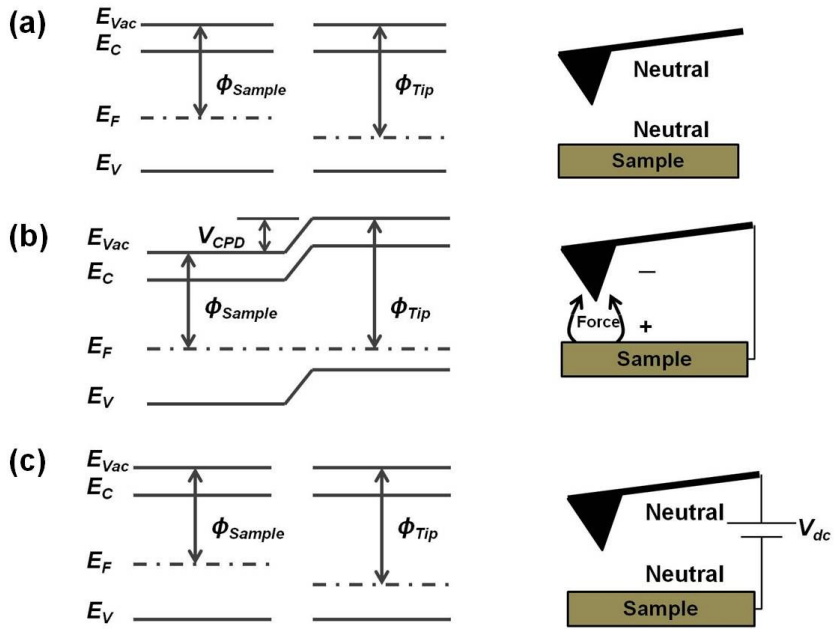

Figure 2.10 Energy diagrams of a tip and sample (a) before contact, (b) after contact, and (c) after V_{dc} is applied. E_{Vac}, E_C, E_F, and E_V are the energy levels of vacuum, conduction band, Fermi level and valence band, respectively. ϕ: work function. V_{CPD} and V_{dc} are CPD developed between the tip-sample and dc bias applied to nullify it, respectively.

In NC-AFM, tip-sample interaction forces include short range repulsive and chemical binding forces, the van der Waals force, and the long range electrostatic and magnetic forces. Among these tip-sample interaction forces, the electrostatic force (F_{el}) is related to KPFM measurement [40]. If we consider the tip-sample system as a capacitor, the capacitance (C) and energy stored in the capacitor (U_{el}) are

$$C = \frac{Q}{V}, \tag{2.6}$$

$$U_{el} = \frac{1}{2}CV^2 = \frac{1}{2}\frac{Q^2}{C}, \tag{2.7}$$

where *V* and *Q* are voltage and charge, respectively. By using the potential energy function for the *z* direction ($F_{el} = -\partial U_{el}/\partial z$), it can be shown that

$$F_{el} = -\nabla U_{el} = -\frac{1}{2}\frac{\mathrm{Q}^2}{\mathrm{C}^2}\frac{\partial \mathrm{C}}{\partial \mathrm{z}} = -\frac{1}{2}\frac{\partial C}{\partial z}V^2. \quad (2.8)$$

In Equation (2.8), forces in the *z* direction is considered, because the main contribution is from the forces perpendicular to the sample surface in AFM [40, 41, 44, 52-54]. During a KPFM measurement, apart from applying an external V_{DC} to nullify the CPD, an external ac voltage (V_{AC}) at the frequency ω_{ac}, $V_{ac}\sin(\omega_{ac}t)$, is also applied between the tip and sample. The applied V_{AC} generates an oscillating electrostatic force that causes the cantilever to oscillate at ω_{ac}. Upon application of these additional voltages, the total voltage between the tip and the sample is $V = V_{dc} - V_{CPD} + V_{ac}sin(\omega_{ac}t)$, and the electrostatic force F_{el} can be written as

$$F_{el} = -\frac{1}{2}\frac{\partial C}{\partial z}[V_{dc} - V_{CPD} + V_{ac}sin(\omega_{ac}t)]^2, \quad (2.9)$$

where $\partial C/\partial z$ is the capacitance between the tip and the sample, and V_{CPD} can be written as the work function difference between the tip and sample ($\Delta\phi$),

$$V_{CPD} = \Delta\emptyset/e = \left(\emptyset_{sample} - \emptyset_{tip}\right)/e, \quad (2.10)$$

where *e* is the elementary charge. It should be noted that V_{CPD} in Equation (2.10) is written for a KPFM set-up where the voltage is applied to the sample and the tip is ground. For the case where the voltage is applied to the tip and the sample is ground, V_{CPD} is written as

$$V_{CPD} = \Delta\emptyset/e = \left(\emptyset_{tip} - \emptyset_{sample}\right)/e. \quad (2.11)$$

F_{el} in Equation (2.9) can be divided into three parts

$$F_{dc} = -\frac{\partial C}{\partial z}\left[\frac{1}{2}(V_{dc} - V_{CPD})^2 + \frac{V_{ac}^2}{4}\right], \quad (2.12)$$

$$F_{\omega_{ac}} = -\frac{\partial C}{\partial z}(V_{dc} - V_{CPD})V_{ac}sin(\omega_{ac}t), \quad (2.13)$$

$$F_{2\omega_{ac}} = \frac{\partial C}{\partial z}\frac{V_{ac}^2}{4}cos(2\omega_{ac}t). \quad (2.14)$$

F_{dc} contributes to the topography signal, $F_{\omega_{ac}}$ is used to measure the CPD and $F_{2\omega_{ac}}$ is used for capacitance microscopy [40, 41, 44, 52, 53, 53]. In addition, $F_{\omega_{ac}}$ component (Eq. (2.13)) can also be used for electrostatic force microscopy (EFM) measurement. EFM maps the electrostatic force on the sample surface, i.e. it is a qualitative surface potential measurement. This is realized by disengaging the feedback loop that matches V_{dc} with V_{CPD}, hence by acquiring an image with the $F_{\omega_{ac}}$ signal [53, 55, 56].

Similar with NC-AFM, KPFM can also be operated with AM and FM detection modes. In AM-KPFM, the amplitude of the electrostatic force-induced cantilever oscillation at ω_{ac} is measured directly by a lock-in amplifier. As is shown in Equation (2.13), $F_{\omega_{ac}}$ is minimized when V_{dc} is equal to V_{CPD}; therefore, by matching V_{dc} and V_{CPD} during the scan, simultaneous topographic and CPD imaging can be performed. Applied ω_{ac} is usually 10-30 kHz, and 1-5 V V_{AC} is necessary to obtain sufficient sensitivity [40, 52]. Another way of performing AM-KPFM is tuning the ω_{ac} to the second resonance frequency of the cantilever which is typically 6 times the first resonance frequency with a smaller and broader peak than the first resonance frequency peak. While topographical information is obtained by assigning the *z* control to the first resonance frequency of the cantilever, the applied V_{AC} simultaneously induces cantilever oscillation at the second resonance frequency which is used for acquiring CPD information. Therefore, topographical and CPD signals can be easily separated. Amplification of the

oscillation at ω_{ac} by the quality factor Q results in enhanced sensitivity and allows V_{AC} to be as small as 100 mV. Using small V_{AC} is an important outcome of this method because, first of all, V_{AC} affects the topography signal F_{dc} due to the $V_{ac}^2/4$ term as shown in Equation (2.12), hence using a small V_{AC} is desirable to reduce the electrostatic effect in the topography signal. Second advantage of using small V_{AC} is preventing a possible tip-induced band bending that can be caused by large V_{AC} [40, 41, 52].

In an FM-KPFM measurement, oscillation of frequency shift, Δf_0 at ω_{ac} is detected. As was explained above, the shift in the cantilever resonance frequency Δf_0 occurs due to the long range forces including the electrostatic force, F_{el} according to Equation (2.3). The applied V_{ac} at ω_{ac} modulates F_{el} at ω_{ac} (Eq. (2.13)) and at $2\omega_{ac}$ (Eq. (2.14)) and consequently this modulation results in the frequency shift, Δf_0 oscillation at ω_{ac} and at $2\omega_{ac}$. It is shown in Figure 2.11 that, in addition to the peaks at ω_{ac} and $2\omega_{ac}$ appearing due to the force modulation, sidebands at $f_0 \pm \omega_{ac}$ and $f_0 \pm 2\omega_{ac}$ also appear next to f_0 due to the modulated force gradient. In FM-KPFM, the signal at $f_0 \pm \omega_{ac}$ is detected by a lock-in amplifier and minimized by the applied V_{dc}. It can be shown by Equations (2.3) and (2.13) that the detected signal is approximately proportional to the force gradient,

$$\Delta f_0(\omega_{ac}) \propto \frac{\partial F_{\omega ac}}{\partial z} = \frac{\partial^2 C}{\partial z^2}(V_{dc} - V_{CPD})V_{ac}sin(\omega_{ac}t). \qquad (2.15)$$

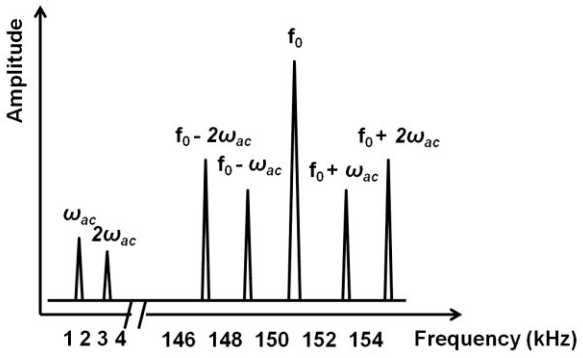

Figure 2.11 Schematic frequency spectrum of a cantilever when an alternating current (AC) voltage V_{ac} at frequency ω_{ac} is applied. After Ref. [57].

In an FM-KPFM measurement, the frequency ω_{ac} has to be chosen in a way that it is high enough to prevent cross-talk to the topography signal as well as low enough to be in the bandwidth of the frequency demodulator of the KPFM set-up. As the frequency ω_{ac} is increased, crosstalk to the topography signal decreases together with the signal intensity of the electrostatic force, because of the limited bandwidth of the frequency demodulator. Typical ω_{ac} values used in FM-KPFM are in the range of 1-3 kHz. In addition, to obtain sufficient sensitivity, usually V_{ac} larger than 2 V is used. As was mentioned above, a large V_{ac} increases the electrostatic contribution to the topography signal and it can result in tip-induced band bending on semiconductor samples. Therefore, FM-KPFM measurements need to be performed by lowering V_{ac} as low as possible [40, 41, 52, 57, 58].

The main difference between AM- and FM-KPFM is the signal they detect; AM-KPFM detects the electrostatic force, whereas FM-KPFM detects the electrostatic force gradient. This difference results in different spatial resolution obtained from these two modes of KPFM. The spatial resolution of FM-KPFM is higher than AM-KPFM because detection of electrostatic force gradient is a short-range detection, whereas that of electrostatic force is a long-range detection. In the attractive force regime (Fig. 2.7), the force gradient becomes larger as the tip-sample distance is decreased; therefore, the force gradient is mainly detected at the apex of the tip. However, since AM-KPFM detects the electrostatic force by a long-range detection scheme, both the tip and the cantilever is included in the electrostatic interaction, which results in reduced spatial resolution by an averaging effect. On the other hand, when the AM-KPFM is used by tuning the ω_{ac} to the second resonance frequency of the cantilever, energy resolution of AM-KPFM is better than FM-KPFM. Because measurement with AM-KPFM in this configuration is based on resonance peak of the cantilever which increases the signal-to-noise ratio, whereas detection through FM demodulator in FM-KPFM generates additional noise in the measurement. However, when AM-KPFM is operated by setting ω_{ac} to 10-30 kHz instead of the

second resonance frequency of the cantilever, energy resolution of AM-KPFM becomes lower than FM-KPFM as shown by simulations and experiments [40, 41, 52].

A schematic of electronic components of a typical FM-AFM together with AM- and FM-KPFM components is shown in Figure 2.12. A lock-in amplifier reference signal channel outputs V_{ac} (OSC out) to be applied to the cantilever. Signal from position sensitive photodiode (PSD) is first amplified by a preamplifier (PRE Amp.) before it was sent to the other components. In FM-KPFM, the frequency shift signal, Δf is split into two and sent to both z regulator of the AFM and the lock-in amplifier. The lock-in amplifier separates the signal that has the same frequency with the V_{ac} and sends it to the KPFM controller. The KPFM controller applies V_{dc} to the tip to minimize the lock-in amplifier output signal. In AM-KPFM measurement, ω_{ac} can be in the range of 10-30 kHz (a frequency that is away from the cantilever resonance frequency to prevent cross-talk between the topography and KPFM signals) or it can also be tuned to the second resonance frequency of the cantilever for measuring the CPD, whereas the first resonance frequency of the cantilever can be used for topography imaging. Therefore, the amplitude of the cantilever oscillation has a low and high frequency components in AM-KPFM. After these frequencies are filtered by a band-pass filter, the low frequency component is used by z regulator of the AFM to obtain the topography image and the high frequency component is sent to the lock-in amplifier. KPFM controller applies V_{dc} to the tip to minimize the lock-in amplifier output signal as in the case of FM-KPFM [41].

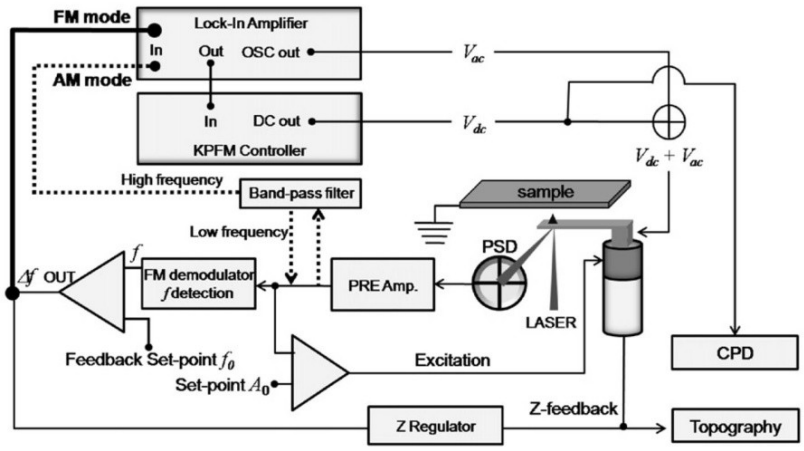

Figure 2.12 Block diagram of an atomic force microscope (AFM) operated by frequency modulation (FM) technique with necessary components for amplitude modulation (AM) and FM-Kelvin probe force microscopy (KPFM) measurements [41].

2.2.2 Electron Backscatter Diffraction

Electron backscatter diffraction (EBSD) technique is used for texture determination in a scanning electron microscope (SEM). It allows studying microstructure quantification; orientation of each grain, i.e. microtexture, and the orientation relationships between the grains, i.e. mesotexture; grain boundary characterization; phase identification, distribution and phase boundary characterization; and strain determination of crystalline materials [59-62]. Although there are other techniques to study texture, obtaining a wide range of information as can be obtained by EBSD is not possible. For example, X-ray and neutron diffraction often examine a large volume of the sample at once and hence obtaining local information simultaneously is not possible, and the crystallographic information obtained by transmission electron microscopy (TEM) is only from a small portion of the sample. Other SEM based techniques for texture determination, such as selected-area channeling and Kossel diffraction, have a lower spatial resolution (micron range) than EBSD has and they are less efficient than EBSD [62, 63]. Consequently, EBSD has become an important technique for studying texture due to its high angular resolution (0.5°-1°) (i.e. diffraction pattern indexing precision), sub-micron spatial resolution, and the ease of EBSD sample preparation. Also, other SEM-based techniques, such

as energy dispersive X-ray spectroscopy, can be used together with EBSD to make a comprehensive analysis on the same sample region examined [60, 62-64].

EBSD is based on analyzing EBSD patterns generated from a sample in SEM. EBSD patterns are essentially Kikuchi patterns that are generated by backscatter diffraction of a stationary high energy electron beam from a sample surface. The sample stage in SEM is tilted typically around 70° with respect to the plane of the sample, i.e. the sample makes a shallow angle with the incident electron beam (accelerating voltage: 10-30 kV, current: 1-50 nA) (Fig. 2.13). This is to maximize the fraction of backscattered electrons those escape from the sample surface and reach the phosphor screen where the diffraction pattern of the backscattered electrons is imaged. A charge coupled device (CCD) camera is usually used to capture the images on the screen.

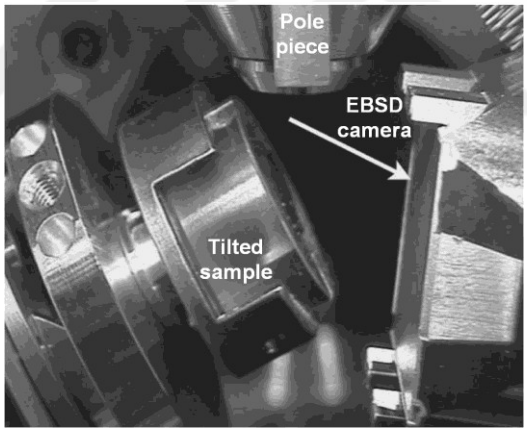

Figure 2.13 A typical EBSD geometry inside SEM. The fraction of the backscattered electrons are increased by tilting the sample (typically ~70°) with respect to the sample plane, i.e. the sample makes a shallow angle with the incident electron beam sent from the pole piece. The arrow indicates the EBSD camera upon where the backscattered electrons form an EBSD pattern of the sample. After Ref. [64].

The beam-sample interaction depth is few tens of nanometers; therefore, crystalline perfection of this top layer affects EBSD pattern quality. In addition, the sample surface needs to be flat to prevent regions shadowed by surface features. Although conventional metallographic methods are usually sufficient for sample preparation for EBSD, additional steps, for instance electropolishing, etching or ion milling, can be necessary to obtain a flat and deformation-free

sample surface. A thin conductive layer, such as carbon, can be applied onto non-conductive samples, and the extra thickness can be compensated by increasing the accelerating voltage [59-66]. A schematic showing formation of Kikuchi patterns in EBSD in SEM, and an EBSD pattern from a Cu(In,Ga)Se_2 thin film, as an example, can be seen in Figures 2.14a and 2.14b, respectively.

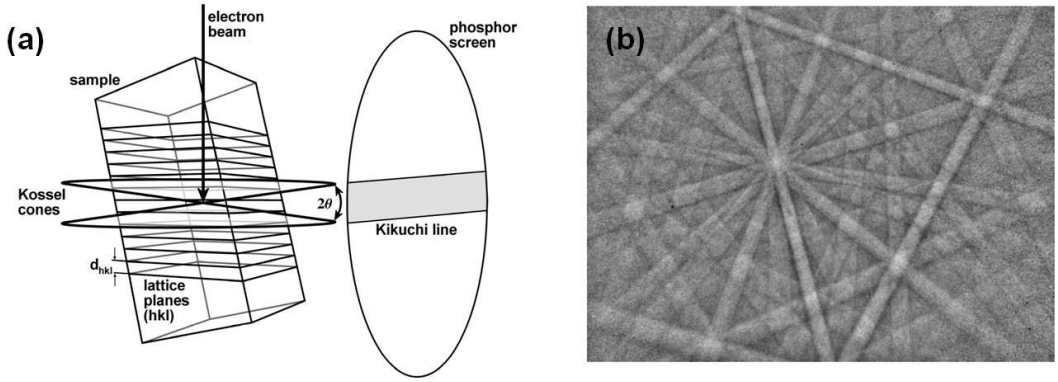

Figure 2.14 (a) Formation of Kikuchi lines on a phosphor screen by diffraction of backscattered electrons from a tilted sample during EBSD operation, and (b) an EBSD pattern from a Cu(In,Ga)Se_2 thin film. After Ref. [67].

Kikuchi line formation can be clearly pictured by considering their formation in a TEM. When an electron beam enters to a sample, some of the electrons undergo inelastic scattering within the sample (Fig. 2.15a). These diffusely scattered electrons diverging from a point source impinge onto crystal planes in all directions, and they are elastically scattered when the Bragg's law is satisfied;

$$n\lambda = 2d_{hkl}sin\theta_{hkl} \tag{2.16}$$

where n is the order of diffraction, λ is the wavelength of the electron beam, d_{hkl} is the interplanar spacing of the hkl planes, and θ_{hkl} is the Bragg angle.

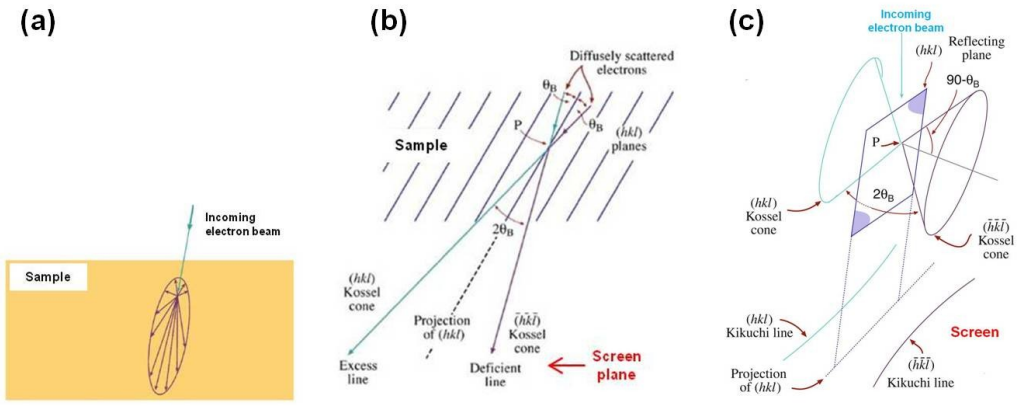

Figure 2.15 A schematic of Kikuchi pattern formation in TEM. (a) Electrons entering the sample diffusely scatter in all direction. (b) Diffusely scattered electrons are diffracted by the crystal planes when the Bragg's law is satisfied. (c) Since the electrons impinge onto the planes in all directions, scattered electrons form cones (Kossel cones) which are almost flat and hence views as almost parallel lines (Kikuchi lines) on the screen. θ_B is the Bragg angle. After Ref. [68].

Therefore, electrons arriving at the crystal planes at the Bragg angle diffract, and there are always electrons satisfying this condition for all crystal planes due to the divergent electrons. Diffracted electrons form two cones (Kossel cones); one cone for each side of the diffracting *hkl* plane as the electrons satisfy the Bragg's law in all directions (Fig. 2.15b). Kossel cones extend with a half apex angle of $90° - \theta_{hkl}$ about the normal of *hkl* planes, because diffracted electrons arrive at *hkl* planes at θ_{hkl} (Fig. 2.15c). Since a typical value for θ_{hkl} is 0.5°, apex angle of a cone is around 180°. That is, the Kossel cones are almost flat, and they form nearly parallel Kikuchi lines when they are recorded on a screen intercepting the Kossel cones. The bright line (excess line) forms at the location towards where the incoming electron beam is diffracted. The dark line (deficient line) forms at the direction of the incoming electron beam because the electrons are diffracted away and do not contribute to the intensity at this direction. The angular distance between the Kikuchi lines (width of a Kikuchi band) is $2\theta_{hkl}$; one line is for θ_{hkl} and the other one is for $-\theta_{hkl}$. Therefore, all of the Kikuchi bands on a Kikuchi pattern have a distinct width and belong to a particular *hkl* plane. The trace of the crystallographic plane is located in the middle of the Kikuchi band that it belongs to. Intersections of Kikuchi bands define

crystallographic zone axes (poles) which are specific crystallographic directions. Consequently, since a Kikuchi pattern provides information on the crystallographic angular relationship in the sample, indexing of Kikuchi pattern is possible by identifying the zone axes and Kikuchi bands on a pattern [60, 61, 63, 64, 68, 69]. However, it should be noted that Kikuchi patterns in TEM form after the incoming beam diffracts and travels the sample width, whereas they stem from backscattered electron diffraction at the surface of a bulk sample in EBSD in SEM [63].

Two steps are necessary to interpret a Kikuchi pattern. In the first step, the pattern is indexed, and in the second one, crystallographic orientation of the sampled volume is determined with respect to the sample axes. Since gnomonic projection is used to project the Kikuchi pattern onto the screen, indexing requires the pattern center (PC) and the sample to screen distance (SSD) to be known. SSD and the coordinates of the PC are found by a calibration procedure. To index a pattern, any point on the pattern needs to be designated as the end point of a vector drawn from the pattern source point (SP) in the sample, the point that the electron beam hits to the sample (Figure 2.16). The three components needed to draw the vector are x and y on the pattern with respect to the PC and z is SSD, i.e. magnitude of the normal drawn between PC to SP. Determination of x and y components of the vector are performed on a computer screen by user, since the captured EBSD pattern is transferred to the computer in the current EBSD set-ups. Therefore, the user can mark several zone axes on the pattern (x and y components with respect to PC). The zone axes marked on the 2-dimensional computer screen are transferred to the 3-dimensional (3D) vectors to relate the pattern to the sample axes. This process requires a reference sample axes (X_s, Y_s, Z_s), a screen (pattern) axes (X_p, Y_p, Z_p), and a third set of axes necessary to relate the reference axes and the screen axes. The third one is set as microscope axes (X_m, Y_m, Z_m). SP constitutes the origin all these three sets of axes. Conventionally, Z_s can be defined normal to the sample surface (normal direction, ND); X_s can be made parallel to the rolling direction of a rolled sample (rolling direction, RD); and Y_s is orthogonal to X_s and Z_s, (transverse direction, TD).

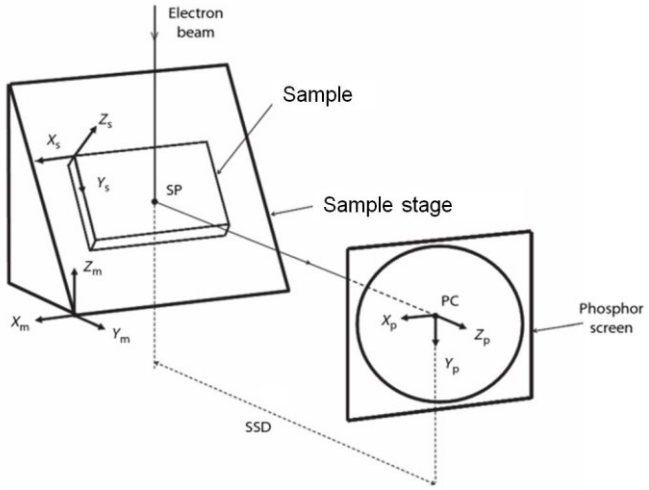

Figure 2.16 A schematic showing the necessary components of EBSD geometry to interpret EBSD patterns. (X_s, Y_s, Z_s), (X_p, Y_p, Z_p) and (X_m, Y_m, Z_m) are sample, pattern and microscope axes, respectively. SP: Pattern source point. PC: Pattern center. SSD: Sample to screen distance. After Ref. [63].

In terms of the microscope axes, the electron beam can define Z_m, X_m can be made parallel to X_s and Y_m traverses the sample stage. By designing the sample stage geometry, X_s, and hence X_m, can be made parallel to X_p. By using the angular relations between Z_s, Z_p and Z_m, it is possible to make transformation between these axes and obtain 3D vectors. Scalar product of such vectors provides the mutual angles between these zone axes. Since the crystal structure of the sample is known, by using a table showing all possible angle relations for this particular crystal structure, the zone axes on the pattern can be found and indexed. In the second step, the crystallographic orientation of the sampled volume needs to be determined with respect to the sample axes. As the zone axes are indexed now, cross product of two known zone axes results in the direction of the vector normal to them. By measuring the angles between each of these vectors and X_s, Y_s, Z_s, a 3 x 3 matrix is obtained representing the orientation of the crystal with respect the sample axes. For instance, α_1, β_1 and γ_1 are the angles between [100] of the crystal axes and X_s, Z_s and Y_s, respectively, whose cosines form the first column of the matrix. The second and third columns of the matrix consists of cosines of α_2, β_2, γ_2 and those of α_3, β_3,

γ_3 which are the angles between [010] and X_s, Y_s, Z_s, and [001] and X_s, Y_s, Z_s, respectively (Fig. 2.17) [61-63].

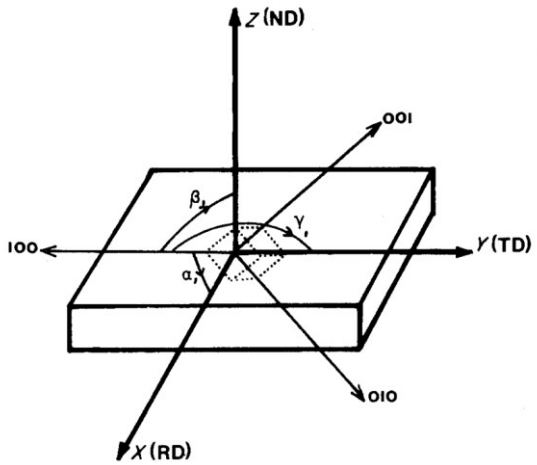

Figure 2.17 A crystal unit cell is shown in a sample. Determining the orientation of a crystal in a sample requires knowledge on the relation between their respective axes. X, Y, Z: Sample axes. [100], [010], [001]: Crystal axes. α_1, β_1 and γ_1: angle between [100] and X, Z, Y, respectively. α_2, β_2, γ_2 and α_3, β_3, γ_3 are not shown in the figure which are angles between [010] and X_s, Y_s, Z_s, and [001] and X_s, Y_s, Z_s, respectively [62].

Kikuchi patterns can also be interpreted automatically, which does not necessitate manual zone axes marking. For this purpose, the Kikuchi bands in the pattern are detected by using Hough or Radon transform of the image followed by calculation of angles between these detected bands and comparing them with a table of all possible angle relations for the respective crystal structure. After indexing is complete, every individual pixel in the image can be related to an external reference axes. Automatic interpretation of Kikuchi patterns is often necessary for orientation microscopy and mapping on a large area of the sample [61, 63, 64].

Orientation microscopy is acquisition and storage of orientation information of a sample according to a predefined sampling grid which can be hexagonal or square. Measurement spots on the sample surface can be located by either stage or beam control in which the sample stage is moved under the stationary electron beam according to the chosen sampling grid or vice versa, respectively. Stored data for every measurement spot include orientation, phase identity, spatial coordinates, diffraction pattern quality metric, and confidence index. Once the orientation

data is obtained, it can be presented as an orientation map providing an image of orientation with respect to the sampling grid. A number of analyses can be performed and demonstrated on an orientation map. For example, Figure 2.18 shows an EBSD study performed at the cross section of a $CuGaSe_2$ (CGS) absorber layer of a thin film solar cell. Cross-sectional SEM image is shown in Figure 2.18a which demonstrates all layers of the solar cell.

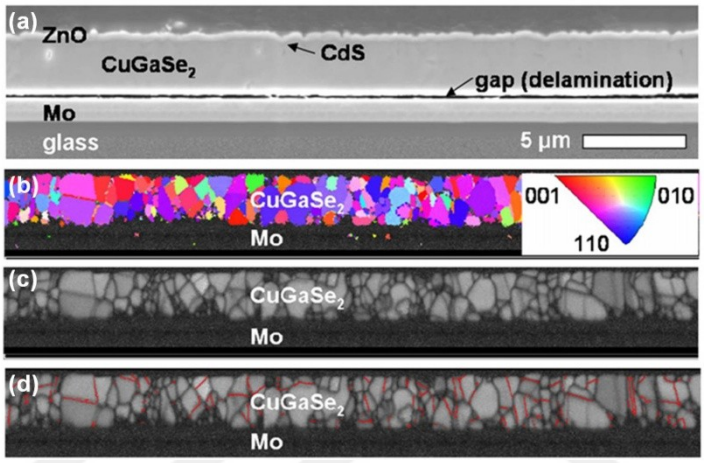

Figure 2.18 (a) Cross-sectional SEM image of a $CuGaSe_2$ (CGS) thin film solar cell. (b) Orientation and (c) pattern quality maps of the same CGS thin film region. (d) The same pattern quality map shown in (c) with Σ3 grain boundaries highlighted by red lines [70].

A color-coded orientation distribution of the CGS layer is shown in Figure 2.18b. Grains with different orientations are obvious, since orientation change and color change are linked. Red, green and blue colors are assigned to the 001, 010 and 110 corners of the stereographic unit triangle, respectively. These three orientations indicate the crystal orientations those are parallel to a selected sample direction (inverse pole figure). Orientations fall between these three primary components are represented by a mixture of red, green and blue. Orientation maps can be obtained for all sample directions, i.e. X (RD), Y (TD), Z (ND). Pattern quality map of the sampled region is shown in Figure 2.18c. A pattern quality map displays a numerical estimate of image quality. They are obtained by normalizing the range of gray scale values to the image quality values in the map; therefore, bright and dark regions in a pattern quality map indicate high and low pattern quality in the map, respectively. Consequently, grain boundaries are seen

as dark lines in a pattern quality map, since they are crystallographic transition regions between two grains with different orientations giving relatively poor pattern quality than grain interiors. It is also possible to examine grain boundary types and highlight the ones relevant to the purpose of the analysis. An example is shown in Figure 2.18d in which Σ3 grain boundaries are highlighted by red lines on the same pattern quality map shown in Figure 2.18c. The Σ symbol is used to classify grain boundaries by the coincidence site lattice (CSL) model (Appendix A). According to the CSL model, certain misorientations between two grains result in coincident lattice sites at the grain boundary between them, and Σ can be defined as the reciprocal density of the coinciding sites at the grain boundary. Identification of the CSL grain boundaries is often made by EBSD since some of the CSL grain boundaries are known to have beneficial properties, for instance, in terms of their electrical behavior as studied in Chapter 3 of this dissertation. Apart from these analyses, orientation mapping also allows studying grain size distribution statistics, phases in multiphase materials, phase boundaries and other functions defined by the user [63, 66, 70].

2.2.3 Cathodoluminescence Spectroscopy and Microscopy

Cathodoluminescence (CL) is the light emission from a radiative relaxation of the excited states generated in a luminescent material by a high-energy electron beam often inside electron microscopes. Applications of CL spectroscopy and microscopy include examining impurity concentration and doping, defect mapping and their effect on the electronic properties, and stress distribution analysis in epitaxial layers. In CL microscopy, the emitted light (in the ultraviolet, visible and near-infrared ranges of the electromagnetic spectrum) from a sample due to the incident electron beam is recorded as a luminescence image, and CL spectroscopy enables obtaining a luminescence spectrum from the region of interest. CL measurement is a contactless technique and can be performed with different electron sources, such as in TEM, SEM or STM. The energy of the electrons used in different tools determines the beam-sample interaction volume and in turn affects the lateral resolution of the CL measurement. By coupling

a CL measurement with other techniques, such as EBSD, electron beam induced current and electron microprobe analysis, allows a complementary analysis on the same sample region [44, 70-72].

In semiconductors, the light emission occurs due to radiative recombination of electron-hole (e-h) pairs. Once the electron beam strikes to a semiconductor sample, elastic and inelastic electron scattering processes occur, and inelastic scattering process of electrons is responsible for e-h pair generation within a sample volume. After the excess carriers are generated, they thermalize, diffuse in the material, and finally recombine by radiative or non-radiative processes [71-74]. The generation (or excitation) volume can be estimated by determining the penetration depth of the incident electron by

$$R_e = (k/\rho)E_b^{\alpha}, \tag{2.17}$$

where E_b is the energy of the incident electron beam, ρ is the density of material, and two constants, k and α depend on the atomic number of the sample material and E_b. And, the local generation rate of e-h pairs is

$$G = \frac{V_b I_b (1-\gamma)}{eE_i} = \frac{V_b I_b Q(1-\gamma)}{eE_g}, \tag{2.18}$$

where V_b is the electron beam voltage, I_b is the beam current, e is the electronic charge, E_i is the ionization energy, E_g is the bandgap of the semiconductor, Q is the quantum efficiency for e-h pair generation, and γ is the loss in the electron beam energy due to backscattered electrons from the sample [72, 74].

CL emission processes can be divided into two groups: intrinsic and extrinsic. Intrinsic CL emission occurs due to the recombination of e-h pairs across the bandgap. Therefore, the peak CL intensity occurs at photon energy $hv_p \simeq E_g$. On the other hand, extrinsic CL emission occurs due to transitions involving shallow or deep states in the bandgap that stem from defects or impurities in the material. Because extrinsic CL emission is due to the defects or impurities in

the material, the emission features are characteristic of these extrinsic factors [71, 72, 74]. A schematic of the radiative transitions is shown in Figure 2.19. In process 1, an electron excited above the conduction band reaches thermal equilibrium with the lattice which may result in phonon assisted photon emission or only emission of phonons. Process 2 shows an intrinsic CL process in which electrons from conduction band and holes from valence band recombine. Process 3 is an excitonic decay that can be seen at low temperatures. Processes that result in extrinsic CL emission are 4, 5 and 6. These transitions involve localized donor or acceptor impurity states in the bandgap. The fact that these shallow levels can be very close to the band edges requires CL measurements to be performed at cryogenic temperatures; therefore, a distinction between transitions involving shallow levels and band-to-band transitions can be made. Although shallow donor and acceptor levels are shown in Figure 2.19, extrinsic CL emission can also occur due to deep acceptor and donor levels. In addition, apart from impurities, localized levels in the bandgap can also exist due lattice defects, such as dislocations and vacancies. And finally, Process 7 shows radiative de-excitation of an impurity [72, 74].

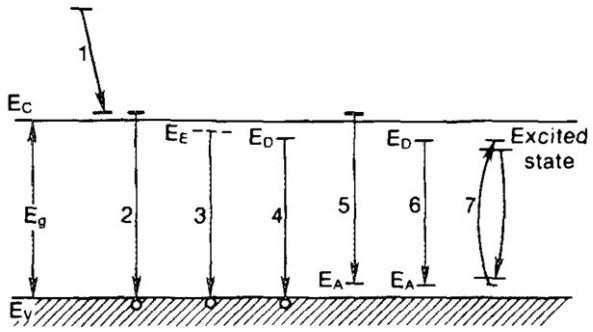

Figure 2.19 Schematic of radiative transitions. Process 1: Thermalization of an electron which may result in phonon assisted photon emission or only emission of phonons. Process 2: Band-to-band recombination, i.e. intrinsic CL emission. Process 3: Excitonic decay at low temperatures. Process 4-6: Transitions involving localized impurity states in the bandgap, i.e. extrinsic CL emission. Process 7: Radiative de-excitation of an impurity. E_C, E_V, E_E, E_A, E_D are energy levels of conduction band edge, valence band edge, exciton, acceptor states and donor states, respectively [72, 74].

Making a quantitative CL analysis is nontrivial because recombination of e-h pairs can also occur by nonradiative recombination processes, such as multiple phonon emission and

Auger recombination. In fact, the radiative recombination efficiency (internal quantum efficiency), η is given by

$$\eta = \tau/\tau_{rr} = [1 + (\tau_{rr}/\tau_{nr})]^{-1}, \quad (2.19)$$

where τ is the minority carrier lifetime, and τ_{rr} and τ_{nr} are radiative and nonradiative recombination lifetimes, respectively. η further determines the rate of CL emission (L_{CL}), which is given by

$$L_{CL} = f\eta G I_b/e, \quad (2.20)$$

where f is a function for CL detection system correction which accounts for lost photons, for example, due to reflection, G is the local generation rate of e-h pairs, I_b is the electron beam current, and e is the electronic charge. In addition, the radiative recombination efficiency η is affected by a number of factors, such as temperature and defects. Consequently, the nonradiative recombination processes can be analyzed by the contrast between radiative and nonradiative recombinations sites in a CL image [44, 72-74].

CL measurements are mostly performed in an SEM (SEM-CL). Although CL measurements in TEM (TEM-CL) enables about one order of magnitude higher lateral resolution than SEM-CL due to the reduced sample thickness, the high energy and small diameter of the electron beam in TEM, limited space of the instrument and small sample size make CL signal collection difficult in TEM [44, 71]. Schematic of an SEM-CL set-up is shown in Figure 2.20. CL signal from a sample is collected either by placing an optical fiber or a mirror (ellipsoidal or parabolic) above the sample. The signal is transported to the detector system outside of the SEM chamber by a light guide. The detector system consists of a monochromator and detectors.

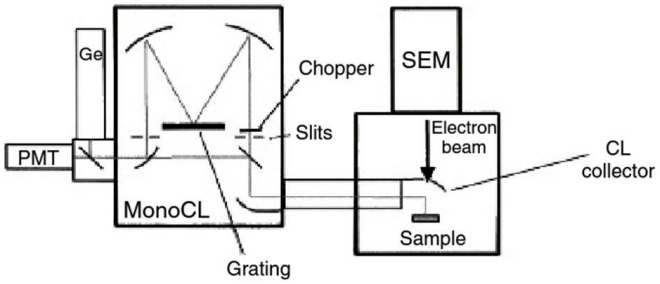

Figure 2.20 Schematic of a cathodoluminescence (CL) measurement set-up in a scanning electron microscope (SEM). An optical fiber or a mirror (CL collector) located above the sample collects the CL signal and sends it to the detector system -monochromator (MonoCL) and detectors (PMT: Photomultiplier tube and Ge: Germanium detector). An image is formed on a cathode ray tube by the CL signal [71].

A CL image can be obtained either by modulating the intensity of the cathode ray tube by the CL signal sent from the detectors or by implementing a CCD camera. Monochromatic or panchromatic images can be obtained by utilizing one or all CL emission wavelengths. Fast data acquisition times (typically 0.5-40 s) in recent CL set-ups is accomplished by using a photodiode or an array of diodes instead of a photomultiplier tube (PMT). A fast data acquisition is particularly important when synchronizing the electron beam movement and the CL signal acquisition for performing CL spectral imaging [71, 73]. To minimize the thermal broadening effects on the CL spectra, a cryostat can be used to control the temperature of the sample at 6 K to 300 K [71, 74].

2.2.4 Raman Spectroscopy

Raman spectroscopy is a vibrational spectroscopy technique that has applications in structural analysis of organic and inorganic materials, and the measurement of crystallinity of solids. Because Raman spectroscopy is a sensitive technique to crystal structure, factors affecting the crystal structure, such as stress in thin films, can be examined [44]. Raman spectroscopy is based on Raman scattering which is inelastic scattering of light from lattice vibrations (phonons). In elastic light scattering (Rayleigh scattering), frequency of the light incident onto the optical medium is not changed, whereas in inelastic light scattering, the incident light changes its frequency in the process of being scattered by the optical medium.

There are two types of inelastic light scattering events: Stokes and anti-Stokes. In Stokes scattering, a phonon is emitted, while in an anti-Stokes scattering a phonon is absorbed [75-78]. If ω_1, k_1 and ω_2, k_2 are angular frequency and wave vector of incident and scattered photons, respectively, and Ω and q are those of a phonon, conservation of energy and momentum requires that

$$\omega_1 = \omega_2 \pm \Omega, \tag{2.21}$$

$$k_1 = k_2 \pm q. \tag{2.2}$$

In Equations (2.21) and (2.22), $+$ sign denotes phonon emission (Stokes scattering) (Fig. 2.21), and $-$ sign denotes phonon absorption (anti-Stokes scattering). Consequently, during a Stokes scattering event, the frequency of the scattered photon is reduced, whereas during an anti-Stokes scattering event, the frequency of the scattered photon is increased [75].

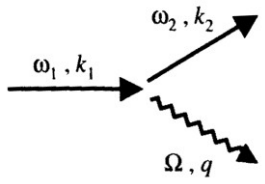

Figure 2.21 Stokes scattering process. A Stokes scattering event results in emission of a phonon and down-shift in frequency of the incoming photon. Straight arrows: photons. Wiggly arrow: phonon. ω_1, k_1 and ω_2, k_2 are angular frequency and wave vector of incident and scattered photons, respectively, and Ω and q are those of a phonon [75].

A schematic Raman spectrum can be seen in Figure 2.22. It should be noted that the x-axis shows wavenumber (cm^{-1}) which is a common unit used for vibrational frequencies and it is the reciprocal of wavelength (λ), $1/\lambda$.

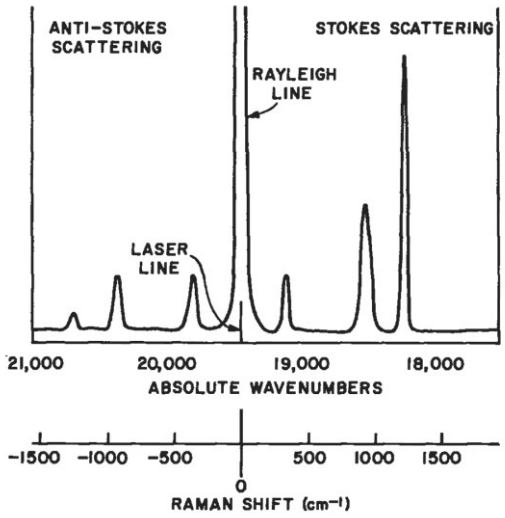

Figure 2.22 Schematic of a Raman spectrum. Raman lines arising from Stokes and anti-Stokes scattering appear at lower and higher wavenumbers than the central Rayleigh line, respectively. Raman shift is the wavenumber difference between the Rayleigh line and a Raman line and displayed by setting the Rayleigh line at zero [78].

Rayleigh scattering is seen as a strong line in the center of the spectrum. Stokes and anti-stokes scattering result in Raman lines at higher and lower wavenumbers than the Rayleigh line, respectively, and they are located symmetrically on the opposite side of the Rayleigh line. Anti-Stokes scattering event involves the existence of thermally activated vibrations; hence, it has a less occurrence probability than Stokes scattering. Therefore, usually Stokes scattering is measured, and the result is presented as the amount of shift (cm^{-1}) of the Raman line from the Rayleigh line which is set to zero [75-78].

In a Raman spectrometer, a laser is used as the light source incident onto a sample to obtain strong signal (Fig. 2.23). Scattered photons are focused and directed to a scanning spectrometer. A photon-counting detector determines the number of photons emitted at a particular wavelength and the data is sent to a computer for analysis [75]. Sample to be measured can be in gas, liquid or solid phase, and sample preparation steps are usually minimal. Coupling a Raman spectrometer with an optical microscope enables studying spatial regions on a sample [76, 77, 79].

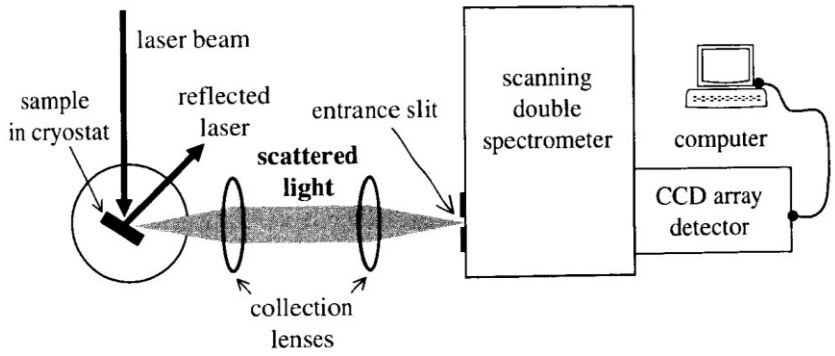

Figure 2.23 Schematic of a typical Raman spectroscopy set-up. A laser beam is incident onto a sample from which it is scattered. Scattered light is focused and directed into a scanning spectrometer. A photon-counting detector determines the number of photons emitted at a particular wavelength and sends the data to a computer for analysis [75].

2.2.5 UV/VIS/NIR Spectroscopy

Apart from being used as an analytical instrument in chemistry research [80], ultraviolet/visible/near-infrared (UV/VIS/NIR) spectroscopy can also be used for experimental determination of optical constants, refractive index and absorption coefficient, α by obtaining the reflectance, $R(\omega)$ and transmittance, $T(\omega)$ of an optical medium, where ω is the frequency of light [81].

A spectrometer consists of light sources, a monochromator or polychromator, detectors, and optical elements, such as mirrors, to manipulate the light beam. Two different configurations for a spectrometer can be seen in Figure 2.24. Light emitted from the source is made incident onto a sample either directly after it is emitted (Fig. 2.24a) or after passing through a monochromator (Fig. 2.24b). Therefore, in the first configuration the reflected or transmitted light from the sample is wavelength dispersed, before being sent to the detector, whereas in the second configuration the detector receives the signal directly from the sample [81]. Wavelength range of UV/VIS/NIR spectroscopy is 190 nm to 2500 nm (UV: 190 nm - 350 nm, VIS: 350 - 800 nm, NIR: 800 nm - 2500 nm), and light sources for this wavelength range can be covered by a deuterium lamp for UV region and a tungsten-halogen lamp for VIS/NIR

regions. A photomultiplier and a PbS detector can be used as detectors for the UV-VIS and NIR regions, respectively [80-82].

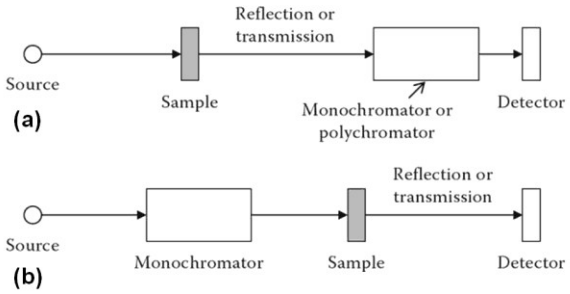

Figure 2.24 Schematic of a spectrometer in two different configurations. (a) Reflected or transmitted light from the sample is wavelength dispersed before it is sent to the detector. (b) Wavelength dispersed light is incident onto the sample and reflected or transmitted light is sent to the detector directly [81].

Once $R(\omega)$ and $T(\omega)$ spectra of an optical medium are obtained, its absorption coefficient α can be calculated by using the following relation

$$T = (1 - R_1)e^{-\alpha l}(1 - R_2), \tag{2.3}$$

where R_1 and R_2 are the reflectivities of the front and back surfaces of the sample, respectively, and l is the thickness of the absorbing medium. In case of a semiconductor sample, obtained absorption coefficient α can be used for determining the bandgap of the semiconductor. For this purpose, α^2 vs. photon energy or $\alpha^{1/2}$ vs. photon energy graphs are plotted for a direct bandgap or an indirect bandgap semiconductor, respectively, and the bandgap can be obtained by extrapolating the linear portion of the curve to zero absorption - an example from a direct bandgap semiconductor is shown in Figure 2.25 [75].

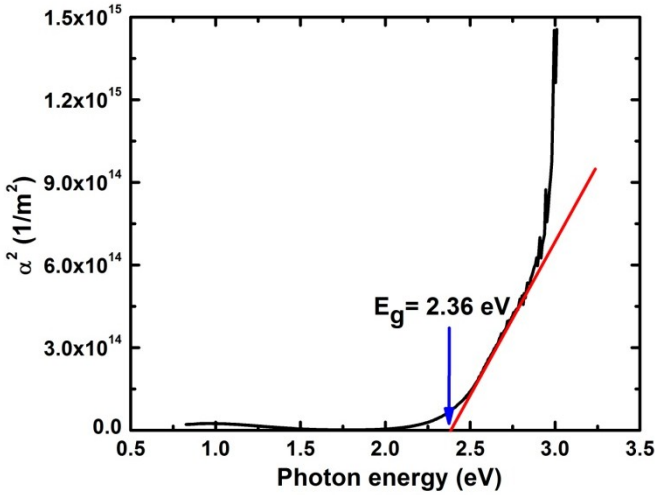

Figure 2.25 Example for determining bandgap (E_g) of a semiconductor by using absorption coefficient α. The graph belongs to a CdS thin film deposited on a glass substrate by chemical bath deposition method. Since CdS is a direct bandgap semiconductor, α^2 vs. photon energy graph is plotted. The red line shows extrapolation of the linear portion of the curve to zero absorption to determine the bandgap.

2.2.6 Glancing Angle X-ray Diffraction

Glancing angle X-ray diffraction (GAXRD) is a diffractometer geometry used for near-surface structural characterization. The idea behind GAXRD is reducing the penetration depth of X-ray ($z_{1/e}$) into a sample to obtain structural information from a limited volume of the sample. This is achieved by reducing the incidence angle of the X-ray (ϕ) onto the sample surface. X-ray penetration depth is defined as the depth that the intensity of X-ray (I) reduces to $1/e$ of its value at the surface. Intensity of X-ray as a function of distance from the sample surface (z) can be expressed as

$$I = I_0 exp(-\mu z/sin\phi), \tag{2.24}$$

where I_0 is the intensity of the X-ray at the sample surface and μ is the absorption coefficient of the material investigated. And, X-ray penetration depth can be written as

$$z_{1/e} = sin(\phi)/\mu. \tag{2.25}$$

When the incidence angle of the X-ray is lower than a few degrees, these relations are not valid, and below a critical incidence angle (ϕ_c) X-ray penetration depth reduces to a few nanometers due to total external reflection [83]. The critical incidence angle is specific for a particular material, since it depends on the refractive index of the material examined [83, 84].

Schematics of Bragg-Brentano geometry used for bulk structural characterization and a GAXRD geometry are shown in Figures 2.26a and 2.26b, respectively. This particular GAXRD geometry is known as grazing incidence angle asymmetric Bragg (GIAB). In Bragg-Brentano geometry, the X-ray beam is fixed, but the sample and the detector rotate to change the incidence angle in a way that the incidence angle of the X-ray and the angle of the detector are kept the same. However, in GAXRD geometry, the incidence angle of the X-ray is maintained the same and only the detector is rotated [46, 77, 83]. Although the signal intensity in GAXRD geometry is significantly lower than the Bragg-Brentano geometry, it has almost two orders of magnitude more surface sensitivity than the Bragg-Brentano geometry [83].

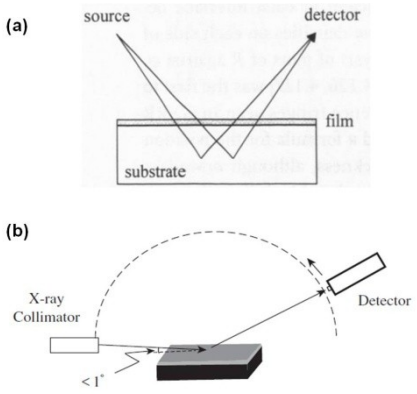

Figure 2.26 Schematics of (a) Bragg-Brentano [83] and (b) GAXRD [46] geometries. In Bragg-Brentano geometry, the X-ray beam is fixed, while the sample and detector are rotated. The incidence angle of X-ray and the angle of detector are maintained the same. However, in GAXRD geometry, the incidence angle of X-ray is fixed and only the detector is rotated.

CHAPTER 3

ELECTRONIC ACTIVITIES OF GRAIN BOUNDARIES IN MULTICRYSTALLINE $CuInSe_2$ INGOTS

Power conversion efficiency of polycrystalline thin film $Cu(In,Ga)Se_2$ (CIGS) solar cells have reached ~20% [1, 2] in laboratory keeping its leadership among other thin film solar cell technologies, such as CdTe and polycrystalline silicon solar cells (Figure 3.1).

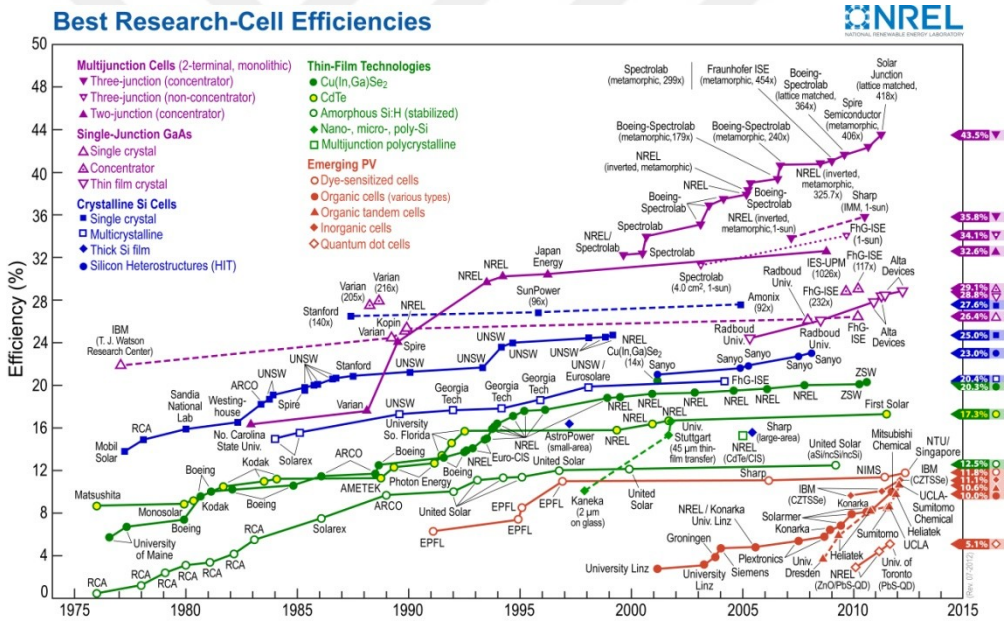

Figure 3.1 Research cell efficiency records chart [3].

Despite the intense research has been performed on chalcopyrite solar cells, there are still immature understanding on some of the fundamental properties of chalcopyrite materials, and electronic activities of grain boundaries (GBs) is one of them. Because obtaining a high efficiency 'polycrystalline' solar cell is not intuitive according to the classical understanding of electronic behavior of semiconductor GBs. GBs have various types of defects that introduce extra electronic states within the bandgap which strongly affect carrier transport and

recombination in semiconductors [5, 7]. Moreover, the best power conversion efficiency obtained from a single crystalline chalcopyrite solar cell is 13% [85], whereas its polycrystalline counterpart has marked ~20% [1, 2]. This comparison makes the GBs in chalcopyrites even more mysterious. Therefore, there has been effort in the field to understand the electronic behavior of chalcopyrite GBs.

In addition, Na impurities, which are required for achieving a high efficiency chalcopyrite solar cell (i.e. sodium effect), have been found in a higher concentration at the GBs than grain interiors (GIs) [8, 9]. Although a comprehensive explanation on the sodium effect is rare, it mainly enhances the open circuit voltage and fill factor of the solar cell. The source of Na is the soda-lime glass (SLG) substrate which is a commonly used substrate for chalcopyrite solar cells and Na diffuses from SLG into the chalcopyrite absorber layer during high temperature film growth [9, 12]. GB diffusion was proposed as the Na diffusion mechanism, and it was shown that when the Na concentration was above ~1 at.%, device performance degraded possibly formation of a Na-related secondary phase in the absorber [86]. Consequently, the effect of Na on electronic properties of chalcopyrite GBs need to be taken into account for a complete understanding of electronic properties of GBs.

In this chapter, the electronic properties of Σ3, ~Σ3 and Σ9 GBs (Appendix A) in a Bridgman-grown multicrystalline Na-free $CuInSe_{2.1}$ wafer were investigated. Investigating the electronic properties of GBs in Na-free CIS was important to prevent any unexpected and uncontrolled effect of Na on the electronic properties of chalcopyrite GBs, for instance, through a Na-related secondary phase segregation at the GBs which was theoretically predicted [11]. It is shown that the electronic properties of the GBs investigated were dependent on the amount of defects at the GB. The Σ3 GB was neutral and was not a recombination center which was an expected result from a low Σ GB. However, once a GB deviated from the Σ3 GB geometry accompanied with an increase in the amount of defects at the GB, it became charged and increased recombination activity was observed, which was the case for the ~Σ3 and Σ9 GBs.

Therefore, the electronic activities of the chalcopyrite GBs investigated in this chapter can be mostly explained by the classical semiconductor GB model [4-6] which is based on the existence of interface states at the GB and their consequences on the GB electronic properties. In terms of device performance, obtaining highly efficient devices from polycrystalline chalcopyrites can be reasoned by the abundance of the Σ3 GBs in this material [87]. Because stacking fault formation energy in chalcopyrites is low [88] and twin GBs, whose formation is based on stacking faults, are characterized as Σ3 according to the coincidence site lattice model [89] (Appendix A).

3.1 Introduction

3.1.1 Grain Boundaries in Chalcopyrite Solar Cell Materials

Models used to explain GB behavior in chalcopyrite solar cell materials can be divided into three groups: electrically active GB (e-GB) model [4-6], valence band offset (VBO) model [90, 91] and electrically benign GB (EB-GB) model [10]. While the e-GB model can be considered as a classical understanding of semiconductor GBs applied to different semiconductors, VBO and EB-GB models were proposed particularly for chalcopyrite GBs.

According to the e-GB model, trapped charges at the GBs lead to band bending and form potential barriers. While every grain inside a polycrystalline material can be considered as a single crystalline material, periodic crystal structure and potential is disturbed at the grain boundaries as well as at the surface of the material. Consequently, a crystallographic transition takes place between grains with different orientations and it results in various types of defects, such as dislocations and vacancies, located at the GBs. These defects introduce spatially localized extra electronic states within the bandgap because the crystal periodicity does not exist at the GBs, and hence the extra states do not have to obey the periodicity of the potential. The extra electronic states within the bandgap tend to trap carriers and they are called *trap states* or *interface states*.

A trap can be a donor or an acceptor depending on its occupancy and energetic position relative to the Fermi level (E_F) of the semiconductor. It is considered as a donor, if it is neutral and becomes positively charged by donating an electron, whereas it is considered as an acceptor, if it is neutral and becomes negatively charged by accepting an electron. This notation can be easily pictured by defining a neutrality level (ϕ_0) that is the energy level up to which states are filled when the interface is neutral. ϕ_0 of an interface and E_F of a bulk semiconductor are usually different; therefore, when an interface (i.e. GB) and a bulk semiconductor (i.e. grain) are brought together, charge transfer takes place to bring them into equilibrium. If $\phi_0 > E_F$, the traps are donor like; they trap holes and the GB is positively charged. If $\phi_0 < E_F$, traps are acceptor like; they trap electrons and the GB is negatively charged. An example for a *p*-type semiconductor in case of $\phi_0 > E_F$ can be seen in Figure 3.2. Since $\phi_0 > E_F$, upon contact between the GB and the bulk semiconductor grains, electron transfer will occur until the E_F of the grains and ϕ_0 of the GB are equalized. As electron transfer proceeds, the positive charge is left behind forming a space-charge region (SCR) on both sides of the GB to preserve charge neutrality. As a result, an electric field is established that prevents further electron flow and band bending occurs at the GB [5, 6, 92].

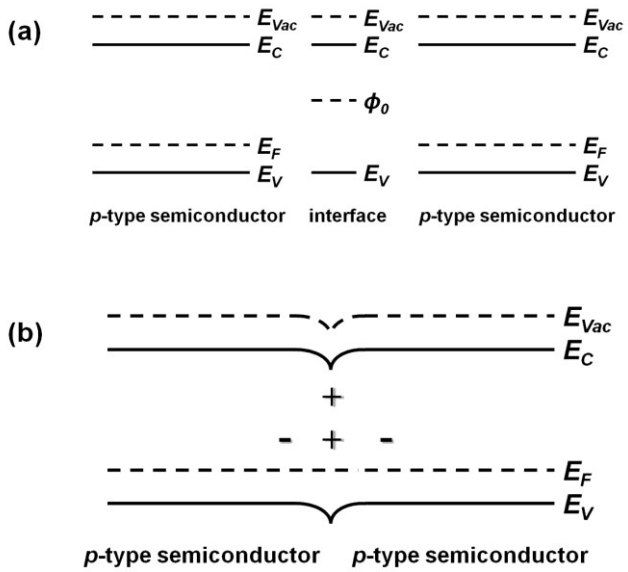

Figure 3.2 Band bending formation at the interface (i.e. grain boundary) of two bulk *p*-type semiconductor (i.e. grains). (a) Before the interface and bulk semiconductors are in contact. (b) After they are contacted. E_{Vac}: Energy level of the vacuum, E_C: Energy level of the conduction band minimum, E_V: Energy level of the valence band maximum, E_F: Energy level of the Fermi level, ϕ_0: Neutrality level of the interface. Plus and minus signs indicate the positive and negative charge, respectively. After Ref. [5].

The potential barrier developed at the GBs affects the carrier transport in polycrystalline semiconductors by reducing the carrier mobility from its value measured in single crystal materials [4, 93]. In addition, band bending at the GBs forms a potential well for the minority carriers which draws them to the GBs and increases the probability of their recombination with the trapped majority carriers [5]. However, GB potential barrier reduces under light. Upon illumination photogenerated excess minority carriers near the GBs drift towards GBs by the electric field gradient in the SCR and recombine with the majority carriers trapped at the interface states. As a result, GB charge and thus potential barrier reduces due to the recombination event [5, 6, 93].

Temperature dependent Hall and conductivity measurements performed on chalcopyrite GBs in different laboratories showed a barrier height of 22 meV to 300 meV [94]. Obtained barrier height was interpreted as downwards band bending due to trapped positive

charge at the GBs according to the e-GB model. Up to 300 meV barrier height was also measured by other techniques, such as Kelvin probe force microscopy (KPFM), which is in accordance with the barrier height deduced from temperature dependent Hall and conductivity measurements. In addition, KPFM showed that chalcopyrite GBs are usually positively charged, and hence downwards band bending occurs [94, 95]. Jiang et al. [96] measured downwards band bending at the GBs of CIGS and proposed that local built-in potential on GBs can extend the minority carrier collection angle. Positively charged GBs can draw the electrons that are far away from *p*-*n* junction, and then can carry them to the junction through a conduction path in the GB, whereas holes are repelled away from the GB. A similar downwards band bending on GBs of a random textured CIGS thin film was also measured by Hanna et al. [97]; however, their interpretation was completely different (Fig. 3.3). They suggested that positively charged GBs draw electrons and cause their enhanced recombination at the GBs. In the same study, they also measured upwards band bending, i.e. a negatively charged GB, but on the GBs of a (220/204) textured CIGS thin film. It was claimed that negatively charged GBs repel electrons and reduces GB recombination.

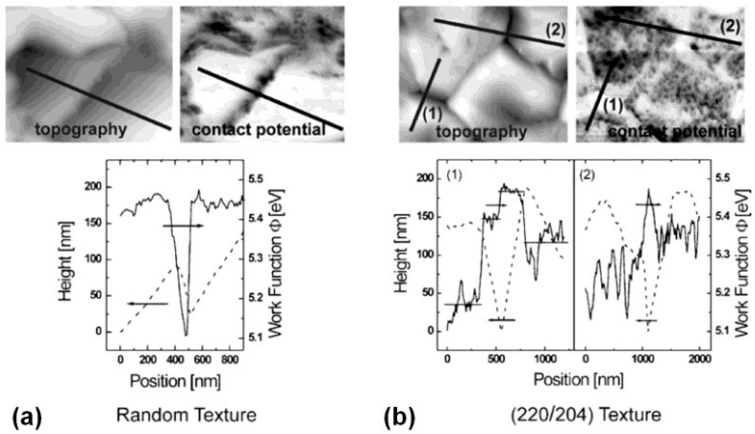

Figure 3.3 Topography and contact potential (CP) images obtained by Kelvin probe force microscopy measurements, and height and work function line profiles extracted from the same images, respectively, on the locations indicated by the black lines. (a) a random texture $Cu(In,Ga)Se_2$ (CIGS) film and (b) a (220)/(204) textured CIGS film. The lightest color indicates the highest value in the images [97].

This view was supported by the former studies reporting that (220/204) textured CIGS thin film leads to higher efficiencies. Kawamura et al. [98] proposed upwards band bending at the CIGS GBs as well according to their electron beam induced current (EBIC) measurement that exhibited the GBs brighter than GIs which means less recombination at the GBs. Consequently, the experimental results on chalcopyrite GBs have been be explained by using the e-GB model; however, the interpretations are conflicting.

Valence band offset (VBO) model is a first principles modeling study of Persson and Zunger [90, 91]. It is predicted that a hole energy barrier of 200 – 400 meV is located at the CIS GBs, whereas the conduction band offset is negligible (Fig. 3.4). Therefore, GBs expel holes and create a recombination-free zone for electron transport.

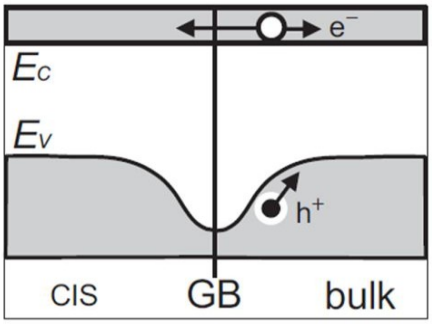

Figure 3.4 Schematic band diagram of a neutral grain boundary (GB) in $CuInSe_2$ (CIS) drawn according to valence band offset model [95]. E_C: Energy level of the conduction band (CB) minimum, E_V: Energy level of the valence band (VB) maximum, e^-: electron at CB, h^+: hole at VB.

The proposed charge-neutral hole barrier is due to the reduced repulsion between Cu *d* and Se *p* orbitals that form valence band maximum (VBM) particularly for a GB composed of two (112) oriented surfaces facing each other. GBs can be generally considered as surface-like structures regardless of their composition and defect chemistry and polar (112) surfaces are the most stable surfaces in chalcopyrites. Due to their polar nature, they are reconstructed by charge neutralizing Cu vacancies that have low formation energy in chalcopyrites. Removal of Cu atoms via vacancies reduces the repulsion between Cu *d* and Se *p* orbitals and lowers the VBM

creating a charge-neutral hole barrier. It should be noted that hole barrier only exists at cation terminated (112) GBs. Anion terminated $(\bar{1}\bar{1}\bar{2})$ GBs are not predicted to have a hole barrier since they stabilize by III-on-Cu antisite defects which does not disturb the VBM as much as Cu vacancies. Scanning tunneling luminescence measurements performed by Romero et al. [99] showed reduced hole density at GBs of CIS which supports VBO model.

However, experimental results on Cu depletion at the GBs, which is a necessity for VBO model, are conflicting. While micro-Auger electron spectroscopy (AES) results of Hetzer et al. [100] showed almost 50% Cu depletion at the GBs of a CIGS thin film, Lei et al. [101] and Yan et al. [102] did not find any compositional difference between GIs and GBs of CIGS thin films by energy dispersive x-ray spectroscopy (EDS) in transmission electron microscope (TEM). In fact, it is not surprising that these results are conflicting because, the VBO model was constructed on the assumption that GBs are along the (112) planes; however, GB orientation was not a part of the characterization in these compositional studies other than the (112) GB studied by Yan et al. [102]. As a further step on their GB characterization, Yan et al. modeled the (112) GB structure that was investigated by TEM, and found only 10-30 meV difference in conduction band minimum (CBM) and VBM of the modeled bulk CIS and GB. In fact, as they mentioned in the paper, the (112) GB they studied did not have a polar surface termination; therefore, there was no extra driving force for the Cu vacancies to form. For that reason, if the GB surface has a polar termination, Cu depletion can happen and VBO model can still apply [102].

Supportive results for VBO model were mostly from studies performed on coincidence site lattice (CSL) GBs (Appendix A) in $CuGaSe_2$ (CGS). Particularly Σ3 GBs were used for these studies, because it was reasoned that the GBs with {112} planes can be described as twins, and twins are categorized as Σ3 according to the CSL model. Temperature dependent Hall mobility measurements performed on a Σ3 GB of a CGS bicrystal resulted in an activation

energy of 32 meV; however, there was not a band bending at the GB according to KPFM (Fig. 3.5) [103].

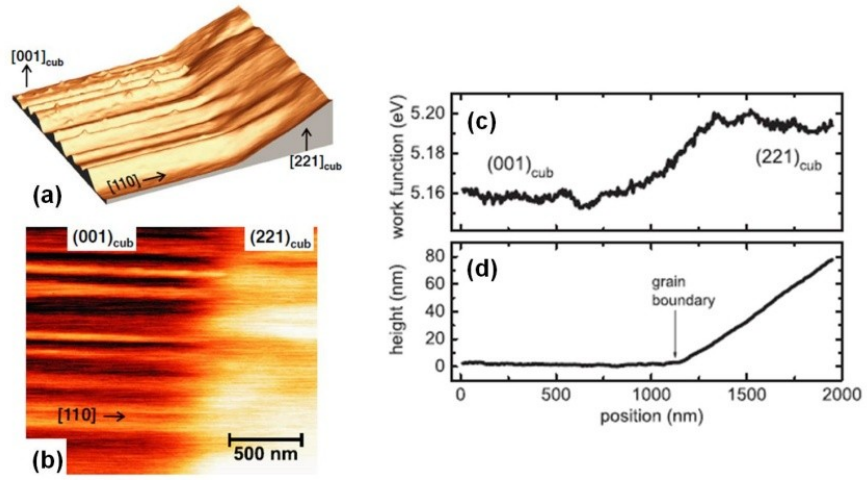

Figure 3.5 Kelvin probe force microscopy measurements on a Σ3 grain boundary in a $CuGaSe_2$ film grown on a GaAs wafer by metal organic vapor phase epitaxy. (a) Three dimensional topography image, (b) work function image, and work function (c) and topography (d) line profiles extracted from (b) and (a), respectively. After Ref. [103].

This result was in agreement with the VBO model which predicts a charge neutral hole barrier. In addition, it was also shown that holes tunnel through the potential barrier at Σ3 GB in CGS which was concluded by comparing the experimental and simulated temperature dependent conductivity measurement data [104]. Essentially, it is meaningful that there is not a charged induced band bending at Σ3 GBs, because the Σ3 GBs have the most coinciding lattice points, and hence least distortion. When the same measurements were performed on a Σ9 GB of CGS which has strained bonds that can be the source of charged defects, a work function dip of up to 90 meV was measured at the GB in contrast to charge neutral Σ3 GB (Fig. 3.6). The investigated Σ9 GB also showed a thermally activated barrier (~100 meV) which consists of thermionic emission and tunneling components [104, 105].

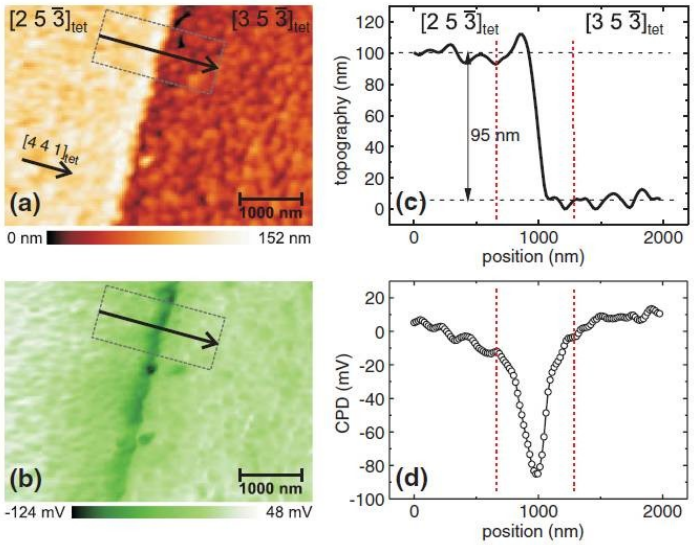

Figure 3.6 Kelvin probe force microscopy measurements on a Σ9 grain boundary in a $CuGaSe_2$ film grown on a GaAs wafer by metal organic vapor phase epitaxy. (a) Topography image and (b) contact potential difference (CPD) image. Averaged (c) topography and (d) CPD line profiles of obtained from areas in (a) and (b) [104].

Electrically benign GB (EB-GB) model proposed by Yan et al. [10, 102] predicts the absence of deep levels located at CIS GBs, even though the GB structure has dislocation cores, i.e. dangling, wrong, extra bonds. It was found that Se-Se wrong bonding is energetically unfavorable due to large electronegativity that leads to atomic relaxation and results in significant GB expansion. Consequently, predicted GB expansion prevents the dangling, wrong, and extra bonds to create deep levels (Fig. 3.7). When the calculations were made for the same CIS GB structure without relaxation, deep levels were present. Therefore, GBs in CIS are not recombination centers in contrary to typical semiconductors according to the EB-GB model, and hence it suggests that electrically active GB model does not apply to chalcopyrites. However, the EB-GB model does not completely exclude the prediction of the VBO model. Cu vacancy formation and resulting valence band offset can still be seen at a polar (112) GB, but at a smaller level than what VBO model predicts, since it was found that Cu vacancy formation energy is about 0.2 eV smaller for a GB than in the bulk. In addition, even though a GB can be

electrically benign, impurities segregated at the GBs can change their behavior which is detailed in the next section.

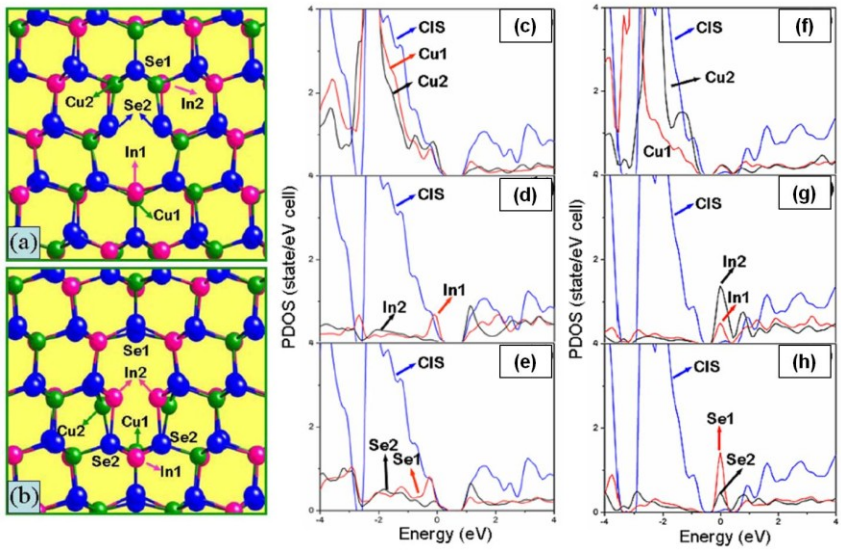

Figure 3.7 First –principles density functional theory calculations made for electrically benign grain boundary model. Atomic structures of dislocation core-containing grain boundaries (GBs) with (a) Se dangling bonds and (b) cation dangling bonds. Calculated projected density of states (PDOS) for (c) Cu, (d) In and (e) Se atoms around the dislocation core when the GB shown in (a) is relaxed, and that for (f) Cu, (g) In and (h) Se atoms around the dislocation core without atomic relaxation at the GB. After Ref. [10].

3.1.2 Sodium Effect in Chalcopyrite Solar Cells and Its Influence on Chalcopyrite Grain Boundaries

Initially the main purpose of using soda lime glass (SLG) substrate for CIGS solar cells was thermal expansion coefficient match between SLG and CIGS; however, it was realized that Na diffusing out of the SLG incorporates into CIGS layer during the high temperature (typically ≥500°C) film growth process and makes positive impact on the cell performance, so-called sodium effect [8, 12, 106]. Apart from the incidental effects of Na in CIGS, such as its influence on film texture and morphology [107-110], the most commonly observed outcome is an increase in open circuit voltage (V_{OC}) of the cells prepared in the presence of Na when compared to the Na-free ones, which is thought to be due to a Na-related increase in hole concentration (Fig. 3.8) [107-113].

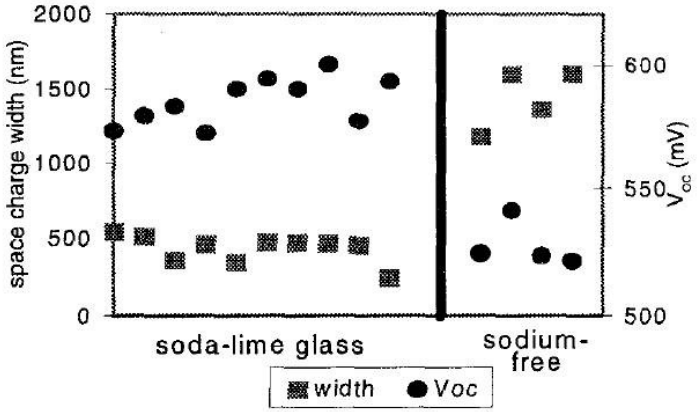

Figure 3.8 Open circuit voltage (V_{OC}) and space charge region width of Cu(In,Ga)Se_2 thin film solar cells prepared by coevaporation on soda-lime glass and sodium-free substrates [113].

Temperature-dependent admittance spectroscopy [112] and x-ray photoelectron spectroscopy (XPS) [114] results suggested that the increase in the hole concentration could be due to a Na-related acceptor state, particularly acceptor-type Na on In antisite (Na_{In}) defects. Predictions of a first principles study [11] were in agreement with these experimental studies on formation of acceptor-type Na_{In} defects. The same theoretical study also predicted that Na can help increasing the hole density by reducing the concentration of donor-type In on Cu antisite (In_{Cu}) defects through forming $Na_{(In_{Cu})}$, and furthermore a relatively higher band gap $NaInSe_2$ phase can precipitate from CIS through Cu substitution by Na, resulting in enhanced V_{OC}.

While the sodium effect is still being debated, efforts to understand the positive role of Na on cell performance are naturally coupled with theoretical and experimental investigations on the location of sodium in the films, and it is mostly found that Na mainly segregates on the surface and/or at the GBs of bulk crystal and thin film chalcopyrites [8, 9, 110, 114-119]. A first-principles study [10] on dislocation core containing GBs in CIS showed that segregation energy of Na to GBs is negative. Although scanning TEM-EDS did not show the presence of sodium at GBs within the detection limit of the measurement (~1 at.%) [101], field-emission AES (FE-AES) [115] and atom probe tomography (APT) (Fig. 3.9) [8, 9, 116, 119] detected up to 2.8 at.% Na at

the GBs of CIS and CIGS thin films, whereas it was at most 0.1 at.% in the GIs as shown by recoil spectrometry [110], XPS [114], and FE-AES [115].

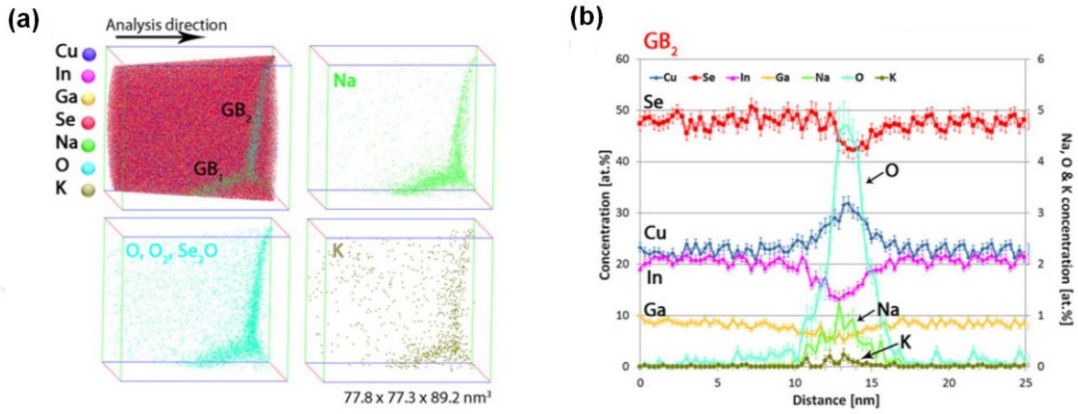

Figure 3.9 Atom probe tomography measurements close to two Cu(In,Ga)Se_2 grain boundaries (GBs). (a) Three dimensional elemental maps. (b) Compositional profiles across the GB_2 in (a) [9].

In addition, absence of significant Na amount in secondary ion mass spectroscopy (SIMS) [118] and scanning electron microscope (SEM)-EDS [117] analysis performed on the chalcopyrite single crystals that either had Na in the melt or post-growth annealed in Na atmosphere further showed that Na segregates to the surface of chalcopyrites.

The results on sodium diffusion into the chalcopyrite solar cells, particularly its segregation to the GBs, added a new aspect to the research being done on behavior of chalcopyrite GBs. Cathodoluminescence (CL) in TEM (TEM-CL) showed that GIs and GBs of Na-incorporated CIGS (Na-CIGS) showed relatively homogenous CL intensity, whereas Na-free CIGS had strong CL contrast at GBs and GIs indicating increased non-radiative recombination [97]. Persson and Zunger's first-principles study [90] predicted that charge-neutral Na_{Cu} defects can create a hole barrier and VBO model can still apply in the presence of Na. Although formation of polar (112) surfaces is not a common outcome of Na existence in chalcopyrites, they based their argument on experimentally seen pronounced (112) texture when Na diffuses into the films. Because Na lacks *d* orbitals, reduced *p* – *d* repulsion will still be seen at the GBs when Na_{Cu} defects form; hence, Na does not interfere with the VBO model. Fuertes Marrón et

al. [120] elaborated this view further and discussed that even though GB behavior is governed by VBO model, e-GB model-like band bending can be measured by KPFM. Na creates dipole layers at the GBs through formation of polar (112) surfaces; therefore, while a hole barrier could exist due to reduced *p* – *d* repulsion, a work function difference could also be present because of the existence of a dipole layer. On the other hand, according to the EB-GB model [10], Na helps charge carrier separation by making the GBs positively charged without causing non-radiative recombination. First-principles calculations on dislocation core containing GBs in CIS predicted that Na prefers interstitial sites where it is always positively charged and makes bonds with Se atoms that have dangling bonds. KPFM measurements (Fig. 3.10) supported these predictions; while a CIGS thin film grown on SLG had positive potential at its GBs, another one grown in the same batch, but on a borosilicate glass without Na, did not show any potential difference over its GBs. In contrast, insignificant GB potential variation in chalcopyrite thin films grown on SLG reported in the literature [97, 121].

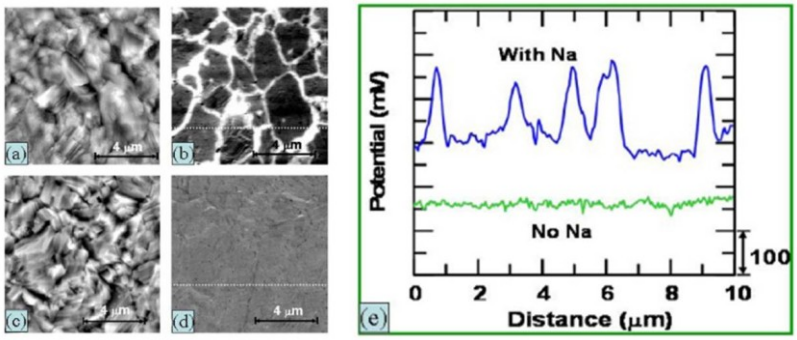

Figure 3.10 Kelvin probe force microscopy measurements of Cu(In,Ga)Se_2 (CIGS) films grown on Mo/soda-lime glass substrate (Na-CIGS) and Mo/borosilicate glass substrate (Na-free CIGS). (a) Topography and (b) potential images of Na-CIGS. (c) Topography and (d) potential images of Na-free CIGS. (e) Potential line profiles of the dotted lines in (b) (with Na) and (d) (No Na) [10].

As a result, currently there is not any high efficiency Na-free CIGS solar cell, and the mechanism of sodium effect is still under debate. Various experimental techniques have shown that Na mostly resides at the GBs. Therefore, the questions asked on chalcopyrite GBs should

be evaluated by considering Na impurities at GBs. However, theoretical and experimental studies on Na-chalcopyrite GBs are rather insufficient and conflicting.

3.2 Experimental Details

The sample used for this study was a Na-free CIS wafer with cm-sized grains cut from a multicrystalline CIS ingot. The ingot was grown with the chemical formula of $CuInSe_{2.1}$ ($CIS_{2.1}$) using a vertical Bridgman method by Dr. Hadley F. Myers for his PhD study completed at McGill University (Canada) under the supervision of Dr. Clifford H. Champness and Dr. Ishiang Shih. General background information on the vertical Bridgman method can be found in the Chapter 2 of this dissertation. As was reported in Dr. Hadley F. Myers' dissertation [122], $CIS_{2.1}$ ingot was grown with appropriate amounts of high purity Cu, In and Se pellets in a vacuum-sealed (~10^{-7} torr) fused quartz ampoule. Before the Bridgman growth process, the ampoule was heated up to 400 °C and maintained at this temperature for 3 hrs 30 min in a brick furnace to react In and Se in a closed environment. It was reported in the same dissertation that, this pre-reaction procedure was necessary to reduce the risk of an ampoule damage that could occur in the exposed upper-zone of the Bridgman furnace (Fig. 3.11) during the first step of crystal growth due to an increase in the ampoule pressure by the Se vapor. After the pre-reaction was complete, the ampoule was placed into the upper-zone of the Bridgman furnace. The upper-zone temperature was increased to 1100 °C and the ampoule was kept in the upper zone for 24 hrs. During the 24 hr reaction period, the ampoule was taken out of the furnace three times and rocked to have a well mixed melt in the ampoule.

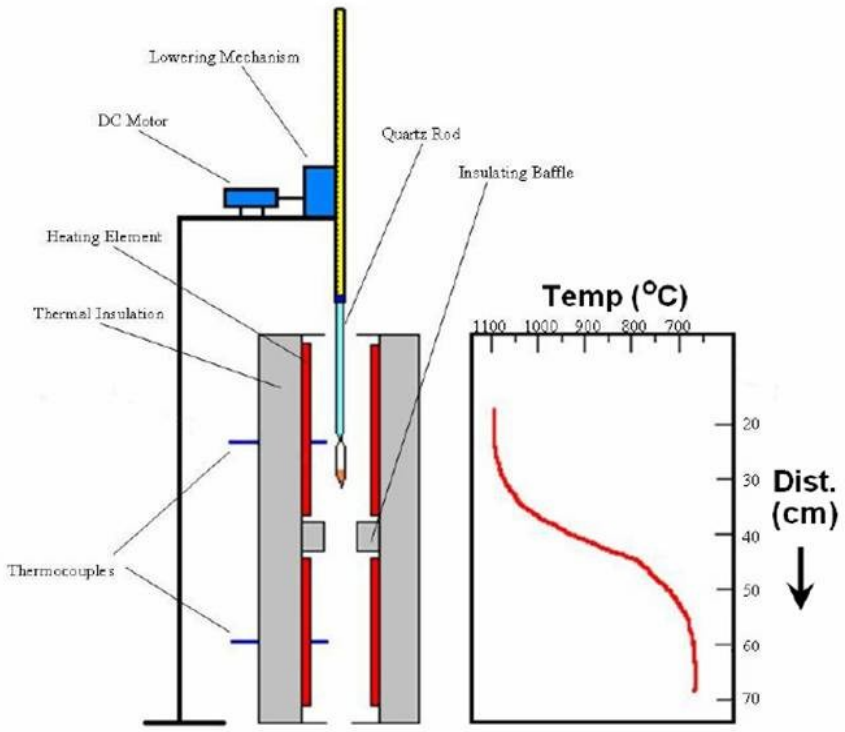

Figure 3.11 Schematic of the Bridgman furnace (left) and its temperature profile (right) used to grow the $CIS_{2.1}$ ingot at McGill University (Canada). The ampoule is shown as it is located at the beginning of the growth process in the upper –zone of the furnace [122].

After 24 hrs, the ampoule was lowered to the lower-zone of the furnace at 700 °C at a rate of 3.34 mm/hr. Once the entire ampoule was in the lower-zone, the temperature was reduced to room temperature in ~44 hrs (cooling rate: 15.71 °C/hr). The ampoule was broken to take out the grown ingot. Hot probe measurement showed that the $CIS_{2.1}$ ingot was *p*-type.

Compositional analysis of the $CIS_{2.1}$ wafer was carried out by energy dispersive X-ray spectroscopy (EDS) (EDAX) in a scanning electron microscope (SEM) (Hitachi, S-3000N) on multiple regions of the as-received wafer at electron-beam energy (E_b) of 10 kV. The wafer (diameter ≈ 11 mm, thickness ≈ 5 mm) was then embedded in epoxy, and it was first ground with 600, 1500, 2500 and 3000 grit sand papers followed by polishing with 5 μm, 1 μm and 0.05 μm alumina suspension successively. The polished wafer was taken out of the epoxy for analyses. Images of the wafer were taken by an optical microscope (Nikon SMZ 1500) coupled

with a digital camera. Compositional analysis, sample polishing and optical microscopy imaging were performed at the University of Texas at Arlington (UTA).

GBs were identified on an inverse pole figure (IPF) map obtained by electron backscatter diffraction (EBSD) measurement. EBSD measurement was performed by an EBSD detector (EDAX Hikari) attached to an SEM (FEI Nova NanoSEM 630) by Dr. Helio R. Moutinho at National Renewable Energy Laboratory (NREL) (USA). Background information on working principles of EBSD and data analysis can be found in Chapter 2 of this dissertation. EBSD data collection was performed with E_b and electron-beam current (I_b) of 15 kV and 1.4 nA, respectively, on a hexagonal grid with 40 μm step size. Sample tilt angle was 70° with respect to the sample plane during the measurement. Orientation Imaging Microscopy (OIM™) software (version 6.1.3) (EDAX) was used for viewing EBSD IPF maps and obtaining GB misorientation angle/axis pairs. The IPF maps were independently obtained and GB misorientation angle/axis pairs were confirmed at UTA using EBSDmcf© (version 6.0) [123] together with TexTools (version 3.3) software (ResMat Corporation, Canada) [124] as well.

Topography and contact potential difference (CPD) measurements of the identified GBs were acquired simultaneously by Kelvin probe force microscopy (KPFM) in an atomic force microscope (AFM) (XE-70, Park Systems) equipped with a lock-in amplifier (SR830, Stanford Research Systems) under ambient conditions at UTA. In addition, simultaneous topography and qualitative surface potential measurements were also performed with the same set-up by electrostatic force microscopy (EFM). Background information on working principles of AFM, KPFM and EFM can be found in the Chapter 2 of this dissertation. A gold coated silicon cantilever (NSC14/Cr-Au, MikroMasch, purchased from Park Systems as mounted on chip carrier) was used for KPFM measurements. To measure the CPD separate from the topography, an alternating current (AC) signal (2.5 V/18 kHz) from the lock-in amplifier was superimposed onto the cantilever which was oscillating at ~160 kHz, close to its resonance frequency, with 20 – 30 nm amplitude. Examined GBs were aligned along the AFM's slow scan

direction and all data were recorded in the AFM's fast scan direction (x) to reduce the effect of a possible thermal drift occurring during the measurement on the data. Scan rate was 0.2 – 0.5 Hz. The KPFM set-up used in this study requires the CPD to be defined as CPD = (ϕ_{tip} – ϕ_{sample})/e, where ϕ_{tip} and ϕ_{sample} are the work functions of the tip and the sample, respectively, and e is the elementary charge. Because the CPD between the tip and sample was measured by applying the nullifying voltage to the tip and the sample was ground. A possible cross-talk between the topography and the KPFM signals was ruled out by confirming that charged regions on the sample reverse their contrast in the EFM images when EFM measurements were performed with positive and negative tip bias voltages. Because, if we consider two measurement points with measured contact potential differences of V_{CPD-1} and V_{CPD-2}, respectively, and furthermore $V_{CPD-1} > V_{CPD-2}$, then positive and negative bias voltages applied to the tip (V_{dc}) will result in $V_{CPD-1} > V_{CPD-2}$ and $V_{CPD-1} < V_{CPD-2}$, respectively, since the measured signal $F_{\omega_{ac}}$ contains the $(V_{dc} - V_{CPD})$ term (Eq. 2.13). Therefore, contrast reversal between these two points occurs by changing the polarity of tip bias voltage. However, the topography signal is not affected by the polarity of the V_{dc}, because the F_{dc} term (Eq. 2.12) contains the $(V_{dc} - V_{CPD})^2$ term [125, 126]. XEI 1.7.1 software (Park Systems) was used for data analysis.

Cathodoluminescence (CL) measurements were performed in an SEM (JEOL 5800) (SEM-CL) equipped with collection optics, spectrograph and a cryogenic InGaAs photodetector array (RoperScientific OMAV 512x1) by Dr. Manuel J. Romero at NREL (USA). Background information on CL and its measurement can be found in the Chapter 2 of this dissertation. E_b and I_b were 15 keV and 1 nA, respectively, and the measurements were performed at 45 K. Data was acquired in spectrum imaging mode, i.e. a CL spectrum was acquired for each pixel of the image in synchronization with the electron beam. CL spectrum acquisition time was 20 ms per pixel. The spectrum imaging software developed at NREL was used to process the data, which allowed extraction of the CL spectrum of any pixel on the CL photon intensity map [127].

3.3 Results and Discussion

Cu/In and (Cu+In)/Se ratios of the $CIS_{2.1}$ wafer (Fig. 3.12) were 0.9 and 1, respectively, according to SEM-EDS. Investigating GBs in copper-poor CIS was important, because device quality chalcopyrite thin films have had a copper-poor composition so far [12].

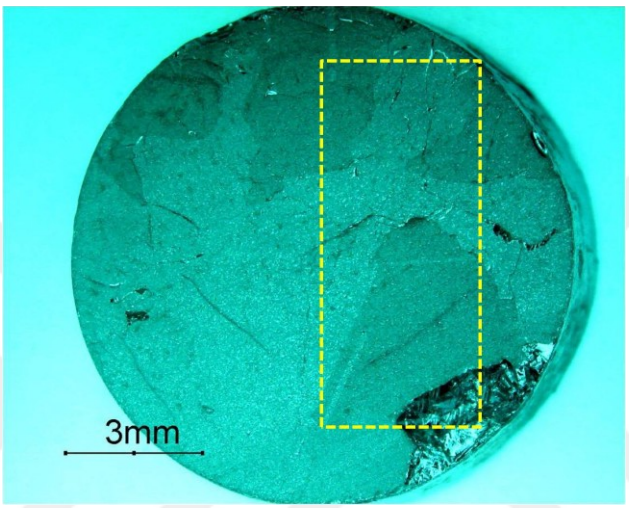

Figure 3.12 Optical microscopy image of the $CIS_{2.1}$ wafer before polishing. The yellow dotted rectangle shows the wafer region studied in this dissertation.

The wafer region studied is indicated by the yellow dotted rectangle in Figure 3.12. EBSD IPF map revealed the GBs existed in this region (Fig. 3.13). Further analysis was focused on GBs between grain (G) 3 and G5 ($GB_{3\&5}$), $GB_{1\&3}$ and $GB_{1\&5}$, because these GBs were identified as Σ3, ~Σ3 and Σ9, i.e. a non-Σ3 GB, according to their misorientation angle/axis pairs (Table 3.1).

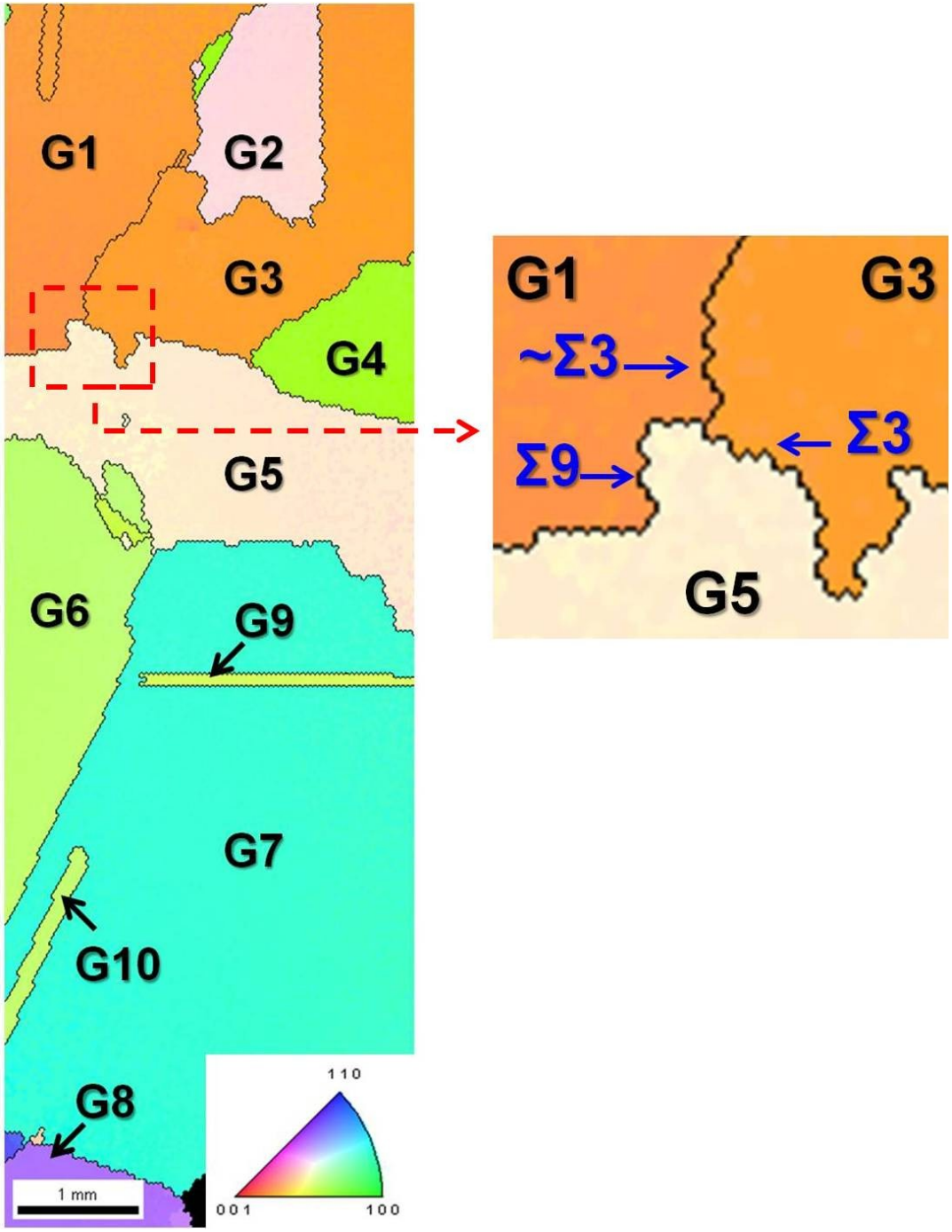

Figure 3.13 Inverse pole figure (IPF) map (normal direction) of the region studied in $CIS_{2.1}$ wafer. Crystallographic orientations are indicated in the color-coded stereographic triangle. The red dotted arrow indicates the close up image of the red dotted rectangle in the IPF map where the investigated grain boundaries (GB) between the grain (G) 1, G3 and G5 are located.

Table 3.1 Misorientation angle/axis pairs of the grain boundaries between the grains indicated in the IPF map of the region studied (Fig. 3). $GB_{1\&2}$, for example, indicates the GB between grain 1 and grain 2 which are the identification numbers of the grains as shown in Figure 3.13.

Grain Boundary (GB)	Misorientation Angle/Axis Pair
$GB_{1\&2}$	65.1 [-23 -8 4]
$GB_{1\&3}$	54.7 [-20 -19 -9]
$GB_{1\&5}$	37.2 [26 3 -12]
$GB_{2\&3}$	29.4 [16 -13 -1]
$GB_{3\&4}$	58.9 [-2 2 -1]
$GB_{3\&5}$	70.7 [1 1 0]
$GB_{4\&5}$	67.0 [-23 -8 4]
$GB_{5\&6}$	36.8 [-20 -1 -11]
$GB_{5\&7}$	78.1 [7 22 4]
$GB_{6\&7}$	59.7 [2 2 -1]
$GB_{7\&8}$	70.3 [21 22 0]
$GB_{7\&9}$	61.3 [-19 -19 10]
$GB_{7\&10}$	60.8 [19 19 -9]

Σ3 GBs in chalcopyrites are represented by 60° <221> and 70.53° <110> (for chalcopyrites with c/a = 2) (Fig. 3.14), whereas Σ9 GBs are represented by 38.94° <201> and 96.38° <210> [87, 128]. Therefore, $GB_{1\&3}$ was characterized as ~Σ3 in this study, because its misorientation angle (54.7°) was 5.3° away from the required value of 60° to be considered as a Σ3 GB, whereas the $GB_{3\&5}$ was characterized as Σ3 with 0.17° tolerance. Studying Σ3 GBs in chalcopyrites are important, because Σ3 GBs are found to be abundant in chalcopyrite materials [87]; hence, understanding their electronic behavior can give clue on the high performance of polycrystalline chalcopyrite solar cells. Abundance of the Σ3 GBs in chalcopyrites is explained by the low stacking fault energy in this material system [88, 128]. Because twin formation is based on stacking faults and twin GBs are characterized as Σ boundaries according to the CSL notation [89]. It should be mentioned here that the twin boundaries in chalcopyrites are not exactly Σ3 because of the tetragonal distortion, i.e. c/a is not exactly 2 due to the different lengths of Cu-Se

and In-Se bonds [87]. In terms of electronic behavior, since Σ3 GBs have a high number of lattice points in coincidence, they are supposed to be electronically harmless to the performance of a solar cell. Because it is expected that a Σ3 GB has less amount of defects [103], i.e. dangling and strained bonds, which would introduce midgap states and make the GB a recombination center. In addition, a Σ3 twin GB can possibly have a hole barrier preventing GB recombination according to the VBO model, if its GB plane is cation terminated (112) [90, 91, 103].

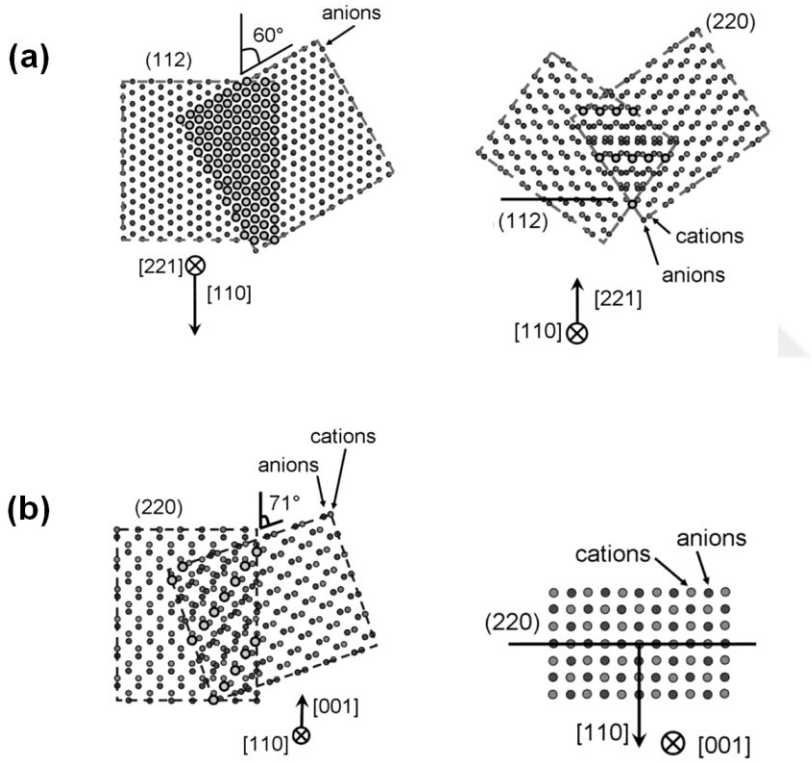

Figure 3.14 Schematic descriptions of two Σ3 grain boundary systems in chalcopyrite materials. Large circles indicate the coincidence lattice sites. (a) *Left:* Two superimposed grains oriented in [221] with 60° misorientation angle (60° <221>). *Right:* The same grains are viewed perpendicular to (112) plane showing that the coincidence site lattice has three times larger (112) interplanar distance than the chalcopyrite lattice has. (b) *Left:* Two superimposed grains oriented in [110] with 71° misorientation angle (70.53° <110>) showing that the coincidence site lattice has three times larger (112) interplanar distance than the chalcopyrite lattice has. *Right:* The same grains are viewed at [001] direction perpendicular to (220) plane showing when a grain rotated around [110] for 71° will have the same periodicity with the original grain [87].

KPFM showed that the Σ3 (Fig. 3.15) and ~Σ3 GBs (Fig. 3.17) were neutral or the existing CPD between these GBs and adjoining grains was less than the resolution limit of our measurements which was estimated to be ~40 mV by considering the noise in the data. The circular and triangular regions in Figures 3.15b and 3.17b were possibly contamination on the surface. When EFM measurements were performed with V_{tip} +1V and -1V (Figs. 3.15c and d, and Figs. 3.17c and d), these regions reversed their contrast indicating that they were charged; however, there was not any indication of their existence in the topography image. Topography and CPD averaged line profiles on the Σ3 (Fig. 3.16) and ~Σ3 GBs (Fig. 3.18) extracted from Figures 3.15 and 3.17, respectively, more clearly showed the absence of any CPD at these GBs. A neutral Σ3 GB was not a surprising outcome and was reported in the literature for both Na-free [103] and Na-containing [121] chalcopyrites. It is expected that the amount of strained and dangling bonds that can create interface states and trap charge is minimal at a Σ3 GB, because a Σ3 GB forms between two grains that have the highest coincidence of lattice points at their interface. Although there was not a CPD at the GB, a clear CPD between the grain surfaces was observed for both Σ3 (Fig. 3.16) and ~Σ3 GBs (Fig. 3.18) in their CPD line profiles. This result might be due to a topography convolution to the CPD signal and/or a CPD created between these two differently oriented grain surfaces [129].

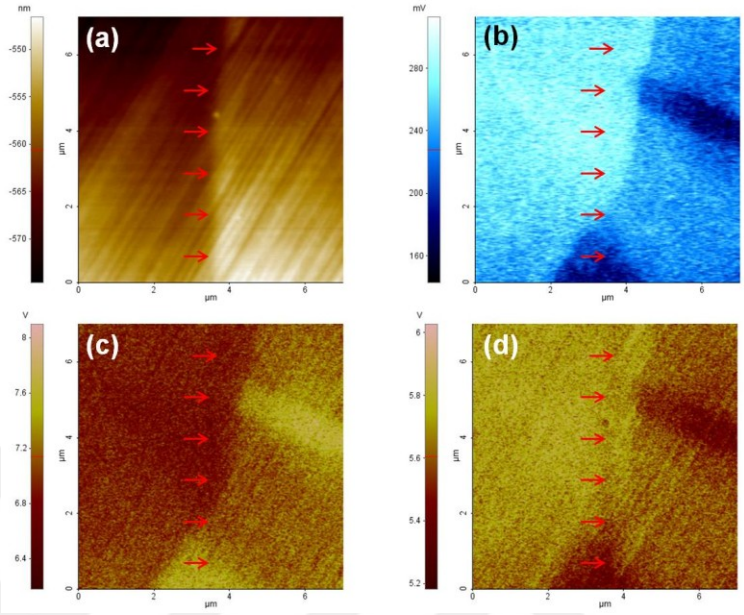

Figure 3.15 Kelvin probe force microscopy (KPFM) and electrostatic force microscopy (EFM) measurements of the Σ3 grain boundary between grains 3 and 5 shown in Figure 3.13. (a) Topography and (b) CPD images measured simultaneously by KPFM. EFM amplitude images measured with applied tip voltage of (c) +1 V and (d) -1 V. The red arrows indicate the location of the GB.

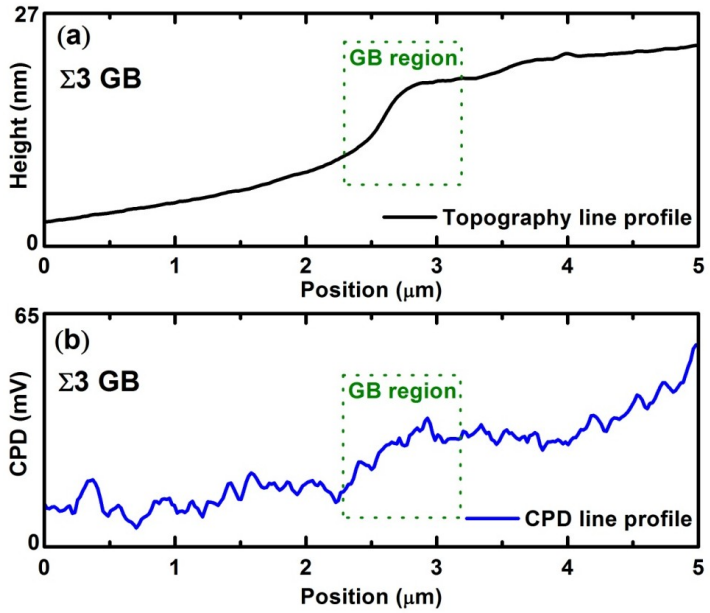

Figure 3.16 (a) Topography and (b) CPD line profiles extracted from the same locations on topography (Fig.3a) and CPD images (Fig. 3b) of the Σ3 grain boundary between grains 3 and 5 shown in Figure 3. Profiles shown are averaged result of 20 consecutive line profiles.

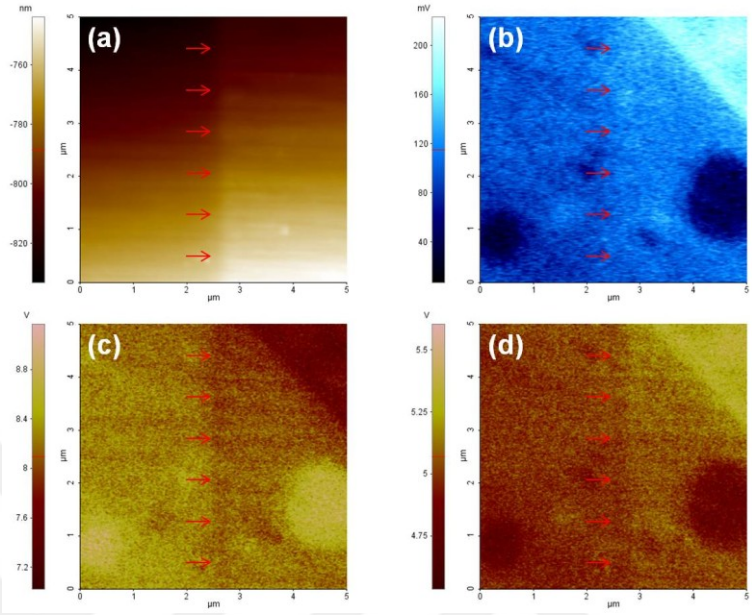

Figure 3.17 Kelvin probe force microscopy (KPFM) and electrostatic force microscopy (EFM) measurements of the ~Σ3 grain boundary between grains 1 and 3 shown in Figure 3.13. (a) Topography and (b) CPD images measured simultaneously by KPFM. EFM amplitude images measured with applied tip voltage of (c) +1 V and (d) -1 V. The red arrows indicate the location of the GB.

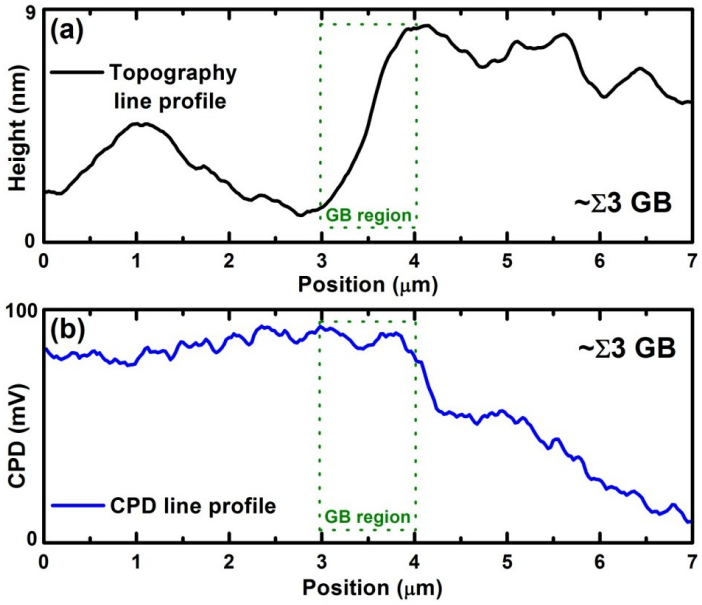

Figure 3.18 (a) Topography and (b) CPD line profiles extracted from the same locations on topography (Fig.3a) and CPD images (Fig. 3b) of the ~Σ3 grain boundary between grains 1 and 3 shown in Figure 3. Profiles shown are averaged result of 20 consecutive line profiles.

Although, according to the KPFM, the Σ3 and ~Σ3 GBs seemed behaving similar regardless of the slight difference in their GB geometry, SEM-CL measurements indicated a clear difference in the recombination activity occurring at these GBs. Σ3 GB was not a recombination center as the CL intensity at the Σ3 GB (Fig. 3.19) was the same as that of the adjoining grains forming it. This was in agreement with its KPFM result which indicated that the Σ3 GB was neutral due to the absence of interface states to trap charge carriers and hence result in increased recombination activity at the Σ3 GB.

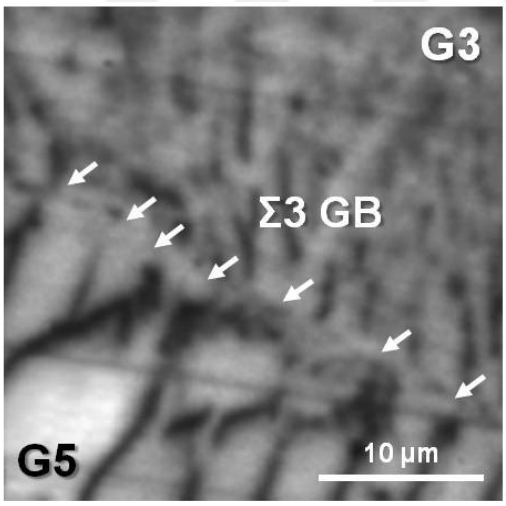

Figure 3.19 CL intensity image of the Σ3 grain boundary (GB) between grains (G) 3 and 5 shown in Figure 3. The arrows indicate the location of the Σ3 GB.

Conversely, ~Σ3 GB was an effective recombination center which was evidenced by a CL intensity reduction at this GB when compared to the CL intensity of the adjoining grains forming it (Fig. 3.20a) although it was neutral according to the KPFM results. CL intensity at the ~Σ3 GB was reduced ~73% and ~45% with respect the CL intensity of G1 and G3, respectively. Clearly, being more than 5° off from an exact Σ3 misorientation angle was sufficient to introduce midgap states at the GB and make it a recombination center.

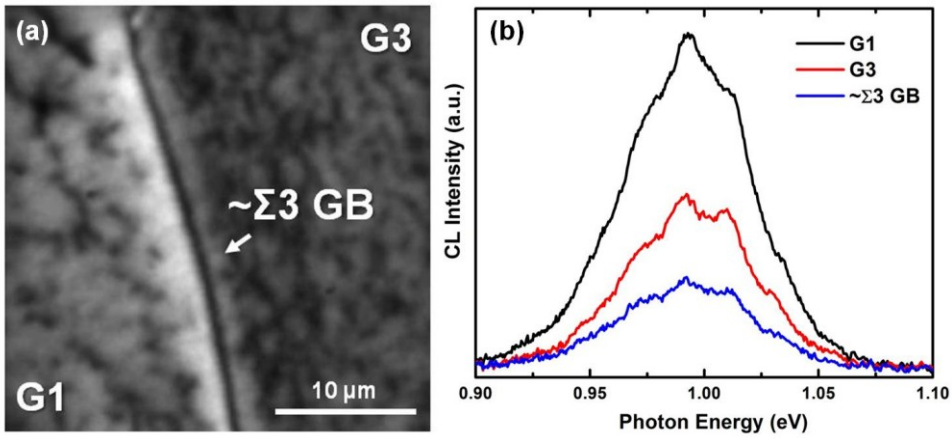

Figure 3.20 SEM-CL measurement results of the ~Σ3 GB located between G1 and G3. (a) CL intensity image. The arrow indicates the ~Σ3 GB. (b) CL spectrum of G1, G3 and ~Σ3 GB.

In addition, the CL spectra of G1, G3 and ~Σ3 GB (Fig. 3.20b) extracted from the CL intensity image indicated that the electronic band structure at the ~Σ3 GB was the same as the grains, since a shift in the energy position of the ~Σ3 GB's CL spectrum was not observed and the shapes of these three CL spectra had the same features but they had different CL intensities due to defects on the grain surfaces and midgap states at the GB.

The electronic behavior of the Σ3 and ~Σ3 GBs can be explained by the classical e-GB model [4-6] which suggests band bending at the GBs due to trapped charge. The Σ3 GB investigated did not have a band bending, because both its KPFM and SEM-CL data indicated that it did not have significant amount of interface states making the GB charged and a recombination center. Therefore, band diagram at the Σ3 GB can be drawn as it is in the adjoining grains forming it (Fig. 3.21). However, there was a band bending at the ~Σ3 GB (Fig. 3.22). Although its KPFM result did not show the band bending at the ~Σ3 GB, its existence was evidenced by the SEM-CL result indicating increased recombination activity due to interface states located at the ~Σ3 GB. The amount of band bending at the ~Σ3 GB was expected to be much less than 40 mV which was the estimated resolution limit of the measurement. However, whether it was an upwards or downwards band bending was not known because of a lack of information on polarity of the charge existed at ~Σ3 GB. If it was positively charged, there was a

downwards band bending causing the electrons drawn to the GB and recombine with the holes there, and vice versa. Moreover, the band structure at the ~Σ3 GB was possibly the same as the adjoining grains forming it but it included interface states, because the SEM-CL spectra of G1, G3 and ~Σ3 GB had the same features but different CL intensities without any relative energy shift with respect to the energy position of each other's CL spectrum. The electronic behavior of Σ3 GB can also be viewed in terms of the EB-GB model [10] which was detailed in the introduction of this chapter. The EB-GB model predicts that GBs in Na-free CIS are not recombination centers, because a significant GB expansion prevents dangling bonds to create deep levels at the GB. However, the electronic behavior of the ~Σ3 GB was not in agreement with the EB-GB model because it has recombination centers.

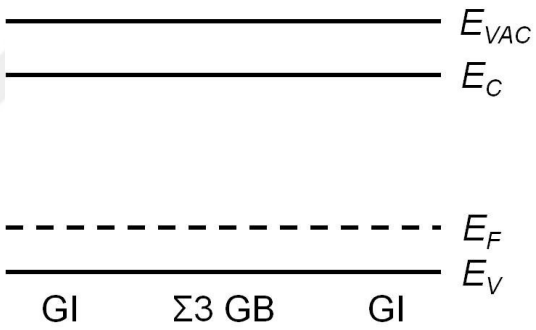

Figure 3.21 Schematic energy band diagram of the Σ3 GB. E_{VAC}: Energy level of vacuum. E_C: Energy level of conduction band minimum. E_F: Energy level of Fermi level. E_V: Energy level of valence band maximum. GI: Grain interior.

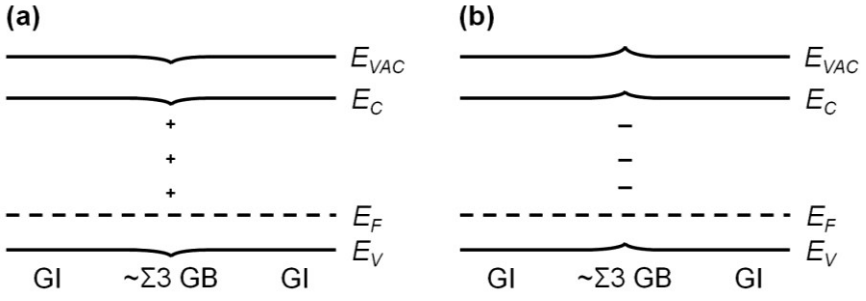

Figure 3. 22 Schematic energy band diagram of the ~Σ3 GB (a) when there is a downwards band bending at the GB and (b) when there is an upwards band bending at the GB. E_{VAC}: Energy level of vacuum. E_C: Energy level of conduction band minimum. E_F: Energy level of Fermi level. E_V: Energy level of valence band maximum. GI: Grain interior. Plus and minus signs indicates the positive and negative trapped charge at the GB.

VBO model [90, 91], detailed in the introduction of this chapter, predicts a hole barrier located at the GB, if the GB plane is a cation terminated {112}. The hole barrier existing due to an offset at the valence band repels holes and creates a recombination free region for electrons at the GB. The Σ3 and ~Σ3 GBs investigated were supposed to have a {110} and a {112} GB planes (Fig. 3.14), respectively. However, we cannot interpret our results according to the VBO model. Because the Σ3 GB examined was supposed to have a {110} GB plane. On the other hand, although the ~Σ3 GB had a {112} GB plane, whether it was a cation or anion terminated {112} plane is not known. Moreover, its misorientation angle deviation from the exact misorientation angle of 60° made the ~Σ3 GB irrelevant for the VBO model. Nonetheless, if we were to draw a hypothetical picture and assume that the GB plane of the ~Σ3 GB was a cation terminated {112} plane and with a further assumption its misorientation angle deviation was not disturbing the VBO model, then we would see a shift in its CL spectrum with respect to the CL spectra of G1 and G3 because the bandgap at the GB increases due to the VBO located at the GB. And, it should be noted that a red shift of CL at the GBs in CIGS was reported in the literature [130], and it was claimed that the Cu vacancies form a band at the GB due to the increase in the concentration of Cu vacancies.

As the GB geometry was further deviated from the geometry of the Σ3 GB significant differences in topography and potential results were observed. Unlike the Σ3 and ~ Σ3 GBs, the Σ9 GB had an open topography (Fig. 3.23a). This result was in agreement with the expected high GB energy (γ_{gb}) associated with the Σ9 GB. Because when two grain surfaces with the surface energy (γ_s) are brought together to form a GB, the GB energy will be $2\gamma_s$ reduced by the binding energy (*B*) gained due to new bond formation at the GB,

$$\gamma_{gb} = 2\gamma_s - B. \tag{3.1}$$

Assuming that γ_s is the same for Σ3 and Σ9 GBs, *B* of a Σ9 GB is expected to be less than that of the Σ3 GB resulting in a higher γ_{gb} in the Σ9 GB than the Σ3 GB. Because as the Σ parameter increases the lattice sites in coincidence decreases, hence bonding at the GB [131-133].

Moreover, the Σ9 GB was positively charged (Figs. 3.23b) and the existing charge was confirmed by contrast reversal at the charged GB by EFM measurements performed with V_{tip} at +1V and -1V (Figs. 3.23c and d). A downwards band bending of ~100 mV located at the Σ9 GB was measured by the topography and CPD averaged line profiles (Fig. 3.24) which was in agreement with a previously reported measurement on a Σ9 GB in a Na-free CGS (Fig. 3.6) [104]. This result was not surprising, because high density of GB states in the bandgap was expected at the Σ9 GB due to the increased amount of defects compared to a Σ3 GB.

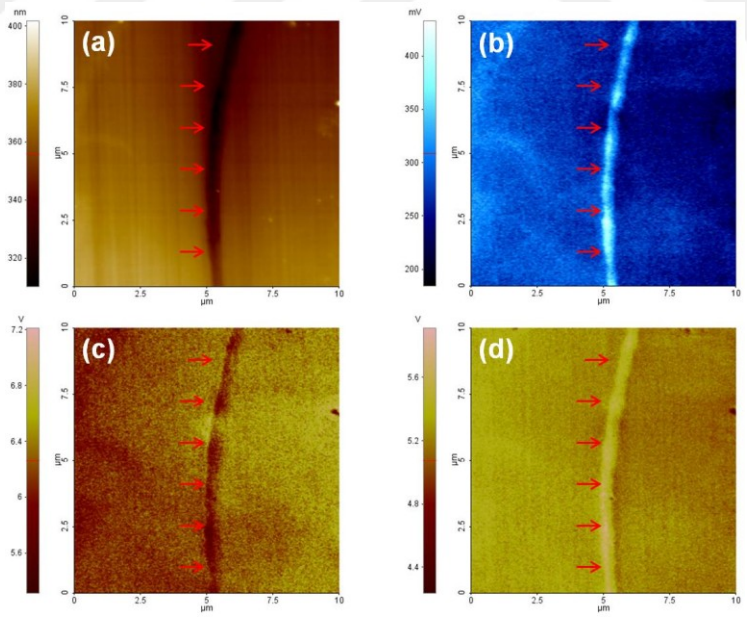

Figure 3.23 Kelvin probe force microscopy (KPFM) and electrostatic force microscopy (EFM) measurements of the Σ9 grain boundary between grains 1 and 5 shown in Figure 3.13. (a) Topography and (b) CPD images measured simultaneously by KPFM. EFM amplitude images measured with applied tip voltage of (c) +1 V and (d) -1 V. The red arrows indicate the location of the GB.

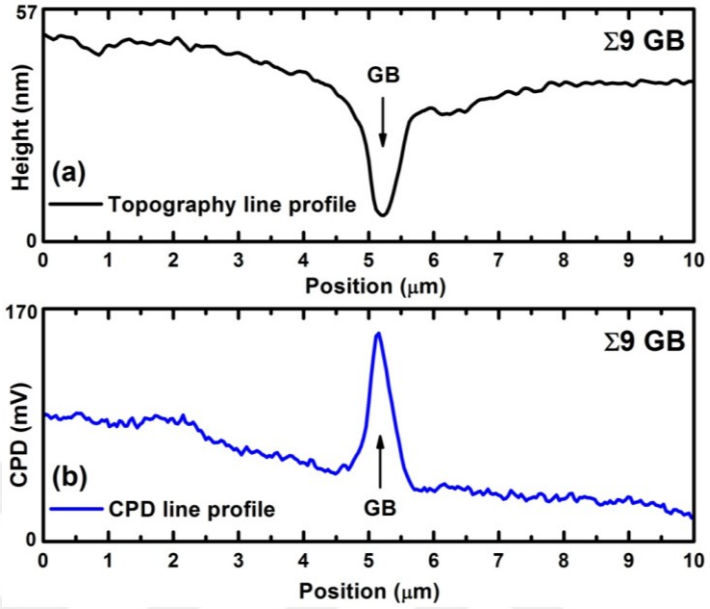

Figure 3.24. (a) Topography and (b) CPD line profiles extracted from the same locations on topography (Fig.3a) and CPD images (Fig. 3b) of the Σ9 grain boundary between grains 1 and 5 shown in Figure 3. Profiles shown are averaged result of 20 consecutive line profiles.

SEM-CL indicated the high recombination activity occurring at the Σ9 GB (Fig. 3.25). The CL intensity was ~93% lower at Σ9* and ~53% lower at Σ9 with respect to the G5. The local deviation in the CL intensity might be a topographical artifact on the CL intensity. It can also be speculated that the local CL intensity variation is due to a local increase/decrease in the density of dangling and strained bonds which might stem from possible defects at the GB plane, such as voids. However, further investigation is necessary to find a comprehensive reason for the local CL intensity variation along the GB.

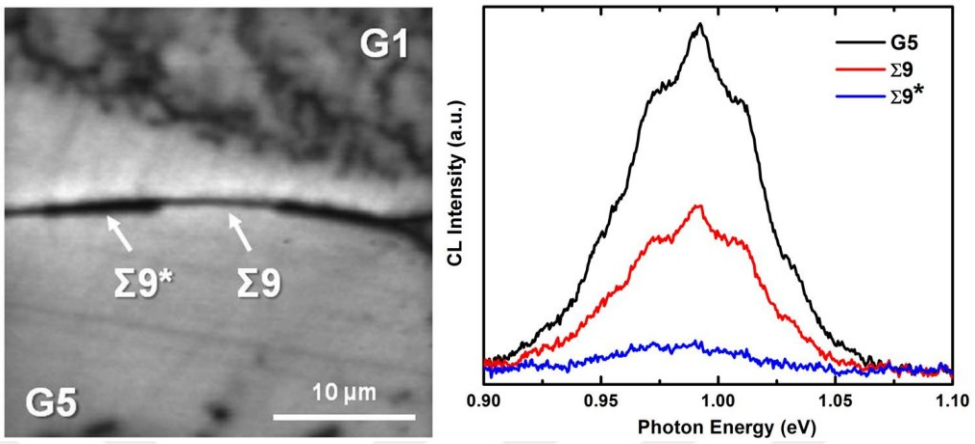

Figure 3.25 SEM-CL measurement results of the Σ9 GB located between G1 and G5. (a) CL intensity image. The arrows indicate two regions, Σ9 and Σ9*, located along the same Σ9 GB. (b) CL spectrum of G5, region Σ9 and region Σ9*.

The electronic behavior of the Σ9 GB can be explained by the eGB model [4-6], i.e. band bending at the GB due to the trapped charge at the interface states introduced by dangling bonds (Fig. 3.26).

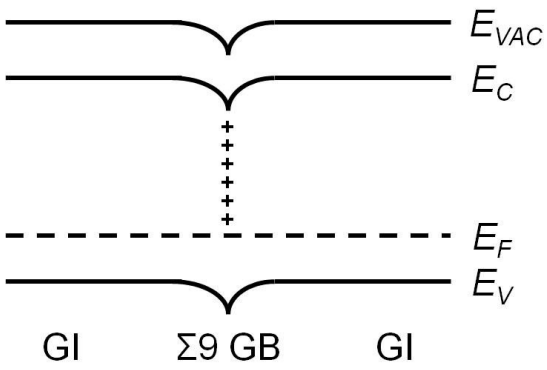

Figure 3.26 Schematic energy band diagram of the Σ9 GB. E_{VAC}: Energy level of vacuum. E_C: Energy level of conduction band minimum. E_F: Energy level of Fermi level. E_V: Energy level of valence band maximum. GI: Grain interior. Plus signs indicate the positive trapped charge at the GB.

According to our SEM-CL measurement, the positively charged Σ9 GB was an effective recombination center and it should be detrimental to the performance of a solar cell. In addition, because the CIS ingot used in this study was grown without intentional Na addition, the positive charge located at the GB is not expected to be related to existence of Na at the GB as was

claimed by EB-GB model [10]. As was mentioned above, EB-GB model predicts that GBs in chalcopyrites do not have deep levels, hence they are neutral; however, it was further claimed that the GBs become positively charged when Na is present, since it was found that Na prefers interstitial sites and interstitial Na is a shallow donor.

Consequently, by considering the results presented on all the GBs, i.e. ~Σ3, Σ3 and Σ9, investigated in this study, it can be claimed that the electronic behavior of GBs in CIS without intentional Na addition is governed by the crystallographic properties of the GBs. Because while the Σ3 GB was charge neutral and was not a recombination center due to the highly matched lattice points of the neighboring grains at the GB plane, once the GB misorientation starts to deviate from a perfect Σ3, the GB becomes charged and acts as a recombination center due to the interface states introduced by the dangling and strained bonds.

3.4 Conclusions

Σ3, ~Σ3 and Σ9 GBs in a Bridgman-grown multicrystalline Na-free $CIS_{2.1}$ wafer were identified by EBSD and their electronic behavior was investigated by KPFM and SEM-CL. It was shown that the electronic behavior of these GBs was strongly related to the geometrical fit at their GB plane. The Σ3 GB was neutral, hence did not have a band bending, and was not a recombination center. This was thought to be due to the high coincidence of the lattice points at the Σ3 GB; hence fewer amount of dangling and strained bonds it had which could introduce interface states. As a GB began to deviate from the Σ3 geometry, increase in the recombination activity was observed. The misorientation angle of the ~Σ3 GB was more than 5° off to be considered as a perfect Σ3. Although this amount of deviation was not sufficient to make the ~Σ3 GB charged according to the KPFM measurement, it behaved as a recombination center indicating the increased amount of interface states with the reduced amount of coincident lattice sites when compared to the Σ3. However, it could not be determined whether the band bending at the ~Σ3 GB was downwards or upwards, since the existing CPD and charge were below the resolution limit of KPFM and EFM measurements, respectively. And finally, the Σ9 GB had ~100

mV downwards band bending with a high recombination activity which was understandable due to the relatively reduced number of coincident lattice points at his GB. These results could be explained with the classical eGB model which simply relates the interface states and band bending at a GB. Moreover, the result presented indicated that existence of Na was not required to make a GB charged which was contrary to the prediction of the EB-GB model.

3.5 Future Work

The results presented in this chapter were on the electronic properties of GBs in Na-free CIS. To have an understanding of effect of sodium on the electronic properties of GBs the same measurements performed on the Na-free $CIS_{2.1}$ need to be performed on Σ3 and non-Σ3 GBs of a Na-containing CIS wafers. Two Na-containing CIS wafers ($CIS_{2.05}$ + 0.1% Na (CIS01Na) and $CIS_{2.05}$ + 9% Na (CIS9Na)) grown at McGill University have been received at UTA. After their surface preparation was completed, they were sent to NREL for EBSD analysis to identify the GBs on the wafers. EBSD analysis of the CIS01Na wafer has been completed so far and GBs were identified on its IPF map (Fig. 3.26). The analyses on the wafer will continue as explained above.

Compositional measurements of the GBs studied in both the Na-free $CIS_{2.1}$ wafer and the wafers grown with Na need to be performed. While tools such as TEM or APT provides a reliable local compositional information, relatively non-destructive tools, such as scanning Auger spectroscopy can be used and might be preferable to continue the analysis of the same GBs with different techniques after the compositional information is obtained.

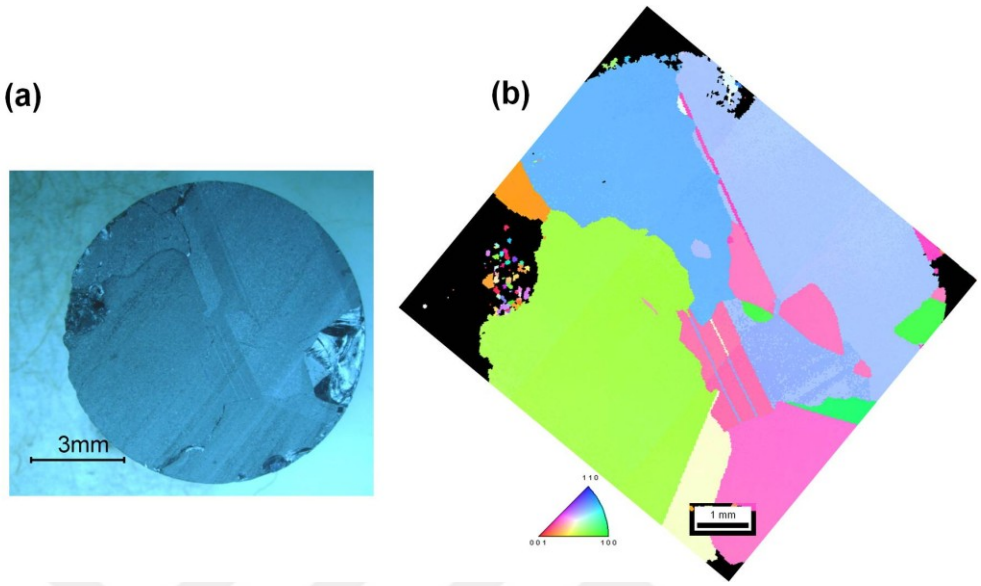

Figure 3.27 Bridgman-grown multicrystalline $CuInSe_{2.05}$ (CIS) wafer grown with 0.1% Na addition. (a) Optical microscopy image of the unpolished wafer. (b) Electron backscatter diffraction inverse pole figure map.

Temperature (T) – dependent I – V measurements over the investigated GBs will be helpful as a complementary data to the KPFM results and also for investigating whether any band bending and/or band offset exist at a GB. For instance, a T-dependent I – V measurement over the Σ9 GB investigated can be used to validate the amount of band bending at this GB measured by KPFM. In addition, a possible valence band offset at a GB with {112} GB plane can be measured by T-dependent I – V measurement because the band offset cannot be measured by KPFM. Also, SEM-CL showed that the ~Σ3 GB was a recombination center; however, KPFM did not detect any CPD at the GB. Therefore, T-dependent I – V measurements can help to obtain the amount of bend bending at this GB.

A last item to be included in the future work list is calculation of the misorientation angle/axis pairs and their symmetrically equivalent misorientations of CSL boundaries in chalcopyrites. Although we were able to obtain the misorientation angle/axis pairs of Σ3 and Σ9 GBs from the literature for this study, a full list of the misorientation angle/axis pairs of CSL boundaries is necessary to extend the study. In fact, a CSL analysis can be performed by EBSD

analysis software. However, as was mentioned in the Chapter 1 of this dissertation, chalcopyrite lattice shows tetragonal distortion, i.e. c/a ratio of the tetragonal chalcopyrite lattice is not exactly 2 due to the different lengths of Cu-Se and In-Se bonds. Consequently, there is a risk of having misindexed EBSD patterns which can cause a misorientation angle assignment with less clarity yielding to a misguiding CSL analysis [87].

CHAPTER 4

CHALCOPYRITE SOLAR CELLS PREPARED BY USING SELENOAMIDE AS SELENIUM SOURCE

$CuInSe_2$ (CIS) and $Cu(In,Ga)Se_2$ (CIGS) thin films were prepared by selenizing Cu-In and In-CuGa metal bilayer thin films with selenoamide in a tube furnace at atmospheric pressure for solar cell fabrication. Chalcogen amides can allow safe transportation and handling of chalcogen sources that can produce chalcogen hydrides at reasonably low temperature. Selenoamide used in this study is stable at room temperature (RT) and decomposes into H_2Se at below 150 °C. It was seen that In segregated towards the bottom of the CIS thin films which was reasoned due to liquid phase In formation and CIS formation reaction. In homogeneity in CIS thin films was realized by carrying out post-selenization annealing at 500 °C for various time periods, which reduced the Cu/In ratio from 1.56 to 0.9. On the other hand, Ga accumulation to the bottom of the CIGS films was observed after selenization which created a bandgap profile in the CIGS absorber, which is beneficial for collection of the minority carriers from the Mo/CIGS interface before they recombine. Post-selenization annealing applied to CIGS thin films favored further intermixing between In and Ga, while the bandgap profile still existed. The first batch of cells fabricated with soda-lime glass (SLG)/Mo/CIS/CdS/ZnO/ZnO:Ga/Al structure exhibited power conversion efficiencies up to 1.6% without any optimization.

A manuscript on the study presented in this chapter is submitted to *Progress in Photovoltaics: Research and Applications*, and a part of the results presented in this chapter was also appeared in the following:

- M. E. Erkan, C.-Y. Lee, S. D. Wu, J.-Y. Lim, D. Lim, K. Kim, and M. H.-C. Jin, "*$CuInSe_2$ solar cells prepared by using seleno-amide as selenium source,*" in

37th IEEE Photovoltaic Specialists Conference, Seattle, WA, 19-24 June 2011, pp. 354-358.

Background information on fabrication of chalcopyrite solar cells and solar cell parameters can be found in the Chapter 1 of this dissertation.

4.1 Introduction

Chalcopyrite $Cu(In,Ga)(Se,S)_2$ material system has been extensively investigated for solar cell applications since its parent material CIS was first synthesized in 1953 [12, 134]. Their adjustable direct band gap and high absorption coefficient make the chalcopyrites ideal absorber materials for thin film solar cells [135], and power conversion efficiencies of ~15% and ~20% have been achieved for thin film CIS [136] and CIGS [1, 2] solar cells in the laboratory, respectively. Although up to 14% power conversion efficiencies have been demonstrated with non-vacuum processed CIGS absorbers [137], higher efficiencies have been obtained by using vacuum-based thin film deposition methods. Typical vacuum-based processes are performed by either co-evaporation of the constituent elements in the vacuum chamber [1, 2, 138] or by selenizing predeposited metal layers at a temperature up to 600 °C [139-146]. For the selenization process, Se can be provided either as a thin layer deposited on top of the metal layers [139, 140] or as a gas-phase precursor such as a vapor of elemental Se [141, 142], H_2Se gas [143, 144], and a vapor of diethylselenide [145, 146]. When H_2Se is used, the endothermic dissociation of H_2Se results in H_2 and polymeric Se_x species, and both H_2Se and Se_x can react with the predeposited metal layers to form chalcopyrite compound [147]. Selenization by H_2Se has the advantage of reducing the consumption of Se compared to the amount of Se needed during a co-evaporation process and removing the excess oxygen by hydrogen during chalcopyrite growth providing an option for an atmospheric pressure process [12, 148, 149, 149]. However, high toxicity and the air reactivity of H_2Se create issues in its mass production, transport and handling [12, 145, 150]. As a safer alternative to direct use of H_2Se, selenoamide ($RC(=Se)NR_2$) can be synthesized and used as a Se-containing precursor

which can liberate H_2Se upon its thermal decomposition, which only occurs during the selenization process. Selenoamide is a solid material at RT and expected to be safer than H_2Se under typical handling and storage conditions. A family of selenoamides has been used as precursors for the synthesis of Se-containing heterocyclic compounds which draw attention due to their bioactivity and pharmacological activity. Reaction of nitrile with a selenating reagent, such as H_2Se or NaSeH, is one of the methods commonly used to synthesize selenoamides [151-153]. In a similar context to the selenoamide, chalcogen amides, in general, can be used in various thin-film chalcogenization processes. For example, H_2S used for sulfurization reaction and for band gap grading of the already selenized absorber is a hazardous gas with similar handling issues as H_2Se [12, 148], and the authors have successfully sulfurized stacked Cu-In metal thin films into $CuInS_2$ thin films using thioacetamide as an alternative to H_2S [154]. Although telluroamide is known to be relatively instable in air and hence rare [155], it is an intriguing thought to utilize the full series of chalcogen amides including thio-, seleno-, and telluroamide in synthesizing chalcopyrite compounds with different bandgaps for fabricating multijunction devices.

In this study, phenylselenocarboxamide was synthesized and used to selenize stacked Cu-In and In-CuGa metal thin films into CIS and CIGS thin films, respectively, in an atmospheric pressure tube furnace. The thermogravimetric analysis of phenylselenocarboxamide from a previous study indicated that it decomposes below 150 °C liberating H_2Se [13] (Fig. 4.1). Vertical compositional inhomogeneity was observed after selenization at 400 °C in both CIS and CIGS thin films, and the effect of post-selenization annealing on In and Ga re-distribution, respectively, in CIS and CIGS thin films was also investigated. Homogenous In distribution and larger grain size in CIS thin films, and improved intermixing between In and Ga in CIGS thin films were obtained by the post-selenization annealing at 500 °C. Finally, working CIS solar cells were fabricated with CIS absorbers prepared by using phenylselenocarboxamide.

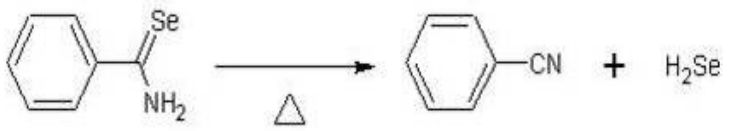

Figure 4.1 Thermal decomposition of phenylselenocarboxamide.

4.2 Experimental Details

Selenoamide preparation: Phenylselenocarboxamide was synthesized by a reaction between arylnitriles and NaSeH according to a previously published study [152] by Mr. Chun-Young Lee at Dr. Kyungkon Kim's laboratory at Korea Institute of Science and Technology (Republic of Korea). Phenylselenocarboxamide at the end of its synthesis appeared as a yellow color solid compound at RT and it was stored under vacuum until its use for the selenization process. Standard laboratory protective clothes, i.e. coat, gloves, and dust mask, were always used for unknown hazards while handling. Although spontaneous oxidation of phenylselenocarboxamide under air was possible and can be recognized by its color change from yellow to green, the oxidation rate seemed very slow at RT and its handling before the selenization process did not require an inert atmosphere. The full chemical analysis on its oxidation process is still necessary, if the extensive use of phenylselenocarboxamide is intended and the authors recommend handling the precursor under a fume hood.

Cu-In bilayer deposition: First, 0.8-0.9 μm thick Mo back contact layer was deposited on clean 1"×1" SLG (microscope slide from Fisher) substrates by a home-built RF sputtering system. Base pressure was 1.2×10^{-5} torr and working pressure was maintained at 10 mtorr during Mo deposition. An NRC thermal evaporator was used for the Cu and In sequential deposition to prepare 1.4-1.5 μm thick Cu-In bilayers with a target Cu/In ratio of 0.9 on SLG/Mo substrates. Cu and In (both 4N pellets from Kurt J. Lesker) were evaporated from tungsten boats (K. J. Lesker) at a rate of 1-2 Å/s which was controlled by a quartz crystal monitor, and the base pressure was 5×10^{-6} torr before the evaporation was started. Depositions were made without intentional substrate heating.

In-CuGa bilayer deposition: Mo, In and CuGa layers were sequentially deposited on 1"x1" SLG substrates by a sputtering system (DMS CO., Republic of Korea) without breaking the vacuum. The base pressure was ~10^{-7} torr and the working pressure was maintained at ~10 mtorr during the deposition of all layers. Thickness of Mo layer and In-CuGa bilayer was 0.8-0.9 μm each. A CuGa alloy target with Cu/Ga ratio of 3.6 was used for CuGa layer deposition. Targeted Cu/III and Ga/III ratio of the bilayer was ~1 and ~0.28, respectively, since optimum composition of CIGS absorbers yielding high efficiency solar cells has been Cu-poor with Ga/III ratio of ~0.3 so far [1, 2, 106, 138].

Selenization process: The bilayers were selenized in a quartz tube furnace which comprised the substrate zone (SubsZ) and the selenium zone (SeZ) heated by a coil furnace (Zircar Ceramics, Inc.) and a heating tape, respectively (Fig. 4.2). After the bilayer was placed into the tube furnace, ~0.3 g phenylselenocarboxamide was weighed under ambient conditions and placed into the SeZ in an alumina crucible. Flange of the tube furnace was then placed and it was purged with ultra-high purity Ar flowing at 300 sccm for at least 15 min, before the furnace temperature was raised.

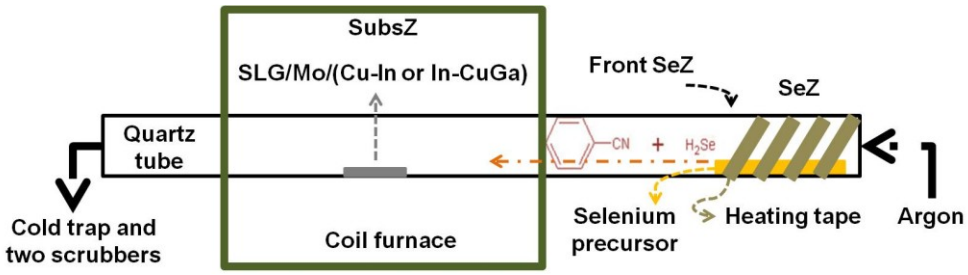

Figure 4.2 Schematic of the selenization set-up used in this study.

Temperature of the SubsZ and the SeZ was controlled independently, and while the SubsZ temperature was measured at the middle of the coil furnace where the bilayer was located, the SeZ temperature was measured at the front of the SeZ which is the closest side of the SeZ to the SubsZ. Because the SeZ temperature was slightly affected when the SubsZ was heated, distance between the two zones was maintained such that the temperature of the SeZ

stayed under the decomposition temperature of phenylselenocarboxamide before the selenization step was started by raising the SeZ temperature. Ar was kept flowing at the same rate of 300 sccm throughout the process including the substrate cooling period. The tube furnace was placed under a fume hood and its outlet was connected to, first, a cold trap and then to two scrubbers containing an aqueous solution of 3M NaOH.

Selenization process (Fig. 4.3) was started with an isothermal pre-selenization annealing (PA) at 400 °C for 30 min (ramping rate: 20-30 °C/min) to homogenize the bilayer. At the end of the PA step, temperature of the SeZ usually reached 65-70 °C without intentional heating. Once the PA was complete, the temperature of the SeZ was raised up to ~145 °C (ramping rate: ~10 °C/min) supplying H_2Se to the bilayer in the SubsZ at 400 °C for 30 min (PSe). Since there was a temperature gradient along the SeZ due to the unintentional heating from the SubsZ, the temperature of the SeZ was increased by 10 °C in every 6-7 min up to 175 °C during the PSe to utilize the entire selenium precursor placed in the crucible. The PSe was finally followed by four different processes (P0-P3). In P0, the substrate was naturally cooled down to RT after the PSe.

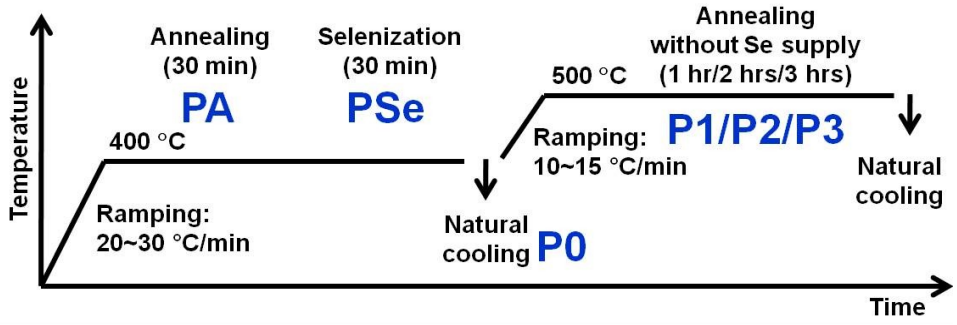

Figure 4.3 Temperature profiles of the processes used.

In the other three processes, SubsZ temperature was increased to 500 °C (ramping rate: 10-15 °C/min) right after the PSe for a post-selenization annealing without the supply of Se. Post-selenization annealing was performed for 1 hr (P1), 2 hrs (P2) or 3 hrs (P3), and then the

substrate was naturally cooled down to RT. While CIS thin films were prepared by all processes shown in Figure 4.3, only P0 and P3 processes were used for CIGS thin film preparation.

Solar cell fabrication: An 80 nm CdS buffer layer and a 50 nm ZnO/500 nm ZnO:Ga window layer were deposited on CIS and CIGS absorbers by chemical bath deposition and RF sputtering, respectively. Front contact was 1 μm thick Al deposited by electron beam evaporation. Device isolation was done by mechanical scribing. Resulting structure of the solar cells was SLG/Mo/(CIS or CIGS)/CdS/ZnO/ZnO:Ga/Al, and the output characteristics were characterized under AM1.5 using a solar simulator. Solar cells were fabricated by Mr. Jong-Youb Lim at Dr. Donggun Lim's laboratory at Chungju National University (CNU) (Republic of Korea) and their characterization was performed at both CNU and the University of Texas at Arlington.

Thin film characterization: Thickness of the deposited films was measured by a surface profiler (Tencor P-10). X-ray diffraction (XRD) was used for bulk (Siemens D500) and depth-profiled (Bruker D8) phase identification. Morphological and compositional analyses of the samples were performed by a scanning electron microscope (SEM) (Hitachi S-3000N) (accelerating voltage: 20-25 kV) equipped with an energy dispersive X-ray spectroscope (EDS) (EDAX).

4.3 Results and Discussion

CIS thin films and solar cells: According to EDS, Cu/In ratios of the as-deposited bilayers prepared under the identical evaporation condition were 0.6-0.7, which was lower than the targeted ratio of 0.9. The higher concentration of In than expectation was concluded to be an artifact coming from the sequence of the bilayer stack in which In was the top layer where EDS had higher sensitivity. The analysis of EDS data was further complicated by the island morphology of the bilayers where higher concentration of In was detected in islands (Cu/In: ~0.5 according to EDS) than terrains (Cu/In: ~1.8 according to EDS) those separate the islands (Fig. 4.4). The In-rich island morphology of the as-deposited Cu-In bilayers was reported in previous

studies where In was deposited onto a Cu layer by evaporation without intentional substrate heating [150, 156, 157].

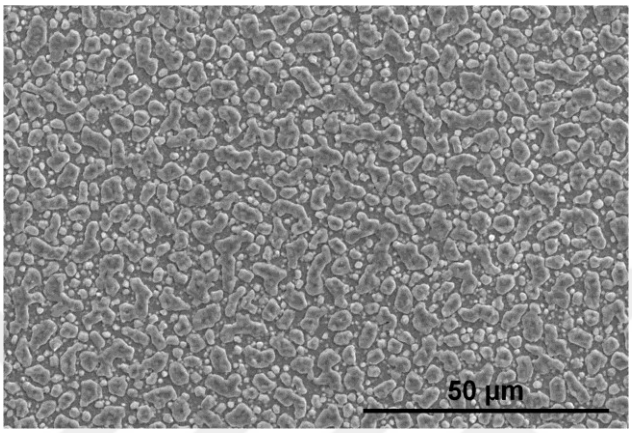

Figure 4.4 SEM image of as-deposited Cu-In bilayer.

Dramatic change in the Cu/In ratio occurred once the bilayer underwent the subsequent steps (Fig. 4.5). The Cu/In ratio increased from 0.69 to 1.56 after selenization at 400 °C (P0) and the ratio continuously decreased once the samples were subject to post-selenization annealing at 500 °C for 1-3 hours (P1-P3), eventually approaching the targeted Cu/In ratio of 0.9. Moreover, the substantial change in the Cu/In ratio seen in P0 required the presence of Se, because the bilayers underwent only PA for up to 1 hr followed by natural cooling had relatively insignificant change in their respective Cu/In ratio. Point EDS measurements performed at the cross-sections of P0 and P3 samples also indicated that high concentration of In is at the bottom of the film (P0) and it was homogenized by the post-selenization annealing at 500 °C (P3) (Fig. 4.6). EDS data further showed that (Cu+In)/Se ratios of all the CIS films were between 0.9-1 regardless of the processes they underwent.

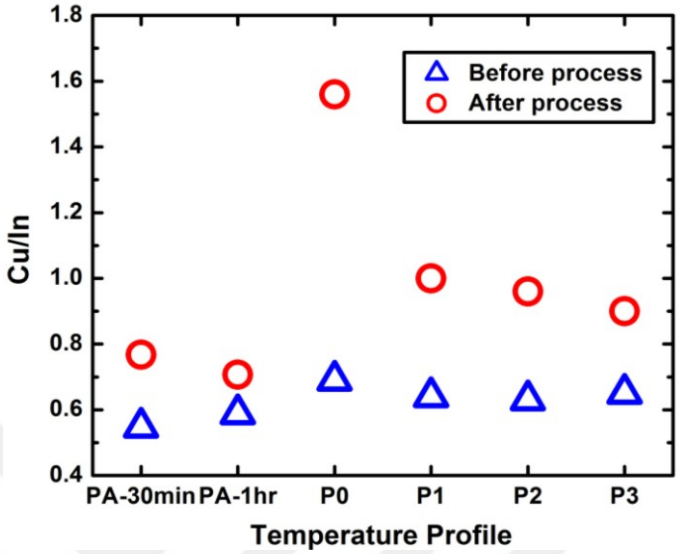

Figure 4.5 Cu/In ratio of the samples processed by the temperature profiles used in this study as determined by EDS. While P0 sample was not annealed after selenization, P1, P2 and P3 samples were annealed at 500 °C after selenization for 1hr (P1), 2 hrs (P2), and 3 hrs (P3). PA-30 min and PA-1hr are the bilayers annealed at 400 °C for 30 min and 1 hr respectively followed by natural cooling without selenization.

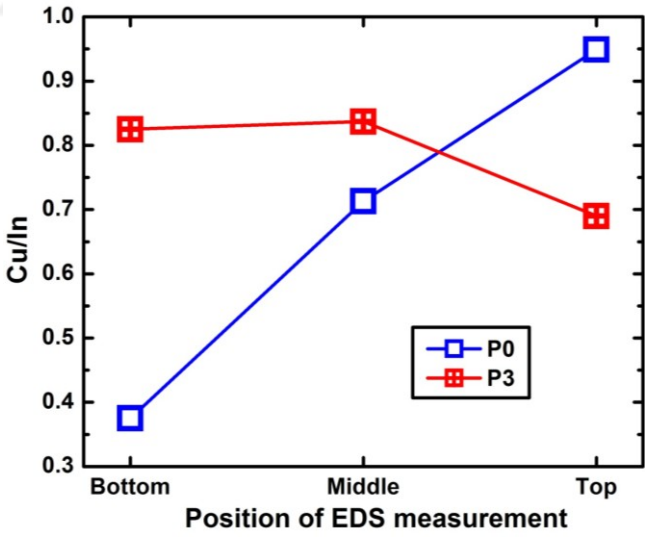

Figure 4.6 Cu/In ratios at the bottom, middle and top regions of the cross-sections of the CIS samples selenized at 400 °C (P0), and annealed at 500 °C for 3 hrs after selenization (P3) as determined by point EDS measurements.

The slight increase in the Cu/In ratio during PA can be explained by the liquid-phase In diffusion towards bottom of the film. In fact, for the composition and temperature range

investigated in this study (Fig. 4.7), Cu-In phase transformations are accompanied by release of liquid In which can diffuse into the underlying Cu-rich layer and continue residing at the bottom of the film, increasing the Cu/In ratio close to the film surface [158, 159]. It was also necessary to understand the selenization mechanism to explain the further increase in the Cu/In ratio during the PSe step and the XRD results presented below gave more insight.

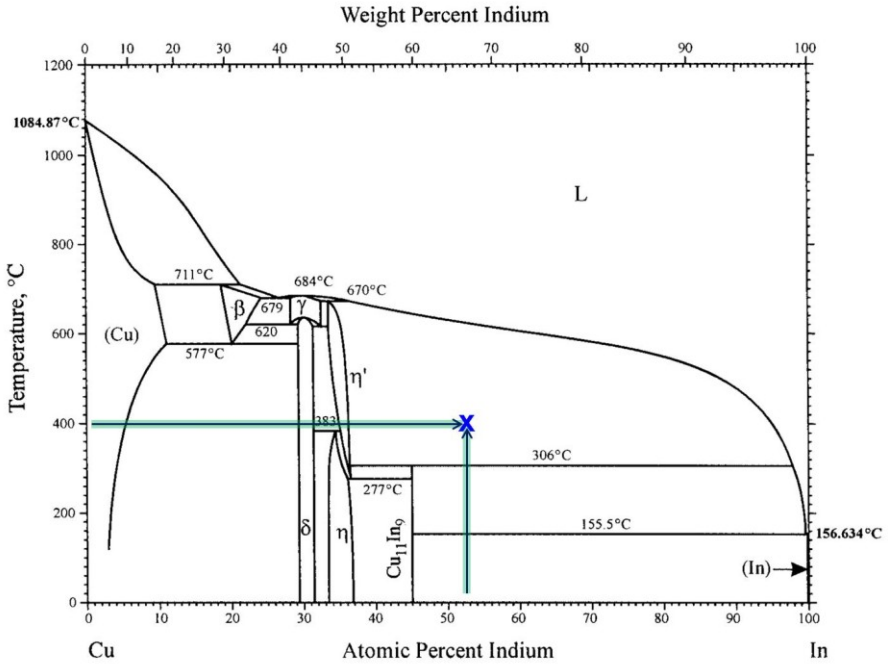

Figure 4.7 Cu-In phase diagram. The blue cross indicates the phase (liquid In with dissolved Cu and η'-$Cu_{16}In_9$) that the Cu/In bilayers had during pre-selenization annealing (PA) at 400 °C. The composition indicated is Cu/In ratio of ~0.9 (After Ref. [160].) (η'-$Cu_{16}In_9$ phase is from Ref. [158].)

XRD results (Fig. 4.8) showed common diffraction features of a chalcopyrite structure (PDF# 87-2265) including the strongest (112) peak regardless of the process sequence used for the film preparation. More precisely, the development of the double peak associated with (204) and (220) planes during the post-selenization annealing (inset in Fig. 4.8) indicated that the film had a sphalerite phase prior to the annealing (P0) and the structure evolved into a chalcopyrite through the annealing process (P1-P3). In addition, the presence of binary selenide phases was also confirmed in all CIS films according to the set of peaks associated with them,

and it requires further optimization effort in the thermal process to eliminate their formation. More importantly, their presence explains the vertical phase separation which caused the significant change in the Cu/In ratio observed throughout the thermal process. Because the conventional Bragg-Brentano configuration used for the diffraction measurement in Figure 4.8 was only sensitive to the bulk of the film, the glancing angle XRD (GAXRD) was also employed for a set of CIS films prepared under similar conditions to study the vertical phase distribution.

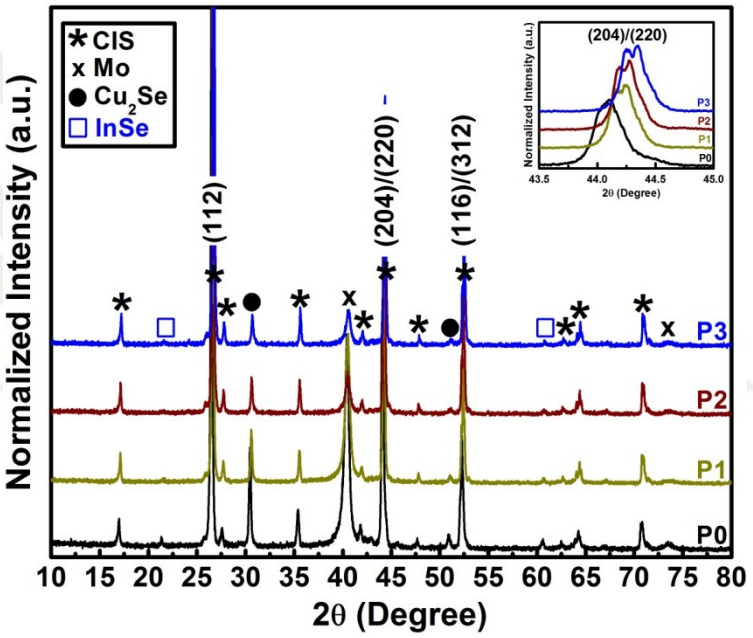

Figure 4.8 XRD patterns of CIS thin films prepared by four different process profiles (P0-P3). Peaks were normalized to the (112) peak. While P0 sample was not annealed after selenization, P1, P2 and P3 samples were annealed at 500 °C after selenization for 1hr (P1), 2 hrs (P2), and 3 hrs (P3). Inset shows the development of (204)/(220) peak splitting in the samples. (Cu_2Se PDF# 79-1841, InSe PDF# 71-0354, Mo PDF# 42-1120)

GAXRD patterns of P0 and P3 samples normalized to the (112) peak of CIS (Fig. 4.9) exhibited that the P0 sample had strong presence of the Cu-Se binary phases such as Cu_3Se_2, on its surface, whereas they did not exist on the surface of the P3 sample. This result explains the difference created by post-selenization annealing in the Cu/In ratio of P0 and P3 samples (Figs. 4.5 and 4.6). The P0 sample had a higher Cu/In ratio, because the strong presence of the Cu-Se binary phases brought its composition to a Cu-rich regime close to its surface. However,

the Cu/In ratio of the P3 sample was significantly lower than that of the P0 sample. Because after the post-selenization annealing the Cu-Se binary phases, which were responsible for the higher Cu/In ratio of the P0 sample, disappeared and consequently the Cu/In ratio of the P3 sample reduced. Moreover, the InSe phase present in the bulk of the P0 sample appeared on the surface of P3 and remained in the bulk as well, which is in support of the above analysis. Although the P0 sample had the InSe phase, it was not seen in its GAXRD spectra up to X-ray incidence angle (Ω) of 3° due to either its small amount existing or absence on the surface, reasoning the high Cu/In ratio of this sample. Meanwhile, the post-selenization annealing caused disappearance of the Cu-Se binary phases from the surface of the P3 sample resulting in a homogenous vertical distribution of the InSe phase in the film, hence the decrease in the Cu/In ratio of the P3 sample.

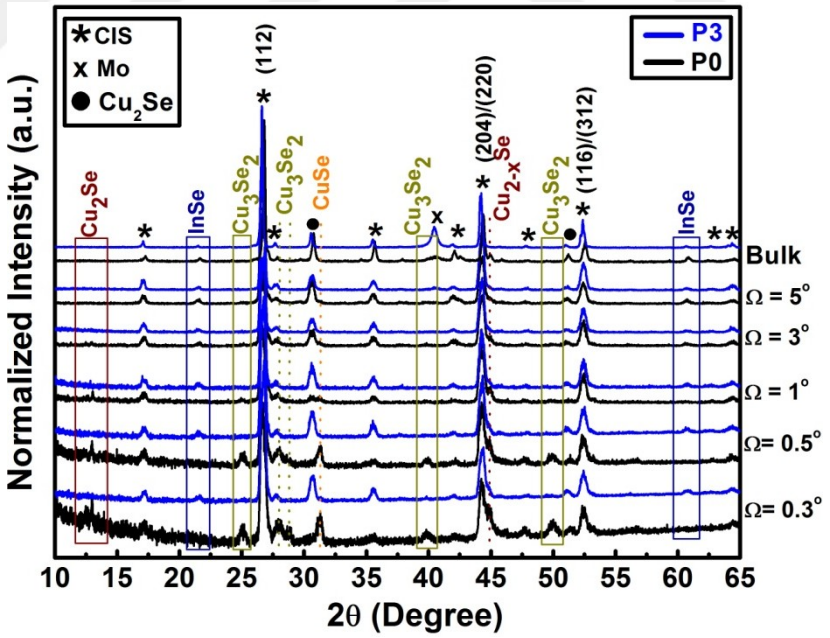

Figure 4.9 Bulk XRD and GAXRD patterns of P0 and P3 samples normalized to the (112) peak. P0 sample was not annealed after selenization, whereas P3 sample was annealed at 500 °C after selenization for 3 hrs. GAXRD measurements were performed at X-ray incident angles (Ω) of 0.3°, 0.5°, 1°, 3° and 5°. (CuSe PDF# 49-1457, Cu_3Se_2 PDF# 72-1421, $Cu_{2-x}Se$ PDF# 06-0680, either all Cu_2Se belongs to PDF# 29-0575 or Cu_2Se peak at 2θ ≈ 13° belongs to tetragonal Cu_2Se PDF# 29-0575 and Cu_2Se peaks at 2θ ≈ 31° and 2θ ≈ 52° belong to cubic Cu_2Se PDF# 79-1841)

According to the proposed models in the literature, CIS can form by a reaction between $Cu_{2-x}Se$ and InSe binary phases in the existence of Se [143, 159, 161, 162]. It was also proposed in Ref. [159] that CIS formation by In incorporation into a $Cu_{2-x}Se$ phase is also possible. According to the latter, Cu diffuses to the top of the film during the selenization and forms $Cu_{2-x}Se$ phase from which CIS grows with subsequent incorporation of In. Although CIS growth according to the both models can occur during selenization in our experiments, CIS growth by In incorporation into $Cu_{2-x}Se$ phase can be a possible explanation for observing the Cu-Se binary phases on the surface of P0 and for its high Cu/In ratio. However, $Cu_{2-x}Se$ formation was expected to discontinue at the top of the film during the post-selenization annealing where Se supply was absent (P1-P3) and CIS growth consumed the $Cu_{2-x}Se$ phases through reactions between $Cu_{2-x}Se$ and In-Se binary phases. In incorporation into the $Cu_{2-x}Se$ phase during the post-selenization annealing most likely discontinued as well because a decrease in the Cu/In ratio was not observed and stayed high at 1.68 when the post-selenization annealing was performed at 400 °C for 1 hr (not shown). In essence, In could have continued incorporating into the remaining $Cu_{2-x}Se$ phases at 400 °C even though the Se was absent decreasing the Cu/In ratio. Consequently, post-selenization annealing at 400 °C without a Se supply triggered occurrence of a low driving force for In to diffuse to the top of the film and incorporate into $Cu_{2-x}Se$ phase. It is possible that a lack of enough In concentration gradient between the surface and middle/bottom of the film was created by the discontinuation of $Cu_{2-x}Se$ formation when Se supply was absent reducing the driving force for In to diffuse to the top of the sample [159].

No change in the Cu/In ratio upon post-selenization annealing at 400 °C contrasted with the significant decrease in the ratio after annealing at 500 °C, and it indicated that the reaction between $Cu_{2-x}Se$ and InSe binary phases during the annealing became meaningfully fast when the temperature reached 500 °C. The increase in the reaction rate can be explained by the emergence of a quasi-liquid Cu-Se binary phase over 500 °C. The quasi-liquid Cu-Se binary

phase stems from the eutectic Cu-Se composition located at ~52.5 at% Se which forms at 523 °C according to the Cu-Se binary phase diagram (Fig. 4.10). Its exact composition can vary with the Se activity and temperature, and it can form at a lower temperature than 523 °C due to surface melting [163]. Without the mobile quasi-liquid phase at 400 °C, the reaction is expected to be very slow because the CIS phase, as a reaction product developed between the binaries can heavily impede the further reaction [164-166]. In addition, Se vacancies formed during the post-selenization annealing could have also increased the reaction rate between binary phases through increasing the interdiffusion of Cu and In [167, 168].

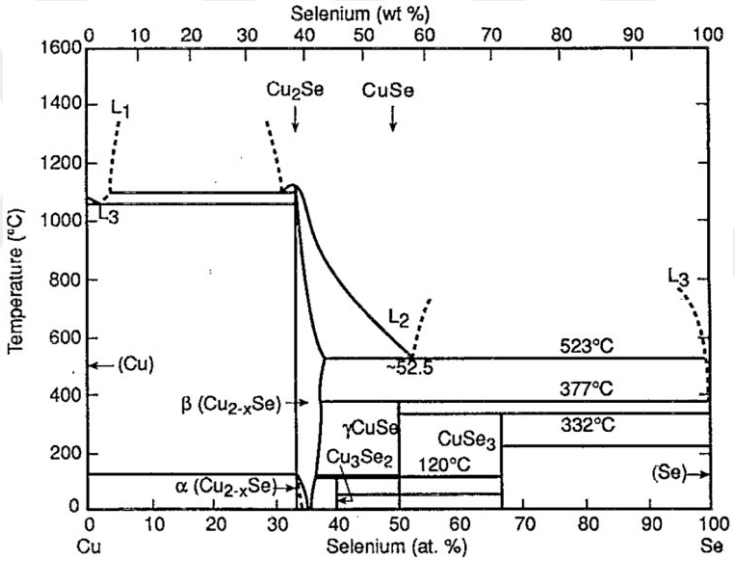

Figure 4.10 Cu-Se binary phase diagram [163].

SEM micrographs further showed that, upon post-selenization at 500 °C, the decrease in the Cu/In ratio occurred together with an increase in the grain size of the CIS thin films (Fig. 4.11), which can also be attributed to the benefit from the quasi-liquid Cu-Se phase.

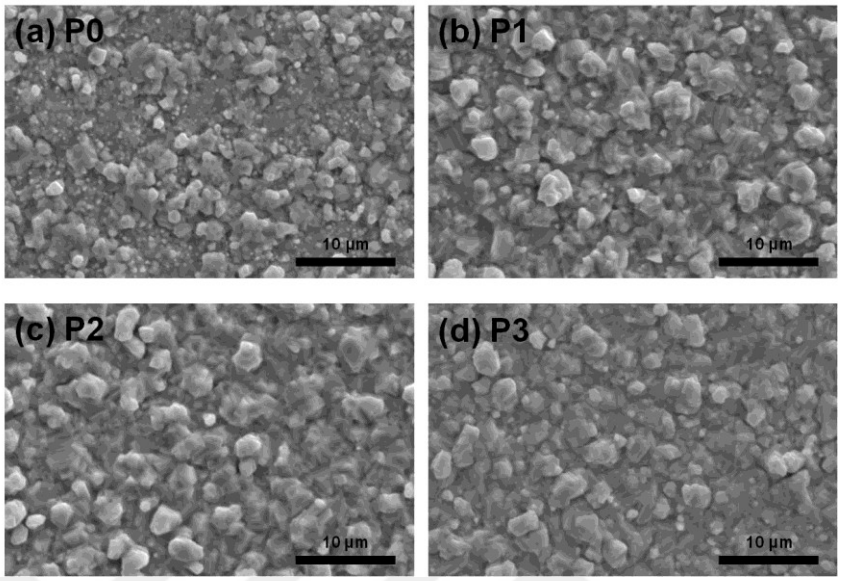

Figure 4.11 SEM images of CIS films: (a) selenized at 400°C (P0), and underwent post-selenization annealing at 500 °C for (b) 1 hr (P1), (c) 2hrs (P2), (d) 3 hrs (P3).

Although indium loss due to the formation of volatile In_2Se binary phase [139, 169] cannot be excluded, approaching to the targeted Cu/In ratio after a 3 hrs post-selenization annealing indicates that it should have been minimal in our experiments and the total amount of In did not alter significantly after selenization.

Among the first batch of CIS solar cells fabricated by the process profiles presented here, the cells prepared with the P1 CIS absorber layer produced the highest power conversion efficiency of 1.6% without any device optimization effort (Fig. 4.12). The relatively low open-circuit voltage (V_{OC}) can be ascribed to the presence of residual metallic $Cu_{2-x}Se$ binary phases (Figs. 4.8 and 4.9) that can be the source of low shunt resistance. In fact, solar cells fabricated with P0 layer did not show any photo-response which can be reasoned by the strong presence of the $Cu_{2-x}Se$ binary phases on its surface preventing the formation of a proper junction with CdS buffer layer. Future effort is necessary to optimize the selenization/annealing process further to prevent the presence of binary phases, particularly the $Cu_{2-x}Se$ phases.

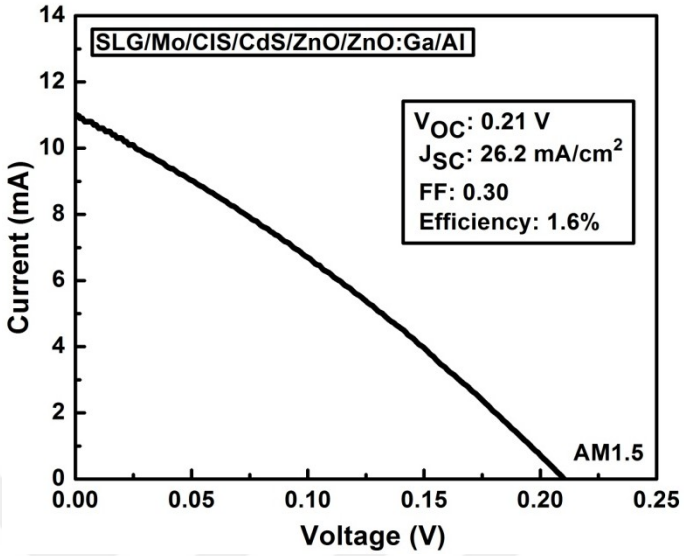

Figure 4.12 Output characteristics of a CIS solar cell prepared by using phenylselenocarboxamide and P1 process profile (annealed at 500 °C for 1 hr after selenization). The active area of the cell was 0.420 cm^2. V_{OC}: Open circuit voltage, J_{SC}: Short circuit current density, FF: Fill factor, AM: Air mass.

CIGS thin films and solar cells: Cu/III and Ga/III ratios of the as-deposited In-CuGa bilayers were 1 and 0.3, respectively, according to EDS, and their SEM micrograph showed that they had nodular grains with ~1 μm diameter (Fig. 4.13a). After the bilayers underwent P0 and P3 processes, the morphology consisted of grains with sizes ranging between ~0.5 μm to ~2 μm in the P0 sample (Fig. 4.13b) and equi-sized grains with ~1 μm diameter in the P3 sample which was possibly due to the quasi-liquid Cu-Se binary phase formed at 500 °C (Fig. 4.13c).

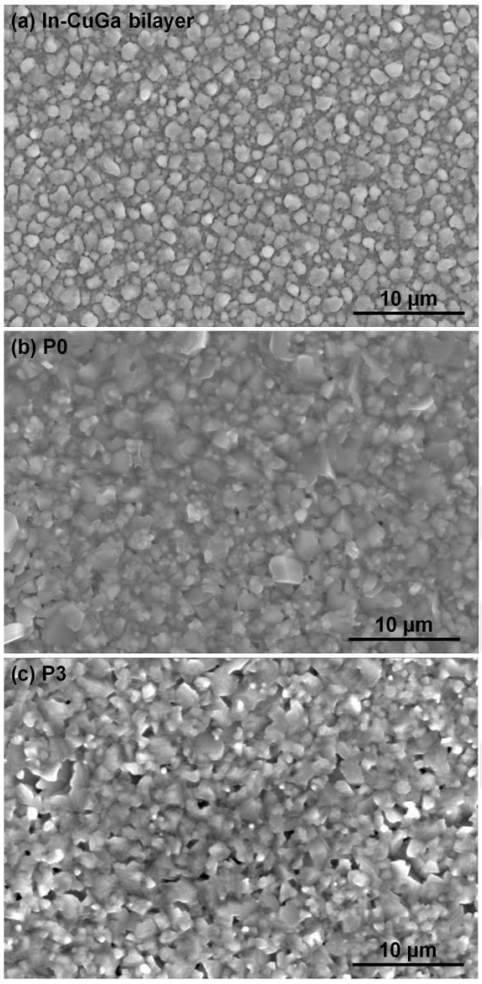

Figure 4.13 SEM images of (a) In-CuGa bilayer, and CIGS thin film (b) selenized at 400 °C (P0), and (c) underwent post-selenization annealing at 500 °C for 3 hrs (P3).

After selenization, significant difference was seen in the Ga/III ratios of the samples while both Cu/III and Se/(I+III) ratios of P0 and P3 samples were ~1 (Fig. 4.14). Decrease in the Ga/III ratio of P0 sample from 0.3 to 0.17 indicated Ga accumulation at the bottom of the sample, which was also evidenced by the point EDS measurements performed along the cross-section of the sample (Fig. 4.15).

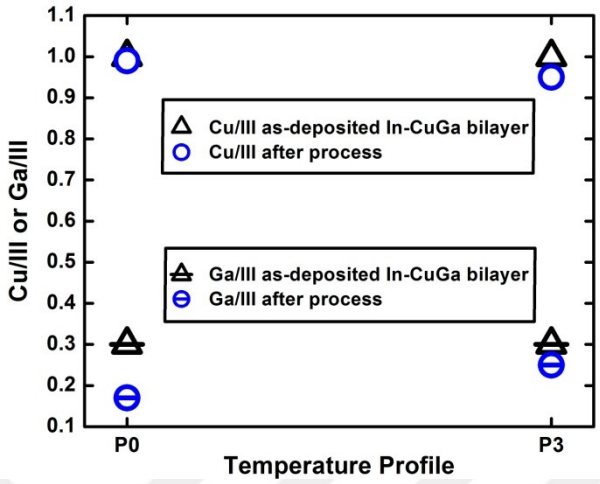

Figure 4.14 Cu/III and Ga/III ratios of the CIGS samples selenized at 400 °C (P0), and annealed at 500 °C for 3 hrs after selenization (P3) as determined by EDS.

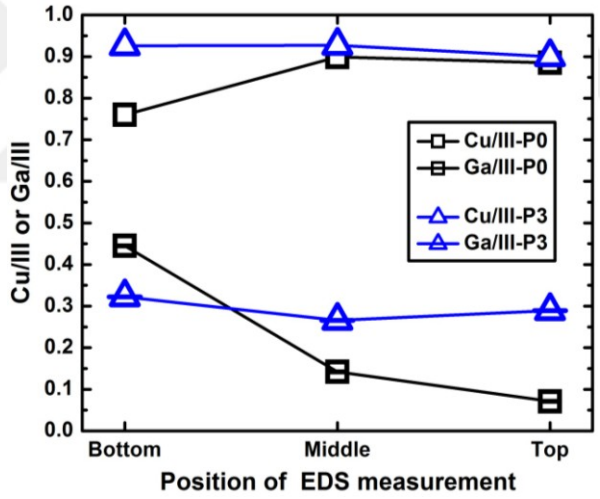

Figure 4.15 Cu/III and Ga/III ratios at the bottom, middle and top parts of the cross-sections of the CIGS samples selenized at 400 °C (P0), and annealed at 500 °C for 3 hrs after selenization (P3) as determined by point EDS measurements.

When a post-selenization annealing was performed, targeted Ga/III ratio of ~0.28 was approached through In and Ga re-distribution along the thickness of the P3 sample. Accumulation of Ga at the bottom of the CIGS thin film when it was prepared by selenization of stacked metal layers and subsequent In and Ga homogenization by a post-selenization annealing without a Se supply was seen in other studies as well [167, 168, 170]. It was proposed in Refs. [144, 167] that CIS phase grows with continuous In incorporation at the

reaction front due to the higher formation reaction rate of CIS than that of CGS, whereas CGS phase is naturally left at the bottom of the sample. However, Se vacancies created can increase the interdiffusion of In and Ga when a post-selenization annealing is performed without a Se supply resulting in a homogenized In and Ga distribution and hence increased reaction between CIS and CGS phases in the sample [167, 168]. These mechanisms can explain the difference observed in the Ga/III ratio of the samples in this study for which XRD and GAXRD results presented below gave more insight.

XRD results (Fig. 4.16) showed that In-CuGa metal bilayers were completely transformed to chalcopyrite phase in both P0 and P3 samples. Completion of the chalcopyrite formation was also evidenced by the existence of the $MoSe_2$ phase (PDF# 77-1715). The $MoSe_2$ phase forms once the chalcopyrite formation ends according to the time resolved high temperature XRD measurements performed during selenization which was supported by showing that standard reactions for CIS reduction by Mo had positive Gibbs energy change at 300 °C and 500 °C [166, 171]. It was also reported in Ref. [172] that a $MoSe_2$ layer is beneficial to the solar cell performance, since it favors formation of an ohmic contact at the Mo/CIGS interface rather than a Schottky contact. Moreover, the XRD results indicated a chalcopyrite phase separation in the P0 sample, since there were peaks in its XRD spectrum which were located at slightly higher 2θ angles than (112), (204)/(220) and (116)/(312) peaks of CIGS (PDF# 35-1102). These peaks were assigned as Ga-rich CIGS, because they were located at smaller 2θ angles than the known peaks of CGS phase (PDF# 75-0104) indicating that it was alloyed with In to a certain extent. Meanwhile, any chalcopyrite phase separation was not observable in the P3 sample. This result indicated an increased reaction between the chalcopyrite phases during the post-selenization annealing, which was also concluded by the shift of its (112) peak towards a higher 2θ angle (inset of Figure 4.16) when compared to those of the P0 sample and the CIS phase (PDF# 87-2265).

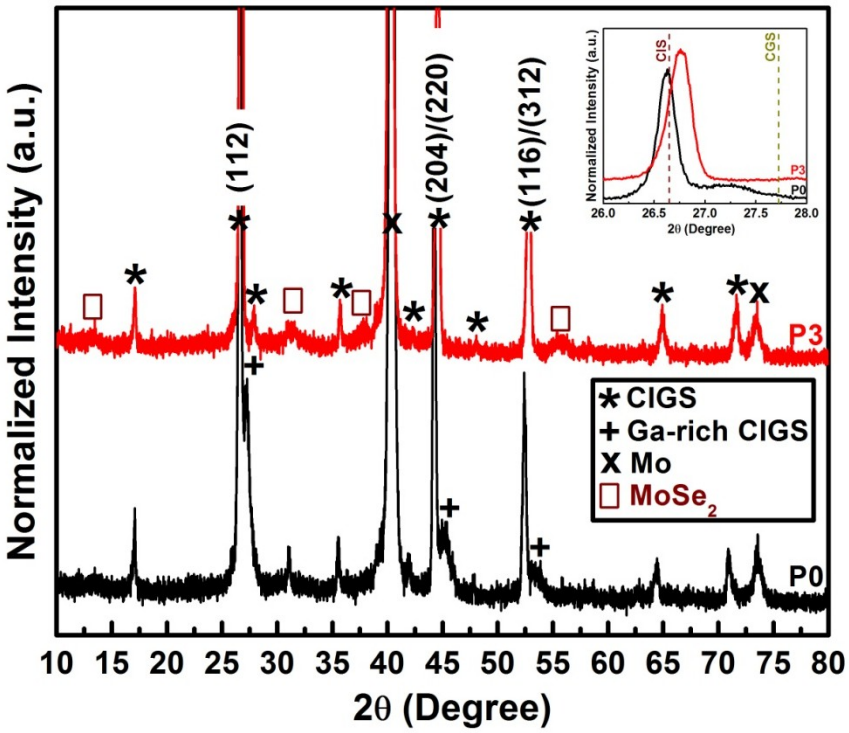

Figure 4.16 XRD patterns of CIGS samples selenized at 400 °C (P0), and annealed at 500 °C for 3 hrs after selenization (P3). Peaks were normalized to the (112) peak. Inset shows (112) peaks of both P0 and P3 thin films. Dashed lines in the inset show the locations of (112) peaks of CIS and CGS as reference.

GAXRD performed over the (112) peak of the CIGS thin films prepared under similar conditions with the P0 and P3 samples showed the difference in the extent of reaction between chalcopyrite phases in these samples. GAXRD results of the P0 sample (Fig. 4.17a) showed two distinct peaks which slightly shifted away from the 2θ angles of known peak positions of CIS and CGS phases towards each other confirming the phase separation due to premature intermixing between In and Ga in this sample. Moreover, the increase in the intensity of the Ga-rich CIGS peak and the shift of the CIGS peak towards higher 2θ angles were in agreement with the EDS measurements (Figs. 4.14 and 4.15) indicating the Ga accumulation towards the bottom of the P0 sample. However, GAXRD results of the P3 sample showed a further reaction between CIS and CGS phases in this sample, because the Ga-rich CIGS peak was absent (Fig. 4.17b). Although the P3 sample had a more uniform intermixing between In and Ga than P0, the

existence of an increase in the Ga concentration through thickness of the P3 sample was evidenced by the shift of the CIGS peak towards higher 2θ angles as the probed volume was deepened by increasing the X-ray incidence angle (Ω).

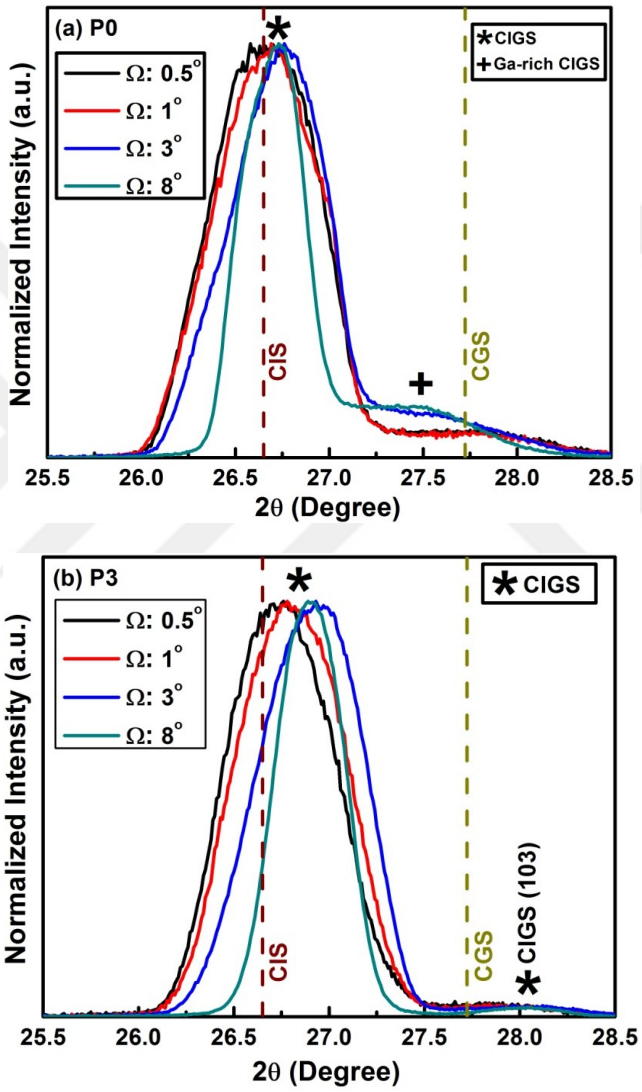

Figure 4.17 GAXRD measurements performed over the (112) peak of CIGS samples (a) selenized at 400 °C (P0), and (b) annealed at 500 °C for 3 hrs after selenization (P3). Peaks were normalized to the (112) peak. Measurements were performed at incident angles (Ω) of 0.5°, 1°, 3° and 8°. Dashed lines show the locations of (112) peaks of CIS and CGS as reference.

EDS (Figs. 4.14 and 4.15), XRD (Fig. 4.16) and GAXRD (Fig. 4.17) results of the P0 and P3 samples can give qualitative information on the bandgap profile created by Ga

distribution through the film thickness although a more comprehensive analysis requires a quantitative compositional depth profiling of these samples. Addition of Ga to CIS widens the bandgap by particularly increasing the conduction band (CB) minimum, whereas the valence band maximum is slightly decreased with Ga addition [173]. It was shown that both P0 and P3 samples had an increase in the Ga concentration at the Mo/CIGS interface which indicated a CIGS absorber with a bandgap profile [174]. In the profile, the bandgap gradually increases from the surface towards the back of the absorber, i.e. Mo/CIGS interface, (Fig. 4.18) which is beneficial for collection of the minority carriers from the Mo/CIGS interface before they recombine. Because in a CIGS absorber with a bandgap profile, the electrons excited to the CB of CIGS at the Mo/CIGS interface are subject to a potential gradient that makes them move towards the CIGS/CdS interface to be collected. Additionally, a higher bandgap of CIGS can be expected at the CIGS/CdS interface of the P3 sample compared to the P0 sample due to its higher concentration of Ga at the interface (Fig. 4.18) – higher bandgap at the CIGS/CdS interface will increase the open circuit voltage (V_{OC}) of the cell. Nonetheless, these hypotheses need to be tested on a device to observe the realistic outcome of the bandgap profiling on the device performance.

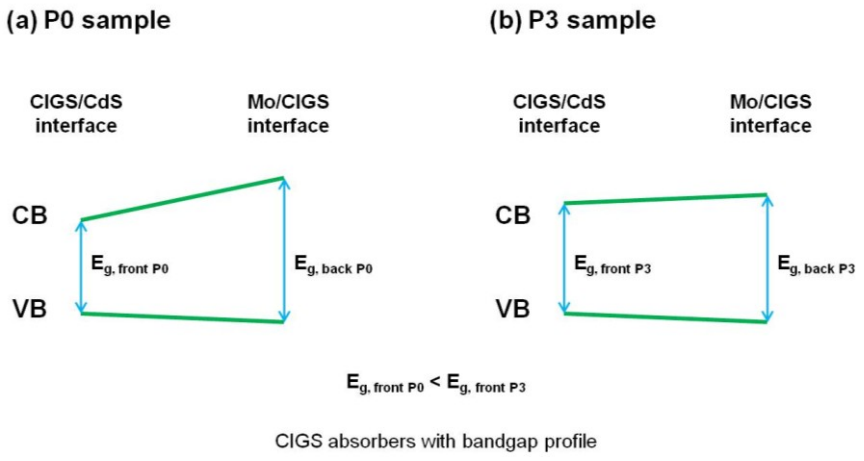

Figure 4.18. Schematic bandgap profiles of (a) the P0 sample and (b) the P3 sample. VB: valence band maximum; CB: conduction band minimum. (Bandgap profile schematics are after Ref. [174].)

Although a batch of CIGS solar cells prepared by P0 and P3 process profiles demonstrated an active junction, any significant photovoltage was not observed. The voids seen in the selenized films (Fig. 4.13b and 4.13c) possibly served as shunting paths deteriorating the cell performance.

4.4 Conclusions

Cu-In and In-CuGa metal bilayer thin films were successfully selenized into CIS and CIGS thin films by using selenoamide in an atmospheric pressure tube furnace. Observed vertical In and Ga segregation in CIS and CIGS thin films, respectively, after selenization was studied by designing systematic temperature process profiles. Selenization of Cu-In bilayers at 400 °C resulted in higher Cu/In ratio than that of metal bilayers. The initial increase in the Cu/In ratio was found to be due to In segregation towards the bottom of the film and chalcopyrite growth reaction. It was observed that while post-selenization annealing without a Se supply at 500 °C for 1-3 hrs homogenized In distribution in the films, it was not sufficient for obtaining single chalcopyrite phase due to slow kinetics of reaction between vertically segregated secondary phases. Conversely, selenization of In-CuGa thin films yielded single chalcopyrite phase together with the Mo_2Se phase which indicated that the CIGS formation reactions were completed. It was seen that selenization at 400 °C resulted in Ga segregation towards the bottom of the CIGS film, possibly creating a normal bandgap profile in the CIGS absorber. The post-selenization annealing without a Se supply at 500 °C for 3 hrs resulted in an increased intermixing between In and Ga. A bandgap profile still existed in the CIGS absorber after the 3 hrs post-selenization annealing, which was evidenced by the GAXRD and cross-sectional SEM-EDS results indicating the relative increase in Ga concentration towards the Mo/CIGS interface.

The first batch of cells prepared with SLG/Mo/CIS/CdS/ZnO/ZnO:Ga/Al structure demonstrated up to 1.6% power conversion efficiency. It was concluded that low shunt resistance due to the presence of Cu-Se binary phases in the CIS absorber could be the cause of low open circuit voltage and the efficiency. Although CIGS solar cells demonstrated an active

junction, voids observed in the CIGS absorber were thought to be possible reason for shunting path formation in the solar cells.

CHAPTER 5

EFFECT OF FLOW DYNAMICS ON THE GROWTH KINETICS OF CdS THIN FILMS IN CHEMICAL BATH DEPOSITION

Heterojunction in chalcopyrite solar cells is formed by depositing a ~50 nm thick *n*-type CdS thin film onto *p*-type Cu(InGa)Se_2 (CIGS) absorber layer. CIGS solar cells with the highest power conversion efficiencies (currently ~20 % [1, 2]) have been fabricated when the CdS is deposited by chemical bath deposition (CBD) method (CBD-CdS), although vacuum-based methods, such as evaporation, can also be used for CdS deposition. Obtaining a conformal CdS thin film on a rough CIGS surface can be reasoned as one of the beneficial effects of CBD-CdS, since obtaining a conformal thin film with vacuum-based physical vapor deposition methods on a rough surface is relatively harder. Moreover, reactions occurring between the chemicals in the bath and CIGS during CBD-CdS need to be considered when explaining the effects of CBD-CdS on CIGS solar cell performance. For example, ammonia used in the CBD-CdS process removes native oxides from CIGS surface during the deposition, increasing the junction quality [12, 14, 106, 175]. In addition, the effects of CBD parameters on deposition kinetics and properties of CdS thin films has a technological importance, for instance for designing CBD tools and processes particularly for high-volume CIGS solar cell manufacturing [175].

In this chapter, effect of the hydrodynamic condition in the chemical bath on growth kinetics of CdS thin films is studied. During CBD-CdS, the solution is typically stirred to prevent unnecessary concentration gradient and precipitates sticking onto the film surface. Stirring rate changes the thickness of laminar boundary layer over the substrate, affecting the diffusion length of the reactants towards the substrate. It can also change hydrodynamic condition in the bath between laminar and turbulent flow. Interestingly, effect of stirring rate on the deposition

kinetics of CdS thin films reported in the literature is conflicting. In this study, it was shown that the diffusion-limited deposition kinetics has created a decreasing profile of film thickness along the sample as a function of boundary layer thickness when the substrate was under laminar flow and deposition temperature was between 45 °C and 63 °C. On the other hand, the deposition became feed-limited when the substrate was under turbulent flow and the deposition temperature was between 45 °C and 63 °C. While the hydrodynamic condition changed the deposition rate significantly, all the CdS films deposited showed a cubic crystal structure and the optical bandgap was slightly lower than that of single crystalline cubic CdS. The tensile stress in film probed by Raman spectroscopy can explain the low bandgap.

Results from this study were appeared in the following, and the experimental background information on CBD-CdS can be found in Chapter 2 of this dissertation.

- M. E. Erkan and M. H.-C. Jin, "*Effect of flow dynamics on the growth kinetics of CdS thin films in chemical bath deposition*", Materials Chemistry and Physics 133, 779-783, 2012.
- M. E. Erkan and M. H.-C. Jin, "*Effect of flow type on film growth kinetics of CdS thin films in chemical bath deposition*", Poster presentation, IMRC 2010, Cancun, Mexico, 15-19 August 2010.

5.1 Introduction

Growth kinetics of CBD-CdS has been previously studied [32, 176-181] and most attention was paid on the effect of chemical concentration, deposition temperature and surface properties of substrate. Best to our knowledge, relation between hydrodynamic conditions of the chemical bath and the properties of CdS films has been scarce and was first discussed by Kaur et al. [176]. They deposited CdS films under both stirred and unstirred bath conditions and reported that deposition rate was faster in the unstirred bath. They claimed that stirring caused the cadmium and sulfur ions to arrive to the substrate's surface fast, causing the film grew ion by ion. It was also proposed in the same study that the films in the unstirred bath grew by

accumulation of CdS colloids (clusters), which first formed in the solution, onto the growth surface. However, they had not looked into the effect of stirring rate on deposition kinetics, which was later studied by Voss et al. [32], who showed that the deposition rate and hence final thickness of the CdS films increased as the stirring rate of the bath increased (Fig. 5.1).

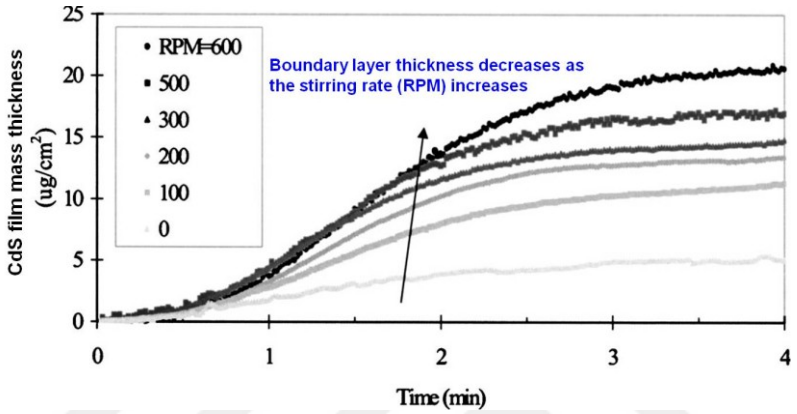

Figure 5.1 CdS film mass thickness (μg/cm^2) vs. deposition time plots obtained for different stirring rates (revolutions per minute, RPM) during chemical bath deposition. The measurements were performed by a quartz crystal microbalance probe dipped into the chemical bath solution, and only the stirring rate of the chemical bath was changed while other parameters were kept constant. After Ref. [32].

The finding was explained in terms of the change in the thickness of diffusion boundary layer over the substrate under the flow created by stirring. The hydrodynamic theory predicts that Reynolds number (Re) increases with the speed of the flow (v), and the thickness of the boundary layer (δ) over a flat plate reduces (Fig. 5.2) regardless of the boundary layer type existing, i.e. for both laminar (δ_l) and turbulent (δ_t) boundary layers, according to the following equations,

$$Re = \frac{vl\rho}{\mu}, \tag{5.1}$$

$$\delta_l = \frac{5x}{(Re_x)^{1/2}}, \tag{5.2}$$

$$\delta_t = \frac{0.376x}{(Re_x)^{1/5}}\ , \tag{5.3}$$

where l is the characteristic length of the body under flow, ρ and μ are, respectively, the density and the dynamic viscosity of the fluid, x is the distance from the leading edge of the flat plate, and Re_x is the Re at x [182, 183].

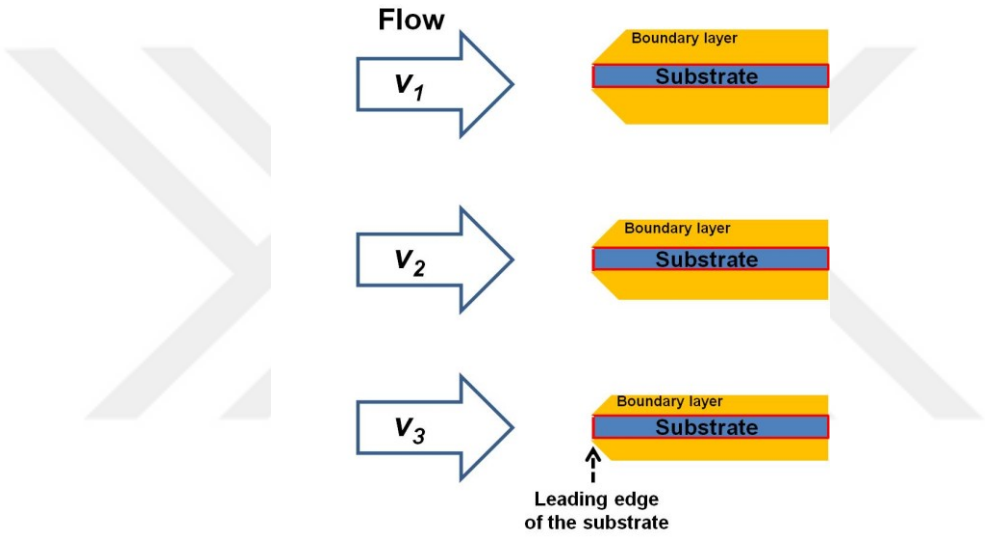

Figure 5.2 A schematic showing the change in the boundary layer thickness over a substrate with the flow speed (v), $v_1 < v_2 < v_3$. Thickness of the laminar boundary layer is inversely related to v according to Equations (5.1) – (5.3).

Therefore, it was explained that as the stirring rate increased, the thickness of the boundary layer decreased, reducing the diffusion length of the reactants towards the substrate and hence increasing the deposition rate – the deposition rate was diffusion-limited. Similar results were also reported by Kim et al. without much discussion on the relation between the hydrodynamics of the bath and the film deposition rate [177].

Wilchelmi et al. [178] reported the dependence of film growth kinetics on different *Re*. Although their results were conflicting with the studies mentioned so far, they have reached to a similar conclusion with Kaur et al. [176] in terms of the film growth model. They showed that the deposition rate of CdS films was almost independent of *Re* when *Re* was below 8000, suddenly

dropped at *Re* of 8000, and remained at the same level until *Re* was increased up to about 12,000 (Fig. 5.3).

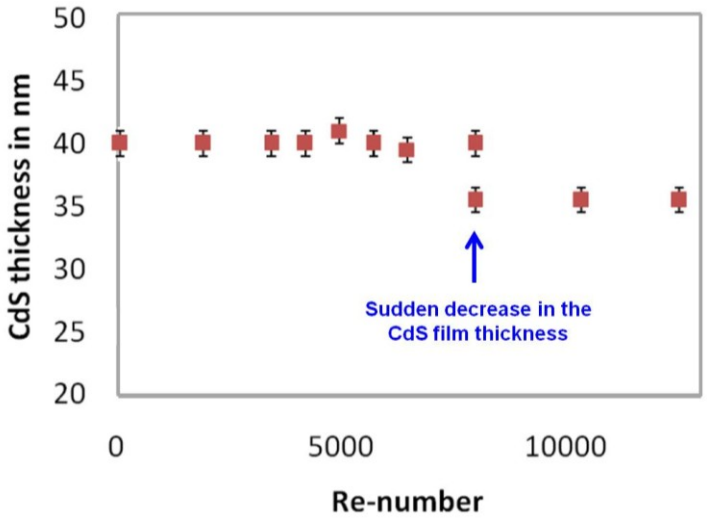

Figure 5.3 Relation between the CdS film thickness (nm) and the Reynolds number, *Re* of the flow in the chemical bath during chemical bath deposition. After Ref. [178].

The results led to the conclusion that CdS deposition was not diffusion-limited and the sudden decrease of the deposition rate at *Re* = 8000 was explained by the cluster-by-cluster growth model and the presence of threshold *Re* (i.e. stirring rate) which slowed down the deposition of CdS clusters on the growth surface. Moreover, it was also claimed by other researchers that CdS deposition kinetics does not depend on the hydrodynamic condition of the bath, i.e. deposition is not diffusion-limited [179, 180]. In addition to the hydrodynamic condition of the chemical bath, a recent study by Tec-Yam et al. [181] showed that substrate's orientation in the bath can also have an influence on the way chemicals are delivered to the substrate under different agitation modes inevitably affecting the deposition kinetics.

Overall, the results from the various studies cannot be explained by unified deposition kinetics. Here, we further studied the dependence of CdS deposition rate on the flow type and rate by using the thermal convection in the bath, which provided a simple flow configuration for the study. By having the substrate experiencing either turbulent or laminar flow in separate experiments, we were able to study the effect of different flow types on the deposition rate. The

results indicated that optical and structural properties of CdS films were not much affected by the hydrodynamic condition of the bath while the deposition could be as twice as faster depending on the flow type used.

5.2 Experimental Details

The CdS bath was prepared with 0.1 M stock aqueous solutions of cadmium sulfate and thiourea (both from Sigma Aldrich) and 28–30 wt.% ammonium hydroxide (Fisher) without further dilution from its original container. First, the ammonium hydroxide solution was added into the beaker that had contained the cadmium sulfate solution at room temperature. Since ammonium hydroxide evaporates easily, the beaker was kept covered with a plastic sheet until the end of deposition process, except while adding thiourea and inserting the substrate. After the solution in the beaker was stirred for 5 min using a magnetic stir bar, the thiourea solution was added and it was stirred for an additional 2 min. The final concentrations of cadmium sulfate, thiourea, and ammonium hydroxide in the bath were 1.96×10^{-3} M, 4.9×10^{-2} M, and 1 M, respectively. Before the substrate (1 in. × 1 in. microscope glass from Fisher) was inserted into the solution, the stir bar was removed from the beaker and pH of the solution was measured with a pH strip (EMD colorpHast). The pH was around 11 for all chemical bath solutions used in this study.

Right after the substrate was placed in the solution, the bath was started to be heated and the temperature was set to the target temperature by a plate heater underneath the beaker. To make depositions under different flow conditions, substrates were placed into the beaker with two different angles of incline (θ) with respect to the bottom of the beaker (Fig. 5.4) [184]. The turbulent flow with respect to the substrate was obtained when $\theta = 0°$, and the laminar flow over the substrate was realized with the angle of 90°.

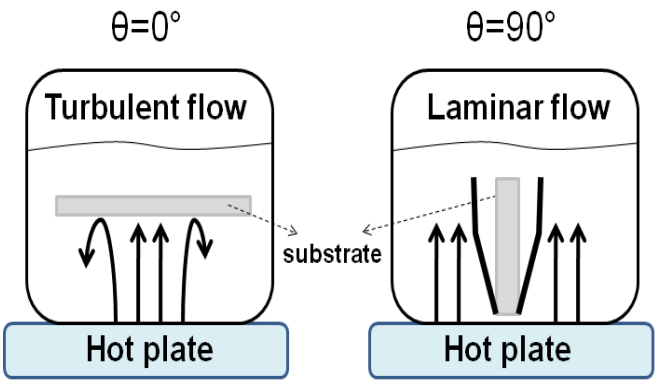

Figure 5.4 Layout of the substrate during the chemical bath deposition of CdS thin films. Substrate angle of incline (θ) with respect to the bottom of the beaker was set to 0° and 90° to create a turbulent and a laminar flow, respectively, using a hot plate under the beaker.

When the desired temperature was reached, the substrate was removed from the bath, rinsed with de-ionized (DI) water, and dried with blown air. Depositions were made with different target bath temperatures of 30 °C, 45 °C, 55 °C and 63 °C under both turbulent and laminar flows. Single deposition of CdS at the target temperature of 30 °C took 1 h and the deposition was made twice on the same substrate to achieve the film thick enough for all the analysis. The time necessary to make a single deposition of an analyzable film at all other target temperatures was 35 min except for a film made at 45 °C for X-ray diffraction (XRD) analysis – two 35 min depositions were made on the same substrate. The flow rate in the bath was controlled by the deposition temperature, which allowed varying Re of the flow, and hence the thickness of boundary layer over the substrate under laminar flow. Comparison among different flow rates at θ of 90° was made by creating flow visualization, in which a mixture of blue ink and milk was injected into a beaker of DI water on the hot plate and a flashlight was located behind the beaker to make the flow clearly visible allowing the measurement of the speed of flow (Fig. 5.5). The speed of flow was determined for the minimum and the maximum temperatures used for CdS deposition in this study, and the speed measured at 30 °C and 63 °C was 0.2 cm/s and 1.0 cm/s, respectively. In order to confirm the laminar flow ($Re_x < 2 \times 10^5$) [14,15], Equation 5.1

was used to estimate Re of the flow, and it was 68 at 30 °C and 559 at 63 °C when the speed of flow measured by flow visualization, the substrate length, the dynamic viscosity and the density of pure water were used for the calculation (Table 5.1) [185].

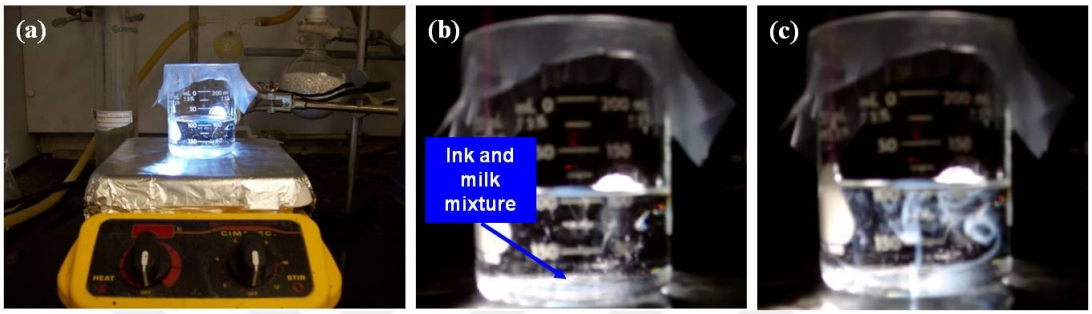

Figure 5.5 Set-up used for visualizing flow in the water bath: (a) the entire set-up and the snapshots (b) at the beginning of heating and (c) 45 sec after the start of heating at 63 °C.

Table 5.1 Values used for calculation of the Reynolds number (Re) associated with the water flow used in the CdS chemical bath.

Bath temperature (°C)	Substrate length (cm)	Viscosity of water (cp)	Density of water (kg/m^3)	Speed of flow (cm/s)	*Re*
30	2.54	0.797	996	0.2	68
63		0.446	982	1.0	559

Optical transmittance and reflectance measurements of the CdS thin films were made by UV/VIS/NIR spectrometer (Perkin Elmer, Lambda 19). Before optical measurements, the film on the backside of the substrate was etched away with HCl to have the film only on one side of the substrate. The optical analysis assumed no interference and the measured reflectance was considered to be the only reflection from the front surface of the film. The absorption coefficient (α) of the film was calculated by using Equation 5.4 [75],

$$T = (1 - R)e^{-\alpha l}, \tag{5.4}$$

where T is transmittance, R is reflectance, and l is the thickness of the film. The optical bandgap of the film was determined by extrapolating the linear portion of the curve to zero absorption in a α^2 vs. photon energy plot knowing that CdS has a direct bandgap.

A step necessary for the thickness measurement was created along the substrate by using dilute HCl and the measurements were made by a surface profiler (Tencor, P-10). In particular, the steps created on CdS thin films deposited under laminar flow condition (θ = 90°) were carefully made by considering the direction of the flow during the deposition to evaluate the effect of boundary layer thickness on the deposition rate. Raman spectra of CdS thin films were acquired by using a microscopic Raman spectroscope (Thermo Scientific, DXR) with a 532 nm laser. Morphology and the crystal structure of the samples were investigated, respectively, by scanning electron microscope (SEM) (Hitachi, S-3000N) and XRD (PANalytical, X'Pert Pro).

5.3 Results and Discussion

The results of thickness measurements on all the deposited films are compiled in Fig. 5.6 including the variation of thickness along the substrates. At low temperature – at least up to 45 °C, the flow type did not change the average thickness much and the thickness profile along the sample indicating the growth kinetics is identical for both flow types being either reaction-limited or feed-limited. Fig. 5.6d shows that the thickness of the CdS film deposited at 63 °C under laminar flow (θ = 90°) has its biggest value close to the edge of the sample where the laminar boundary layer is the thinnest.

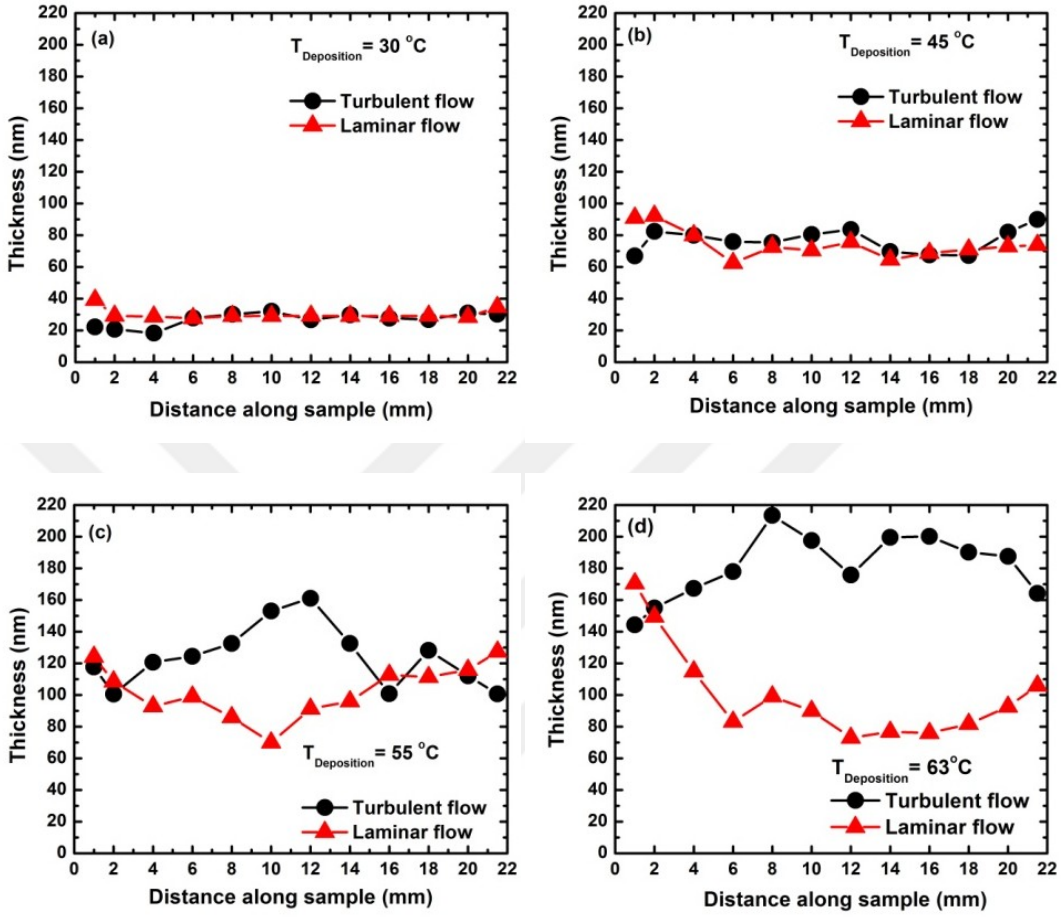

Figure 5.6 Thickness profile of CdS films along the substrates: (a) deposition temperature ($T_{Deposition}$) of 30 °C, (b) 45 °C, (c) 55 °C, and (d) 63 °C. 0 mm distance indicates the edge of the 1 in. × 1 in. size substrate. For the CdS films deposited under laminar flow condition, 0 mm distance corresponds to the bottom edge of the substrate at which the boundary layer started to develop. Thickness of CdS films deposited at 30 °C was normalized to 35 min-deposition time.

Laminar boundary layer thickness over a flat plate gradually increases as it develops starting from the leading edge of the plate. Accordingly, the diffusion length of the reactants gradually increases along the substrate following the direction of the flow. In addition, change in CdS grain size along the substrate proves the effect of boundary layer thickness on the deposition rate (Fig. 5.7).

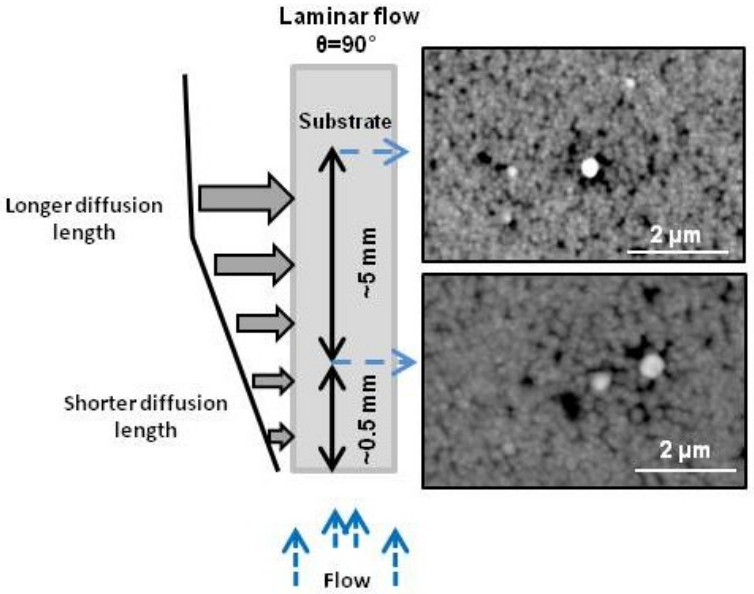

Figure 5.7 Schematic of change in the thickness of laminar boundary layer along the substrate and scanning electron micrographs of CdS films deposited at 63 °C. The micrograph obtained at the distance of 5 mm (top) shows the grain size smaller than that at 0.5 mm (bottom).

Dependence of deposition rate on the thickness of boundary layer explains that the deposition kinetics of CdS films under laminar flow is diffusion limited. While this trend did not clearly show up in the film deposited at 55 °C, the flow type certainly made a difference in the deposition rate, which would explain that the transition between two different deposition kinetics was occurring at 55 °C. On the other hand, the thickness profile of the films deposited under turbulent flow (θ = 0°) was very irregular along the sample possibly due to the turbulent nature of the flow. Additionally, the thickest part of the films appeared in the center of the substrates indicating the kinetics was governed by the amount of physical flux arriving at the growth surface – this can exclude the possibility of being reaction-limited growth as the surface temperature was expected to be constant along the sample and such inhomogeneity cannot be expected from the reaction-limited kinetics. The overall difference in deposition kinetics of CdS thin films deposited under turbulent and laminar flow at various deposition temperatures is shown in Fig. 5.8.

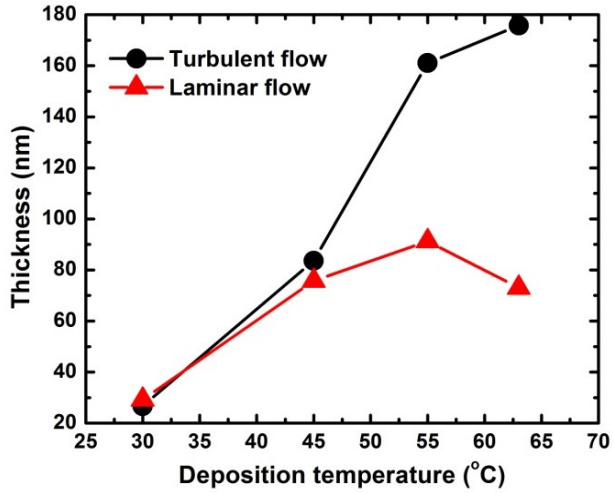

Figure 5.8 Thickness of CdS films approximately at the middle of the substrates −12 mm away from the edge of the sample. Thickness of CdS films deposited at 30 °C was normalized to 35 min deposition time.

It should be noted that the thickness data were taken at the center of the samples for both flow types. Below 45 °C, the deposition kinetics was either limited by insufficient thermal energy due to low deposition temperature or by slow convective flux regardless of the flow type. As the target temperature further increased over 45 °C, deposition rate under turbulent flow continuously increased as higher temperature created faster convective flux of reactants, whereas the rate relatively slowed down for laminar flow as diffusion through the boundary layer started governing the deposition kinetics.

CdS shows polymorphism at room temperature; it can exist in stable hexagonal or metastable cubic crystal structures [29]. XRD results (Fig. 5.9) show that CdS thin films have cubic crystal structure regardless of the deposition temperature and the flow type used. In fact, all the diffraction peaks identified as (111), (220) and (311) of the cubic structure are closely located, respectively, at the positions for (002), (110) and (112) of hexagonal structure, which made the crystal structure determination difficult. However, the absence of the strongest peak of hexagonal structure, i.e. (101) located at 2θ of 28.2°, supports the analysis. Although the slow deposition rate under laminar flow might drive the crystal to be hexagonal, it is possible that the temperature was too low to realize the stable phase.

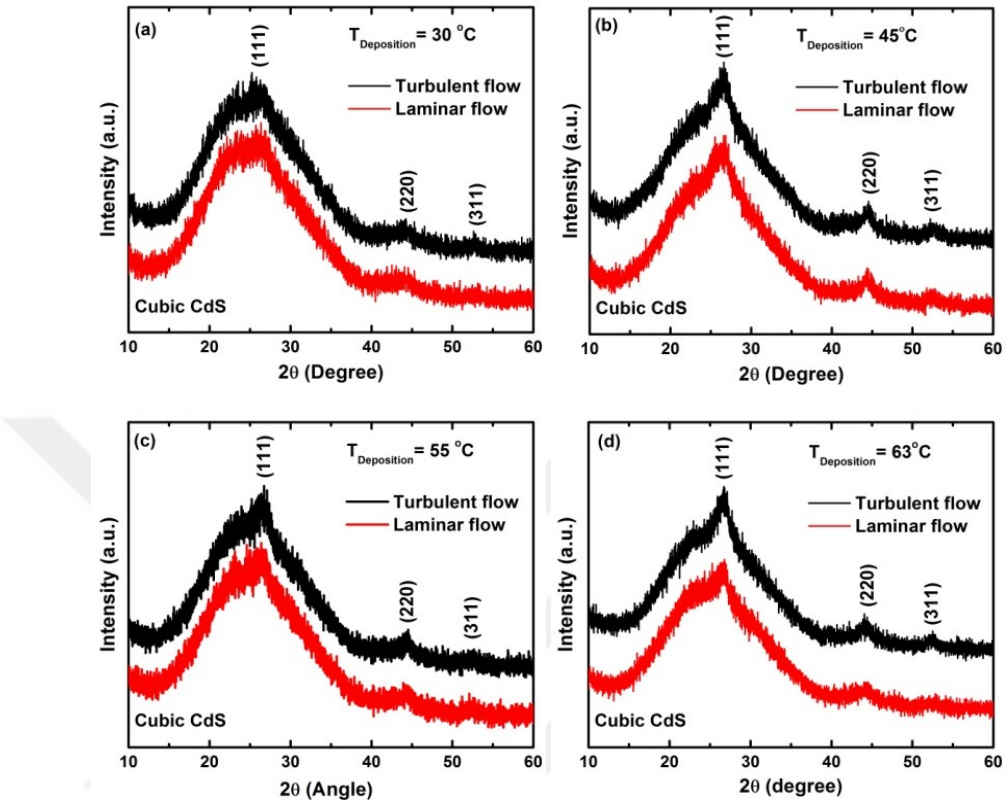

Figure 5.9 XRD spectra of CdS films deposited under different flow types and deposition temperatures: (a) deposition temperature ($T_{Deposition}$) of 30 °C, (b) 45 °C, (c) 55 °C, and (d) 63 °C.

The first longitudinal optical (1LO) phonon mode of CdS was identified through the Raman shift of 300–303 cm^{-1} from all the CdS films deposited in this study regardless of deposition condition (Fig. 5.10). In addition, all of them showed a red shift from the known Raman shift of the cubic-phase CdS bulk crystal (305 cm^{-1}) [186-188] (Fig. 5.11).

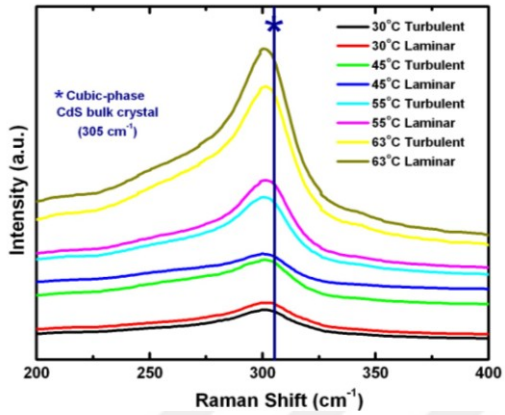

Figure 5.10 Raman spectra of CdS thin films deposited under laminar and turbulent flow conditions in the chemical bath at different deposition temperatures. The first longitudinal optical phonon mode of CdS is located at Raman shift of 300–303 cm^{-1}.

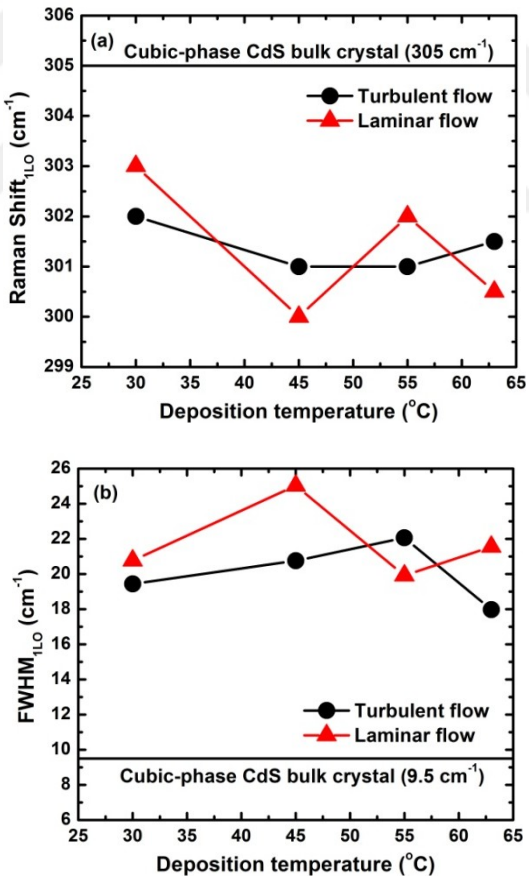

Figure 5.11 (a) Raman shift and (b) full-width-at-half-maximum (FWHM) of the first longitudinal optical (1LO) phonon mode of CdS films deposited under different flow types and temperatures. The Raman shift and FWHM of the cubic-phase CdS bulk crystal are from the literature [186-188].

The red shift is attributed to tensile stress in the films developed during film growth [189]. The tensile stress can also explain the optical bandgap of the CdS films deposited in this study being often lower than that of single crystalline cubic CdS (2.4 eV) [24] (Fig. 5.12). Optical bandgap of the CdS films was determined by extrapolating the linear portion of their respective α^2 vs. photon energy curves (Fig. 5.13) to zero absorption.

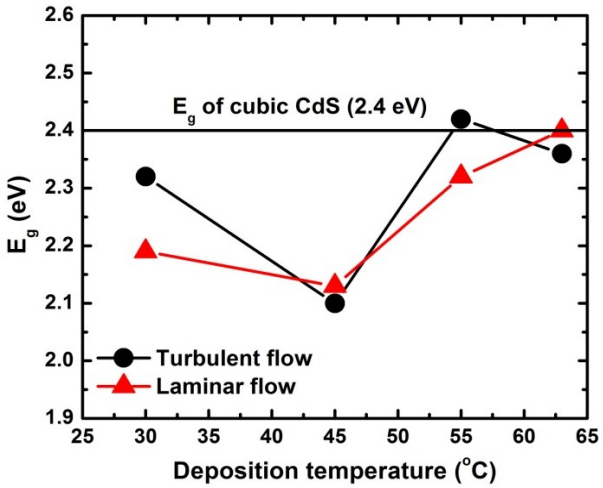

Figure 5.12 Optical bandgaps of CdS films deposited under different flow types and temperatures. The bandgap of the cubic-phase CdS bulk crystal is from the literature [190].

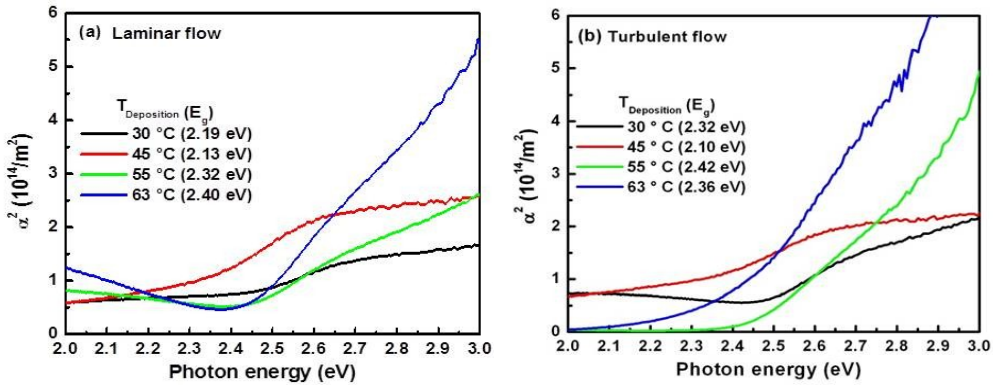

Figure 5.13 α^2 vs. photon energy graphs of CdS films deposited under (a) laminar and (b) turbulent flow conditions at deposition temperature ($T_{Deposition}$) of 30 °C, 45 °C, 55 °C, and 63 °C.

While the effect of film thickness on the bandgap (Fig. 5.14) was inconclusive, the bandgap seemed becoming larger at higher deposition temperatures.

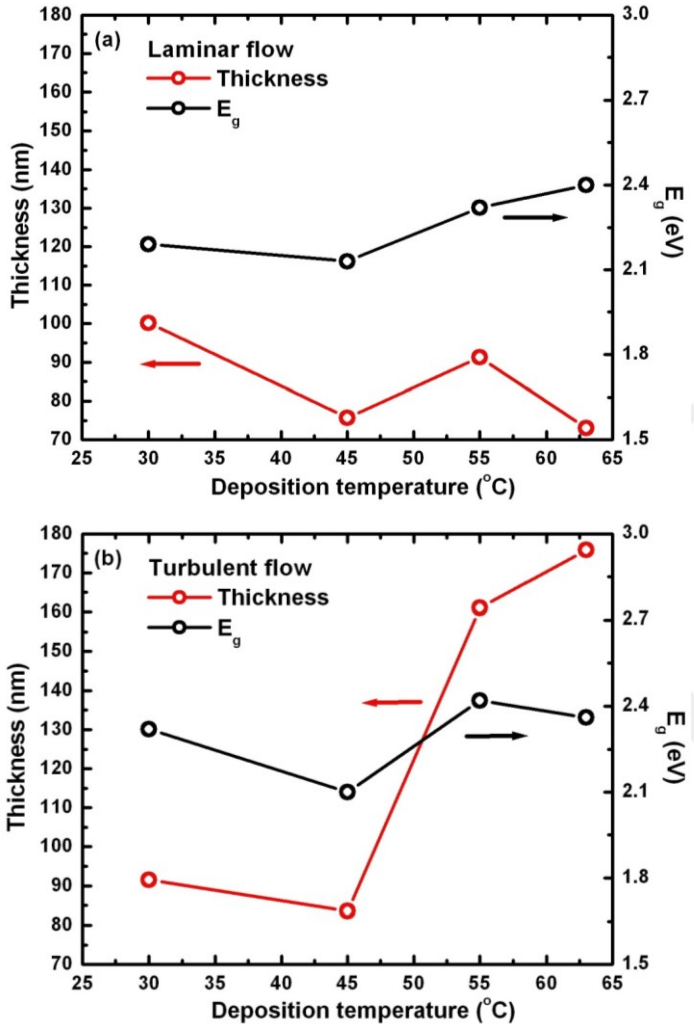

Figure 5.14. Relation between thickness and bandgap (E_g) of CdS thin films deposited at different deposition temperatures under (a) laminar flow and (b) turbulent flow conditions.

5.4 Conclusion

The flow type during the chemical bath deposition of CdS thin films was directed by the thermal convection created using a plate heater under the bath and the placement of the substrate. Dependences of growth kinetics and the optical and structural properties of CdS films on the flow type were investigated. The film growth kinetics was either reaction-limited or feed-limited regardless of the flow type below deposition temperature of 45 °C, and it became diffusion-limited under laminar flow at higher deposition temperatures as the film deposited

under laminar flow at 63 °C clearly showed the effect of boundary layer thickness on the deposition rate along the substrate. In the meantime, inhomogeneous thickness profile of the film along the sample indicated that the deposition kinetics under turbulent flow above 45 °C was more likely feed limited. Although the results showed the dependence of the film deposition rate on the hydrodynamic condition of the bath, optical and structural properties of the CdS films did not significantly depend on the flow type in the bath. All CdS films had cubic crystal structure, and they grew with tensile stress which caused lower bandgap energy of the CdS films with respect to that of the cubic-phase CdS bulk crystal.

CHAPTER 6

SUMMARY

Three studies on chalcopyrite solar cells are presented in this dissertation. In this final chapter a summary of all three studies are given.

A study on the electronic activities of Σ3, ~Σ3 and Σ9 grain boundaries (GBs) in a Bridgman-grown Na-free $CuInSe_{2.1}$ (CIS) wafer was presented in Chapter 3. Studying both Σ3 and non-Σ3 GBs were important, because Σ3 GBs are abundant in the chalcopyrites and the difference in the electronic properties of Σ3 and non-Σ3 GBs could give a clue on the unexpected high efficiencies obtained in polycrystalline chalcopyrite solar cells. Moreover, best to the author's knowledge, a study on Σ3 and non-Σ3 GBs in a Na-free CIS with complementary methods has not been reported so far. The electronic properties of the GBs crystallographically identified by electron backscatter diffraction were studied by Kelvin probe force microscopy and cathodoluminescence in scanning electron microscope (SEM-CL). Investigating the GBs in a Na-free wafer was essential for understanding the electronic behavior of chalcopyrite GBs without any external influence, because when Na is present in chalcopyrites it segregates to the GBs. Moreover, a Na-related secondary phase formation could be possible in the presence of Na which will inevitably affect the electronic behavior of a GB. In this study, it was shown that the electronic behavior of chalcopyrite GBs in a Na-free CIS could be viewed by the classical semiconductor GB model which explains the electronic properties of GBs by the GB electronic states existing due to the defects. Because although both Σ3 and ~Σ3 GBs were neutral according to KPFM, ~Σ3 GB was a recombination center according to the SEM-CL. In fact, in this case the ~Σ3 GB was expected to be charged; however, it was concluded that the existing contact potential difference (CPD) measured by KPFM was less than the detection limit of the

measurement. Nonetheless, it was clear that the misorientation angle deviation from being an exact Σ3 GB was sufficient to introduce midgap states at the ~Σ3 GB. As the geometric deviation from being a Σ3 GB increased more, i.e. increased amount of defects at the GB, the electronic behavior of the GB changed in agreement with the classical GB model. The Σ9 GB had ~100 mV downwards band bending as measured by KPFM. In agreement with the band bending at the Σ9 GB, its SEM-CL result demonstrated the significant recombination activity occurring at the Σ9 GB. Overall, it was concluded that the electronic behavior of GBs in the Na-free CIS depended on the amount of defects existing at the GB which in turn affects the density of the midgap states at the GB. It can also be argued that the successful device performance seen in polycrystalline chalcopyrite solar cells can be due to the electronically inactive Σ3 GBs which, according to our results, should not disturb the charge carriers, hence device performance. However, this statement should include an assumption: Σ3 GBs are harmless to the solar cell performance as long as Na impurities do not change their electronic behavior. To be able to test this, future work was projected which requires studying Σ3 and non-Σ3 GBs in CIS wafers with gradually increased Na concentration.

In Chapter 4, the feasibility of using selenoamide as a Se source for selenization was demonstrated for the first time. Cu-In and In-CuGa metal bilayers were selenized into CIS and $Cu(In,Ga)Se_2$ (CIGS) thin films successfully by using selenoamide in an atmospheric pressure tube furnace at 400 °C. The observed segregation of In in CIS and that of Ga in CIGS during selenization and their re-distribution by post-selenization annealing at 500 °C were studied by phase transformations occurring during systematically designed annealing processes. The segregation of In towards the bottom of CIS was concluded to be due to the heavy presence of the Cu-Se binary phases observed close to film surface by glancing angle X-ray diffraction (GAXRD). It was also shown that In re-distribution in the film together with disappearance of the Cu-Se binary phases from the surface was occurred gradually once a post-selenization annealing at 500 °C was applied without Se supply for 1-3 hrs. A possible explanation for this

result was formation of a quasi-liquid Cu-Se binary phase at 500 °C. Consequently, an increase in the reaction rate between Cu-Se and In-Se (or In) at 500 °C occurred due to the existence of quasi-liquid phase which favored re-distribution of In in the CIS thin films. Increased grain size in CIS thin films was an indication of the existence of a quasi-liquid phase during post-selenization annealing at 500 °C. On the other hand, Ga segregation toward the bottom of the CIGS after selenization was observed and interpreted as formation of a bandgap profile in the CIGS thin film. Although a post-selenization annealing at 500 °C for 3 hrs favored re-distribution of Ga and increase of the Ga concentration at the surface of the CIGS films, a gradual increase in the Ga concentration towards the bottom of CIGS was still evident by the results obtained from GAXRD and cross-sectional energy dispersive X-ray spectroscopy (EDS) in SEM. Therefore, it was suggested that after the post-selenization annealing, bandgap profile was accompanied by an increase in the bandgap at the surface which could increase the open circuit voltage of a CIGS solar cell. However, although the fabricated CIGS solar cells demonstrated an active junction, it was possible that the voids seen on the selenized films formed shunting paths in the solar cells. On the other hand, the first batch of CIS solar cells fabricated with soda-lime glass/Mo/CIS/CdS/ZnO/ZnO:Ga/Al structure demonstrated up to 1.6% power conversion efficiency. The low efficiency was concluded to be due to the presence of secondary phases in CIS thin films which served as shunting paths in the fabricated solar cells. Therefore, further optimization in the selenization and annealing processes is necessary to obtain single phase CIS thin films and to prevent void formation in CIGS thin films.

The final study was on the dependency of CdS deposition kinetics on the flow type over the substrate in the chemical bath deposition (CBD). CBD-CdS is used in chalcopyrite solar cells to form the *p-n* junction. This study was designed to address the conflict seen in the literature on the effect of chemical bath's hydrodynamic condition on the deposition kinetics of CdS thin films. Stirring is a common practice during CBD of CdS to obtain a homogenous distribution of chemicals in the bath and to prevent precipitates sticking onto the surface of CdS

thin film. In studies reported in the literature, the hydrodynamic condition of the bath was regulated by stirring the bath and/or stirring rate. However, in this study CdS thin films were deposited under laminar and turbulent flow conditions over the substrate in an unstirred bath. This was achieved by utilizing natural flow occurring in the bath due to the thermal convection created by placing a plate heater under the bath. Laminar and turbulent flow conditions were obtained by changing the alignment of the substrate with respect to the bottom of the beaker. When the substrate was parallel to the bottom of the beaker, turbulent flow over the substrate was obtained, and when the substrate was aligned perpendicular to the bottom of the beaker laminar flow over the substrate existed. The main outcome of the study was the difference in the CdS deposition rate when different flow type existed. The deposition rate was significantly higher under the turbulent flow condition. It was proposed that the reaction was diffusion-limited when laminar flow existed; meanwhile, the deposition was feed-limited under the turbulent flow condition. Because the laminar flow creates a boundary layer over a substrate that the reactants need to diffuse through to reach the substrate, whereas the reactant flux is directly incident onto the surface of the substrate when turbulent flow exists. This was also evidenced by the gradual change in the CdS film thickness over the substrate when the deposition was made under the laminar flow condition. When a laminar boundary layer starts to develop over a flat plate from a leading edge, the thickness of the boundary layer has its thinnest value at the leading edge and its thickness gradually increases, hence the diffusion length of the reactants towards the substrate. Despite the deposition rate difference, the optical and structural properties of CdS thin films were the same regardless of the flow type in the bath. As a result, it was shown that turbulent flow had its advantage over the laminar flow by its higher CdS deposition rate which is technologically important, for instance, when a large-scale CIGS solar cell manufacturing is considered.

APPENDIX A

MISORIENTATION ANGLE/AXIS DESCRIPTION OF GRAIN BOUNDARY GEOMETRY AND GRAIN BOUNDARY CLASSIFICATION BY COINCIDENCE SITE LATTICE MODEL

One of the ways of describing the geometry of a grain boundary (GB) is the misorientation scheme which is the base for coincidence site lattice (CSL) classification of GBs. If we consider two grains as interpenetrating lattices in space (Fig. A.1), the first one is fixed and the second one is rotated around a common axis, [*uvw*] by an angle of *θ* with respect to the first grain. It should be mentioned that naming the grains as 'first' and 'second' and the relation between the misorientation axis, [*uvw*] and the GB plane are arbitrary.

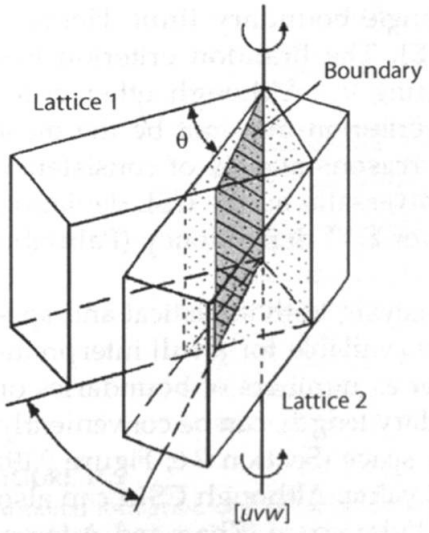

Figure A.1 Schematic of two interpenetrating lattices with misorientation angle/axis pair of *θ*/[*uvw*]. The lattice 2 is rotated around the common axis [*uvw*] by an angle of *θ*, whereas the lattice 1 is fixed. Dotted space is the interpenetrating space between the lattices after rotation where the grain boundary (GB) is located. Lattice 1 and 2 are chosen arbitrarily. A tilt GB is shown [63].

CSL arises from the fact that at certain misorientations between the interpenetrating grains, some of the lattice points will coincide and form a superlattice in three dimensions (Fig. A.2). CSLs are characterized by the Σ notation which is the reciprocal density of the lattice sites in coincidence or the volume ratio between the unit cells of superlattice and the crystal lattice. Therefore, a smaller Σ means higher number of coincidence lattice sites.

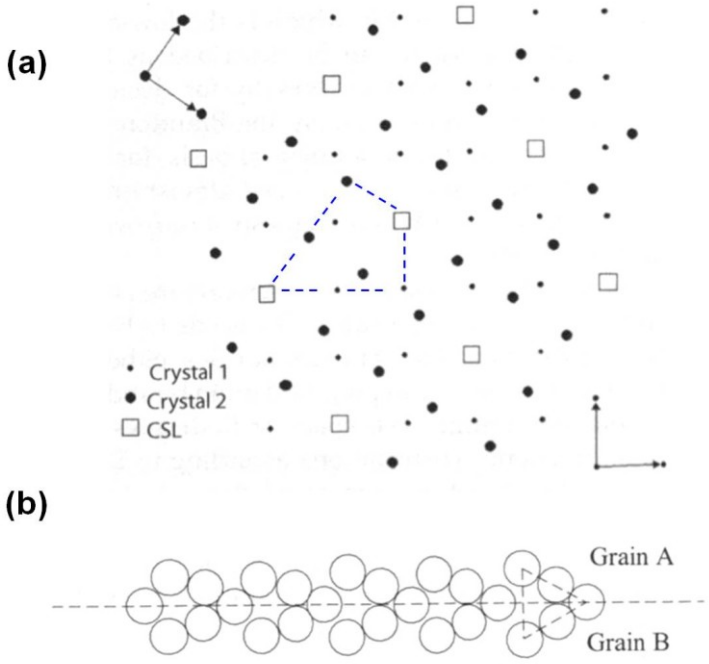

Figure A.2 Two dimensional representation of a Σ5 grain boundary (GB), i.e. 1 lattice point out of 5 is in coincidence. (a) Two interpenetrating cubic crystals with misorientation of 39.6°/<100>. After Ref. [63] (b) Coincidence of lattice points at a Σ5 GB [191].

Some of the CSL GBs might have special properties, such as in terms of their electrical properties, due to the lattice match, i.e. non-random atomic arrangement, at the GB plane. However, it should be noted here that the misorientation angle/axis scheme used commonly for identifying GBs is not related to the exact position of the GB plane within the unit cell of the crystal, and inclination of the GB plane in the interpenetrating lattice defines the exact lattice coincidence [63, 89].

REFERENCES

[1] I. Repins, M. A. Contreras, B. Egaas, C. DeHart, J. Scharf, C. L. Perkins, B. To and R. Noufi, "19·9%-efficient ZnO/CdS/CuInGaSe$_2$ solar cell with 81·2% fill factor," *Prog Photovoltaics Res Appl,* vol. 16, pp. 235-239, 2008.

[2] P. Jackson, D. Hariskos, E. Lotter, S. Paetel, R. Wuerz, R. Menner, W. Wischmann and M. Powalla, "New world record efficiency for Cu(In,Ga)Se$_2$ thin-film solar cells beyond 20%," *Prog Photovoltaics Res Appl,* vol. 19, pp. 894-897, 2011.

[3] National Renewable Energy Laboratory, "Research Cell Efficiency Records," http://www.nrel.gov/ncpv/, 2012.

[4] J. Seto, "The electrical properties of polycrystalline silicon films," *J. Appl. Phys.,* vol. 46, pp. 5247, 1975.

[5] J. Nelson, *The Physics of Solar Cells.* Imperial College Press, 2003.

[6] C. R. M. Grovenor, "Grain boundaries in semiconductors," *Journal of Physics C: Solid State Physics,* vol. 18, pp. 4079, 1985.

[7] I. Visoly-Fisher, S. R. Cohen, A. Ruzin and D. Cahen, "How Polycrystalline Devices Can Outperform Single-Crystal Ones: Thin Film CdTe/CdS Solar Cells," *Adv Mater,* vol. 16, pp. 879-883, 2004.

[8] O. Cojocaru-Mirédin, P. Choi, R. Wuerz and D. Raabe, "Atomic-scale distribution of impurities in CuInSe2-based thin-film solar cells," *Ultramicroscopy,* vol. 111, pp. 552-556, 5, 2011.

[9] O. Cojocaru-Mirédin, Pyuck-Pa Choi, D. Abou-Ras, S. S. Schmidt, R. Caballero and D. Raabe, "Characterization of Grain Boundaries in Cu(In,Ga)Se Films Using Atom-Probe Tomography," *IEEE Journal of Photovoltaics,* vol. 1, pp. 207-212, 2011.

[10] Y. Yan, C. - S. Jiang, R. Noufi, S. Wei, H. R. Moutinho and M. M. Al-Jassim, "Electrically Benign Behavior of Grain Boundaries in Polycrystalline CuInSe$_2$ Films " *Phys. Rev. Lett.,* vol. 99, pp. 235504, 2007.

[11] S. Wei, S. B. Zhang and A. Zunger, "Effects of Na on the electrical and structural properties of CuInSe$_2$," *J. Appl. Phys.,* vol. 85, pp. 7214-7218, 1999.

[12] W. N. Shafarman, S. Siebentritt and L. Stolt, "Cu(InGa)Se$_2$ solar cells," in *Handbook of Photovoltaic Science and Engineering*, Second Edition, A. Luque and S. Hegedus, Eds. Wiley, 2011, pp. 546.

[13] S. - B. Wu, A. Alphonse, C. -. Lee, K. H. Kim, K. Kim and M. H. -. Jin, "Chalcogenization of Cu/In metallic precursor thin-films using amide derivatives for chalcopyrite thin-film solar cells," in *19th International Photovoltaic Science and Engineering Conference,* Jeju, Korea.

[14] U. Rau and H. W. Schock, "Cu(In,Ga)Se_2 Solar cells," in *Clean Electricity from Photovoltaics*, M. D. Archer and R. Hill, Eds. Imperial College Press, 2001, pp. 277.

[15] I. M. Kötschau and H. W. Schock, "Compositional depth profiling of polycrystalline thin films by grazing-incidence X-ray diffraction," *Journal of Applied Crystallography (Wiley-Blackwell),* vol. 39, pp. 683-696, 10, 2006.

[16] S. Siebentritt, "What limits the efficiency of chalcopyrite solar cells?" *Solar Energy Mater. Solar Cells,* vol. 95, pp. 1471-1476, 6, 2011.

[17] W. N. Shafarman and L. Stolt, "Cu(InGa)Se_2 solar cells," in *Handbook of Photovoltaic Science and Engineering*, A. Luque and S. Hegedus, Eds. Wiley, 2003, pp. 567.

[18] H. W. Schock, "Thin film photovoltaics," *Appl. Surf. Sci.,* vol. 92, pp. 606-616, 2/2, 1996.

[19] A. Shah, P. Torres, R. Tscharner, N. Wyrsch and H. Keppner, "Photovoltaic Technology: The Case for Thin-Film Solar Cells," *Science,* vol. 285, pp. 692-698, July 30, 1999.

[20] A. Slaoui and R. T. Collins, "Advanced Inorganic Materials for Photovoltaics," *MRS Bull,* vol. 32, pp. 211, 2007.

[21] D. S. Ginley, R. Collins and D. Cahen, "Direct solar energy conversion with photovoltaic devices," in *Fundamentals of Materials for Energy and Environmental Sustainability*, D. S. Ginley and D. Cahen, Eds. Cambridge University Press, 2012, pp. 216.

[22] S. Dimitrijev, *Principles of Semiconductor Devices.* Oxford University Press, 2006.

[23] L. Solymar and D. Walsh, *Electrical Properties of Materials.* Eighth Edition, Oxford University Press, 2010.

[24] J. George, *Preparation of Thin Films.* Marcel Dekker, 1992.

[25] A. Wagendristel and Y. Wang, *An Introduction to Physics and Technology of Thin Films.* World Scientific Publishing, 1994.

[26] D. L. Smith, *Thin-Film Deposition: Principles and Practice.* McGraw-Hill, 1995.

[27] A. A. R. Elshabini-Riad and F. D. Barlow, *Thin Film Technology Handbook.* McGraw-Hill, 1998.

[28] S. Wolf and R. N. Tauber, *Silicon Processing for the VLSI Era.* Lattice Press, 1986.

[29] G. Hodes, *Chemical Solution Deposition of Semiconductor Films.* Marcel Dekker, 2003.

[30] R. S. Mane and C. D. Lokhande, "Chemical deposition method for metal chalcogenide thin films," *Mater. Chem. Phys.,* vol. 65, pp. 1-31, 6/15, 2000.

[31] M. Bouroushian, "Electrochemistry of Metal Chalcogenides," 2010.

[32] C. Voss, Y. - J. Chang, S. Subramanian, S. O. Ryu, T. - J. Lee and C. - H. Chang, "Growth Kinetics of Thin-Film Cadmium Sulfide by Ammonia-Thiourea Based CBD," *J. Electrochem. Soc.,* vol. 151, pp. C655-C660, 2004.

[33] T. P. Niesen and M. R. De Guire, "Review: Deposition of Ceramic Thin Films at Low Temperatures from Aqueous Solutions," *Journal of Electroceramics,* vol. 6, pp. 169-207, 2001.

[34] C. Guillén, M. A. Martínez and J. Herrero, "Accurate control of thin film CdS growth process by adjusting the chemical bath deposition parameters," *Thin Solid Films,* vol. 335, pp. 37-42, 11/19, 1998.

[35] R. Bhattacharya, "Chemical bath deposition, electrodeposition, and electroless deposition of semiconductors, superconductors, and oxide materials," in *Solution Processing of Inorganic Materials*, D. B. Mitzi, Ed. John Wiley & Sons, Inc, 2009, pp. 199.

[36] O. Savadogo, "Chemically and electrochemically deposited thin films for solar energy materials," *Solar Energy Mater. Solar Cells,* vol. 52, pp. 361-388, 4/30, 1998.

[37] P. Capper, "Bulk crystal growth - methods and materials," in *Springer Handbook of Electronic and Photonic Materials*, S. Kasap and P. Capper, Eds. Springer, 2006, pp. 231.

[38] M. Isshiki and J. F. Wang, "Bulk crystal growth of wide-bandgap II-VI materials," in *Bulk Crystal Growth of Electronic, Optical and Optoelectronic Materials*, P. Capper, Ed. John Wiley & Sons, Ltd, 2005, pp. 269.

[39] Lord Kelvin, "Contact electricity of metals," *Philosophical Magazine,* vol. 46, pp. 82, 1898.

[40] S. Sadewasser, "Experimental technique and working modes," in *Kelvin Probe Force Microscopy: Measuring and Compensating Electrostatic Forces*, S. Sadewasser and T. Glatzel, Eds. Springer, 2012, pp. 7.

[41] W. Melitz, J. Shen, A. C. Kummel and S. Lee, "Kelvin probe force microscopy and its application," *Surface Science Reports,* vol. 66, pp. 1-27, 1, 2011.

[42] G. Binnig, C. F. Quate and C. Gerber, "Atomic Force Microscope," *Phys. Rev. Lett.,* vol. 56, pp. 930-933, 03/03, 1986.

[43] G. Binnig, H. Rohrer, C. Gerber and E. Weibel, "Surface Studies by Scanning Tunneling Microscopy," *Phys. Rev. Lett.,* vol. 49, pp. 57-61, 07/05, 1982.

[44] D. K. Schroder, *Semiconductor Material and Device Characterization.* Third Edition, John Wiley & Sons, Inc., 2006.

[45] B. Such, F. Krok and M. Szymonski, "Scanning force microscopies for imaging and characterization of nanostructured materials," in *Nanotechnology for Electronic Materials and Devices*, A. Korkin, J. Labanowski, E. Gusev and S. Luryi, Eds. Springer, 2007, pp. 223.

[46] Y. Leng, *Materials Characterization: Introduction to Microscopic and Spectroscopic Methods.* John Wiley & Sons (Asia) Pte Ltd, 2008.

[47] D. A. Bonnell and B. D. Huey, "Basic principles of scanning probe microscopy," in *Scanning Probe Microscopy and Spectroscopy: Theory, Techniques, and Applications*, Second ed., D. A. Bonnell, Ed. Wiley-VCH, 2001, pp. 7.

[48] T. Mikayama, "AFM," in *Nanoparticle Technology Handbook*, M. Hosokawa, K. Nogi, M. Naito and T. Yokoyama, Eds. Elsevier, 2007, pp. 279.

[49] D. Ricci and P. C. Braga, "Imaging methods in atomic froce microscopy," in *Atomic Froce Microscopy: Biomedical Methods and Applications*, P. C. Braga and D. Ricci, Eds. Humana Press, 2004, pp. 13.

[50] Park Systems, "XE-70 User's Manual," 2007.

[51] M. Nonnenmacher, M. P. O'Boyle and H. K. Wickramasinghe, "Kelvin probe force microscopy," *Appl. Phys. Lett.,* vol. 58, pp. 2921-2923, June 24, 1991, 1991.

[52] T. Glatzel, M. C. Lux-Steiner, E. Strassburg, A. Boag and Y. Rosenwaks, "Principles of kelvin probe force microscopy," in *Scanning Probe Microscopy: Electrical and Electromechanical Phenomena at the Nanoscale Vol 2*, S. Kalinin and A. Gruverman, Eds. Springer, 2007, pp. 113.

[53] Park Systems, "EFM: Electrostatic Force Microscopy for XE Series SPM: Operating Manual," 2004.

[54] H. D. Young, R. A. Freedman, T. R. Sandin and A. L. Ford, *Sears and Zemansky's University Physics.* Addison Wesley Longman, Inc., 2000.

[55] C. - S. Jiang, "Microscopic electrical characterization of inorganic semiconductor-based solar cell materials and devices using AFM-based techniques," in *Scanning Probe Microscopy in Nanoscience and Nanotechology*, B. Bhushan, Ed. Springer, 2011, pp. 723.

[56] V. Palermo, M. Palma and P. Samorì, "Electronic Characterization of Organic Thin Films by Kelvin Probe Force Microscopy," *Adv Mater,* vol. 18, pp. 145-164, 2006.

[57] U. Zerweck, C. Loppacher, T. Otto, S. Grafström and L. M. Eng, "Accuracy and resolution limits of Kelvin probe force microscopy," *Phys. Rev. B,* vol. 71, pp. 125424, 03/25, 2005.

[58] T. Glatzel, S. Sadewasser and M. C. Lux-Steiner, "Amplitude or frequency modulation-detection in Kelvin probe force microscopy," *Appl. Surf. Sci.,* vol. 210, pp. 84-89, 3/31, 2003.

[59] V. Randle, "Electron backscatter diffraction: Strategies for reliable data acquisition and processing," *Mater Charact,* vol. 60, pp. 913-922, 9, 2009.

[60] R. A. Schwarzer, D. P. Field, B. L. Adams, M. Kumar and A. J. Schwartz, "Present state of electron backscatter diffraction and prospective developments," in *Electron Backscatter Diffraction in Materials Science*, Second ed., A. J. Schwartz, M. Kumar, B. L. Adams and D. P. Field, Eds. Springer, 2009, pp. 1.

[61] D. J. Dingley and D. P. Field, "Electron backscatter diffraction and orientation imaging microscopy," *Materials Science and Technology,* vol. 13, pp. 69, 1997.

[62] D. J. Dingley and V. Randle, "Microtexture determination by electron back-scatter diffraction," *Journal of Materials Science,* vol. 27, pp. 4545-4566, 1992.

[63] O. Engler and V. Randle, *Introduction to Texture Analysis: Macrotexture, Microtexture, and Orientation Mapping.* CRC Press, 2010.

[64] J. R. Michael, "Characterization of nano-crystalline materials using electron backscatter diffaction in the scanning electron microscope," in *Handbook of Microscopy for Nanotechnology*, N. Yao and Z. L. Wang, Eds. Kluwer Academic Publishers, 2005, pp. 401.

[65] H. Moutinho, R. Dhere, C. Jiang, B. To and M. Al-Jassim, "Electron-Backscatter Diffraction of Photovoltaic Thin Films," *MRS Online Proceedings Library,* vol. 1012, 2007.

[66] T. Maitland and S. Sitzman, "Electron backscatter diffraction (EBSD) technique and materials characterization examples," in *Scanning Microscopy for Nanotechnology: Techniques and Applications*, W. Zhou and Z. L. Wang, Eds. Springer, 2006, pp. 41.

[67] D. Abou-Ras, R. Caballero, J. Kavalakkatt, M. Nichterwitz, T. Unold, H. -. Schock, S. Bucheler and A. N. Tiwari, "Electron backscatter diffraction: Exploring the microstructure in cu(in,ga)(S,se)2 and CdTe thin-film solar cells," in *35th IEEE Photovoltaic Specialists Conference (PVSC),* 2010, pp. 000418-000423.

[68] D. B. Williams and C. B. Carter, *Transmission Electron Microscopy: A Textbook for Materials Science.* Springer, 2009.

[69] D. Brandon and W. D. Kaplan, *Microstructural Characterization of Materials.* John Wiley & Sons Ltd, 2008.

[70] D. Abou-Ras, J. Dietrich, J. Kavalakkatt, M. Nichterwitz, S. S. Schmidt, C. T. Koch, R. Caballero, J. Klaer and T. Rissom, "Analysis of Cu(In,Ga)(S,Se)2 thin-film solar cells by means of electron microscopy," *Solar Energy Mater. Solar Cells,* vol. 95, pp. 1452-1462, 6, 2011.

[71] G. Salviati, F. Rossi, N. Armani, V. Grillo and L. Lazzarini, "Power-dependent cathodoluminescence in III-nitrides heterostructures: From internal field screening to controlled band-gap modulation," in *Characterization of Semiconductor Heterostructures and Nanostructures*, First ed., C. Lamberti, Ed. Elsevier, 2008, pp. 209.

[72] B. G. Yacobi, "CL: Cathodoluminescence," in *Encyclopedia of Materials Characterization: Surfaces, Interfaces, Thin Films*, C. R. Brundle, C. A. Evans and S. Wilson, Eds. Butterworth-Heinemann, 1992, pp. 149.

[73] D. B. Holt and B. G. Yacobi, *Extended Defects in Semiconductors: Electronic Properties, Device Effects and Structures.* Cambridge University Press, 2007.

[74] B. G. Yacobi and D. B. Holt, "Cathodoluminescence scanning electron microscopy of semiconductors," *J. Appl. Phys.,* vol. 59, pp. R1-R24, 1986.

[75] M. Fox, *Optical Properties of Solids.* Oxford University Press, 2001.

[76] A. K. Arora, "Raman spectroscopic characterization of nanostructured materials," in *Perspectives in Materials Characterization*, G. Amarendra, B. Raj and M. H. Manghnani, Eds. CRC Press, 2009, pp. 23.

[77] R. W. Cahn, Ed., *Concise Encyclopedia of Materials Characterization.* Elsevier, 2005.

[78] W. B. White, "Raman spectroscopy," in *Encyclopedia of Materials Characterization: Surfaces, Interfaces, Thin Films*, C. R. Brundle, C. A. Evans and S. Wilson, Eds. Butterworth-Heinemann, 1992, pp. 428.

[79] P. E. J. Flewitt and R. K. Wild, *Physical Methods for Materials Characterisation.* IOP Publishing, 2003.

[80] C. W. Brown, "Ultraviolet, visible, and near-infrared spectrophotometers," in *Analytical Instrumentation Handbook*, Second Edition, G. W. Ewing, Ed. Marcel Dekker, 1997, pp. 327.

[81] H. Okamura, "Methods for obtaining the optical constants of a material," in *Optical Techniques for Solid-State Materials Characterization*, R. P. Prasankumar and A. J. Taylor, Eds. CRC Press, 2012, pp. 111.

[82] H. - H. Perkampus, *Encyclopedia of Spectroscopy.* VCH, 1995.

[83] P. N. Gibson, "Grazing incidence X-ray methods for near-surface structural studies," in *Surface and Thin Film Analysis: A Compendium of Principles, Instrumentation, and Applications*, H. Bubert and H. Jenett, Eds. Wiley-VCH, 2002, pp. 208.

[84] B. E. McCandless, "Glancing Incidence X-Ray Diffraction of Polycrystalline Thin Films," *MRS Online Proceedings Library,* vol. 865, 2005.

[85] L. S. Yip and I. Shih, "Photovoltaic cells with efficiency exceeding 10% using monocrystalline $CuInSe_2$ substrates," in *Conference Record of the Twenty Fourth IEEE Photovoltaic Specialists Conference, IEEE First World Conference on Photovoltaic Energy Conversion,* 1994, pp. 210-213 vol.1.

[86] J. E. Granata, J. R. Sites, S. Asher and R. J. Matson, "Quantitative incorporation of sodium in $CuInSe_2$ and $Cu(In,Ga)Se_2$ photovoltaic devices," in *Photovoltaic Specialists Conference, Conference Record of the Twenty-Sixth IEEE,* 1997, pp. 387-390.

[87] D. Abou-Ras, S. Schorr and H. W. Schock, "Grain-size distributions and grain boundaries of chalcopyrite-type thin films," *Journal of Applied Crystallography,* vol. 40, pp. 841-848, 2007.

[88] N. I. Medvedeva, E. V. Shalaeva, M. V. Kuznetsov and M. V. Yakushev, "First-principles study of deformation behavior and structural defects in $CuInSe_2$ and $Cu(In,Ga)Se_2$," *Phys. Rev. B,* vol. 73, pp. 035207, 01/11, 2006.

[89] V. Randle, *The Measurement of Grain Boundary Geometry.* IOP Publishing, 1993.

[90] C. Persson and A. Zunger, "Anomalous Grain Boundary Physics in Polycrystalline $CuInSe_2$: The Existence of a Hole Barrier " *Phys. Rev. Lett.,* vol. 91, pp. 266401, 2003.

[91] C. Persson, "Compositionally induced valence-band offset at the grain boundary of polycrystalline chalcopyrites creates a hole barrier," *Appl. Phys. Lett.,* vol. 87, pp. 211904-3, 2005.

[92] S. M. Sze and K. K. Ng, *Physics of Semiconductor Devices.* Wiley-Interscience, 2006.

[93] A. L. Fahrenbruch and R. H. Bube, *Fundamentals of Solar Cells.* Academic Press, 1983.

[94] U. Rau, K. Taretto and S. Siebentritt, "Grain boundaries in $Cu(In, Ga)(Se, S)_2$ thin-film solar cells," *Appl. Phys. A,* vol. 96, pp. 221-234, 2009.

[95] S. Siebentritt, M. Igalson, C. Persson and S. Lany, "The electronic structure of chalcopyrites-bands, point defects and grain boundaries," *Prog Photovoltaics Res Appl,* vol. 18, pp. 390-410, 2010.

[96] C. - S. Jiang, R. Noufi, K. Ramanathan, J. A. AbuShama, H. R. Moutinho and M. M. Al-Jassim, "Does the local built-in potential on grain boundaries of $Cu(In,Ga)Se_2$ thin films benefit photovoltaic performance of the device?" *Appl. Phys. Lett.,* vol. 85, pp. 2625-2627, 2004.

[97] G. Hanna, T. Glatzel, S. Sadewasser, N. Ott, H. P. Strunk, U. Rau and J. H. Werner, "Texture and electronic activity of grain boundaries in $Cu(In,Ga)Se_2$ thin films," *Appl. Phys. A,* vol. 82, pp. 1-7, 2006.

[98] M. Kawamura, T. Yamada, N. Suyama, A. Yamada and M. Konagai, "Grain Boundary Evaluation of $Cu(In_{1-x}Ga_x)Se_2$ Solar Cells," *Japanese Journal of Applied Physics,* vol. 49, pp. 062301, 2010.

[99] M. J. Romero, C. - S. Jiang, R. Noufi and M. Al-Jassim, "Photon emission in $CuInSe_2$ thin films observed by scanning tunneling microscopy," *Appl. Phys. Lett.,* vol. 86, pp. 143115, 2005.

[100] M. J. Hetzer, Y. M. Strzhemechny, M. Gao, M. A. Contreras, A. Zunger and L. J. Brillson, "Direct observation of copper depletion and potential changes at copper indium gallium diselenide grain boundaries," *Appl. Phys. Lett.,* vol. 86, pp. 162105, 2005.

[101] C. Lei, C. M. Li, A. Rockett and I. M. Robertson, "Grain boundary compositions in $Cu(InGa)Se_2$," *J. Appl. Phys.,* vol. 101, pp. 024909, 2007.

[102] Y. Yan, R. Noufi and M. M. Al-Jassim, "Grain-Boundary Physics in Polycrystalline $CuInSe_2$ Revisited: Experiment and Theory," *Phys. Rev. Lett.,* vol. 96, pp. 205501, 2006.

[103] S. Siebentritt, S. Sadewasser, M. Wimmer, C. Leendertz, T. Eisenbarth and M. C. Lux-Steiner, "Evidence for a Neutral Grain-Boundary Barrier in Chalcopyrites," *Phys. Rev. Lett.,* vol. 97, pp. 146601, 2006.

[104] M. Hafemeister, S. Siebentritt, J. Albert, M. C. Lux-Steiner and S. Sadewasser, "Large Neutral Barrier at Grain Boundaries in Chalcopyrite Thin Films," *Phys. Rev. Lett.,* vol. 104, pp. 196602, 2010.

[105] M. Hafemeister, S. Siebentritt, S. Sadewasser, C. Frank-Rotsch and M. C. Lux-Steiner, "A neutral barrier at CGS grain boundaries - compositional and structural dependencies," in *MRS Proceedings,* San Francisco, California, USA, 2007, pp. 1012-Y09-04.

[106] R. Scheer and H. W. Schock, *Chalcogenide Photovoltaics: Physics, Technologies, and Thin Film Devices.* Wiley, 2011.

[107] J. Hedstrom, H. Ohlsen, M. Bodegard, A. Kylner, L. Stolt, D. Hariskos, M. Ruckh and H. -. Schock, "ZnO/CdS/Cu(In,Ga)Se_2 thin film solar cells with improved performance," in *Conference Record of the Twenty Third IEEE Photovoltaic Specialists Conference,* 1993, pp. 364-371.

[108] M. Bodeg Ård, K. Granath and L. Stolt, "Growth of Cu(In,Ga)Se_2 thin films by coevaporation using alkaline precursors," *Thin Solid Films,* vol. 361-362, pp. 9-16, 2/21, 2000.

[109] V. Probst, J. Rimmasch, W. Riedl, W. Stetter, J. Holz, H. Harms, F. Karg and H. W. Schock, "The impact of controlled sodium incorporation on rapid thermal processed Cu(InGa)Se_2-thin films and devices," in *Conference Record of the Twenty Fourth IEEE Photovoltaic Specialists Conference, IEEE First World Conference on Photovoltaic Energy Conversion,* 1994, pp. 144-147 vol.1.

[110] M. Bodegård, L. Stolt and J. Hedström, "The influence of sodium on the grain structure of $CuInSe_2$ films for photovoltaic applications," in *12th European Photovoltaic Solar Energy Conference* Amsterdam, The Netherlands, 1994, pp. 1743.

[111] D. Rudmann, A. F. da Cunha, M. Kaelin, F. Kurdesau, H. Zogg, A. N. Tiwari and G. Bilger, "Efficiency enhancement of Cu(In,Ga)Se_2 solar cells due to post-deposition Na incorporation," *Appl. Phys. Lett.,* vol. 84, pp. 1129-1131, 2004.

[112] U. Rau, M. Schmitt, D. Hilburger, F. Engelhardt, O. Seifert, J. Parisi, W. Riedl, J. Rimmasch and F. Karg, "Influence of Na and S incorporation on the electronic transport properties of Cu(In,Ga)Se_2 solar cells," in *Conference Record of the Twenty Fifth IEEE Photovoltaic Specialists Conference,* 1996, pp. 1005-1008.

[113] H. Ruckh, D. Schmid, M. Kaiser, R. Schaffler, T. Walter and H. W. Schock, "Influence of substrates on the electrical properties of Cu(In,Ga)Se_2 thin films," in *Conference Record of the Twenty Fourth IEEE Photovoltaic Specialists Conference, IEEE First World Conference on Photovoltaic Energy Conversion,* 1994, pp. 156-159 vol.1.

[114] D. W. Niles, K. Ramanathan, F. Hasoon, R. Noufi, B. J. Tielsch and J. E. Fulghum, "Na impurity chemistry in photovoltaic CIGS thin films: Investigation with x-ray photoelectron spectroscopy," *J. Vac. Sci. Technol. A,* vol. 15, pp. 3044-3049, 1997.

[115] D. W. Niles, M. Al-Jassim and K. Ramanathan, "Direct observation of Na and O impurities at grain surfaces of $CuInSe_2$ thin films," *J. Vac. Sci. Technol. A,* vol. 17, pp. 291-296, 1999.

[116] E. Cadel, N. Barreau, J. Kessler and P. Pareige, "Atom probe study of sodium distribution in polycrystalline $Cu(In,Ga)Se_2$ thin film," *Acta Materialia,* vol. 58, pp. 2634-2637, 4, 2010.

[117] C. H. Champness, H. F. Myers and I. Shih, "Carrier polarity reversal with sodium addition in Bridgman-grown CuInSe2," *Thin Solid Films,* vol. 519, pp. 7337-7340, 8/31, 2011.

[118] V. Lyahovitskaya, Y. Feldman, K. Gartsman, H. Cohen, C. Cytermann and D. Cahen, "Na effects on CuInSe[sub 2]: Distinguishing bulk from surface phenomena," *J. Appl. Phys.,* vol. 91, pp. 4205-4212, April 1, 2002, 2002.

[119] F. Couzinie-Devy, E. Cadel, N. Barreau, P. Pareige and J. Kessler, "Atom probe contribution to the Characterisation of CIGSe grain boundaries," in *37th IEEE Photovoltaic Specialists Conference (PVSC),* 2011, pp. 001966-001971.

[120] D. Fuertes Marrón, S. Sadewasser, A. Meeder, T. Glatzel and M. C. Lux-Steiner, "Electrical activity at grain boundaries of $Cu(In,Ga)Se_2$ thin films," *Phys. Rev. B,* vol. 71, pp. 033306, 01/06, 2005.

[121] R. Baier, D. Abou-Ras, T. Rissom, M. C. Lux-Steiner and S. Sadewasser, "Symmetry-dependence of electronic grain boundary properties in polycrystalline $CuInSe_2$ thin films," *Appl. Phys. Lett.,* vol. 99, pp. 172102, 2011.

[122] H. F. Myers, "Electrical Influence of Sodium in Bridgman-grown $CuInSe_2$," Dissertation, McGill University, 2012.

[123] B. Beausir and J. J. Fundenberger, "EBSDmcf," version 6.0, 2011.

[124] ResMat Co., "HTexTools," version 3.3, 2000.

[125] S. V. Kalinin, "Nanoscale electric phenomena at oxide surfaces and interfaces by scanning probe microscopy," Dissertation, University of Pennsylvania, 2002.

[126] Y. Lu, M. Muñoz, C. S. Steplecaru, C. Hao, M. Bai, N. Garcia, K. Schindler and P. Esquinazi, "Electrostatic Force Microscopy on Oriented Graphite Surfaces: Coexistence of Insulating and Conducting Behaviors," *Phys. Rev. Lett.,* vol. 97, pp. 076805, 08/18, 2006.

[127] M. J. Romero, K. Ramanathan, M. A. Contreras, M. M. Al-Jassim, R. Noufi and P. Sheldon, "Cathodoluminescence of $Cu(In,Ga)Se_2$ thin films used in high-efficiency solar cells," *Appl. Phys. Lett.,* vol. 83, pp. 4770-4772, 2003.

[128] D. Abou-Ras and K. Pantleon, "The impact of twinning on the local texture of chalcopyrite-type thin films," *Physica Status Solidi (RRL)-Rapid Research Letters,* vol. 1, pp. 187-189, 2007.

[129] S. Sadewasser, T. Glatzel, M. Rusu, A. Jager-Waldau and M. C. Lux-Steiner, "High-resolution work function imaging of single grains of semiconductor surfaces," *Appl. Phys. Lett.,* vol. 80, pp. 2979-2981, 2002.

[130] M. J. Romero, H. Du, G. Teeter, Y. Yan and M. Al-Jassim, "Comparative study of the luminescence and intrinsic point defects in the kesterite Cu_2ZnSnS_4 and chalcopyrite $Cu(In,Ga)Se_2$ thin films used in photovoltaic applications," *Phys. Rev. B,* vol. 84, pp. 165324, 10/24, 2011.

[131] G. Rohrer, "Grain boundary energy anisotropy: a review," *Journal of Materials Science,* vol. 46, pp. 5881-5895, 2011.

[132] L. K. Fionova and A. V. Artemyev, *Grain Boundaries in Metals and Semiconductors.* Les Editions de Physique, 1993.

[133] D. A. Porter and K. E. Easterling, *Phase Transformations in Metals and Alloys.* CRC Press, 1992.

[134] F. M.L., "The phase relations in the Cu,In,Se system and the growth of $CuInSe_2$ single crystals," *Solar Cells,* vol. 16, pp. 91-100, 2, 1986.

[135] K. L. Chopra, P. D. Paulson and V. Dutta, "Thin-film solar cells: an overview," *Prog Photovoltaics Res Appl,* vol. 12, pp. 69-92, 2004.

[136] J. A. M. AbuShama, S. Johnston, T. Moriarty, G. Teeter, K. Ramanathan and R. Noufi, "Properties of ZnO/CdS/$CuInSe_2$ solar cells with improved performance," *Prog Photovoltaics Res Appl,* vol. 12, pp. 39-45, 2004.

[137] C. J. Hibberd, E. Chassaing, W. Liu, D. B. Mitzi, D. Lincot and A. N. Tiwari, "Non-vacuum methods for formation of $Cu(In,Ga)(Se,S)_2$ thin film photovoltaic absorbers," *Prog Photovoltaics Res Appl,* vol. 18, pp. 434-452, 2010.

[138] P. Jackson, R. Würz, U. Rau, J. Mattheis, M. Kurth, T. Schlötzer, G. Bilger and J. H. Werner, "High quality baseline for high efficiency, $Cu(In_{1-x},Ga_x)Se_2$ solar cells," *Prog Photovoltaics Res Appl,* vol. 15, pp. 507-519, 2007.

[139] F. Karg, V. Probst, H. Harms, J. Rimmasch, W. Riedl, J. Kotschy, J. Holt, R. Treichler, O. Eibl, A. Mitwalsky and A. Kiendl, "Novel rapid-thermal-processing for CIS thin-film solar cells," in *Conference Record of the Twenty Third IEEE Photovoltaic Specialists Conference,* 1993, pp. 441-446.

[140] I. M. Kötschau, A. Kampmann, T. Hahn, J. Hinze, O. Pursche, S. Gorse and E. Richter, "Systematic design of an annealing process for $Cu(In,Ga)Se_2$ layer formation by in-situ XRD: A case study," in *25th European Photovoltaic Solar Energy Conference and Exhibition / 5th World Conference on Photovoltaic Energy Conversion,* Valencia, Spain, 2010, pp. 3533.

[141] F. O. Adurodija, J. Song, S. D. Kim, S. H. Kwon, S. K. Kim, K. H. Yoon and B. T. Ahn, "Growth of $CuInSe_2$ thin films by high vapour Se treatment of co-sputtered Cu-In alloy in a graphite container," *Thin Solid Films,* vol. 338, pp. 13-19, 1/11, 1999.

[142] J. Fang, D. Perng and J. Chen, "Mechanism of forming (2 2 0/2 0 4)-oriented $CuInSe_2$ film on Al:ZnO substrate using a two-step selenization process," *J. Cryst. Growth,* vol. 321, pp. 106-112, 4/15, 2011.

[143] N. Orbey, H. Hichri, R. W. Birkmire and T. W. F. Russell, "Effect of temperature on copper indium selenization," *Prog Photovoltaics Res Appl,* vol. 5, pp. 237-247, 1997.

[144] R. Kamada, W. N. Shafarman and R. W. Birkmire, "Cu(In,Ga)Se_2 film formation from selenization of mixed metal/metal–selenide precursors," *Solar Energy Mater. Solar Cells,* vol. 94, pp. 451-456, 3, 2010.

[145] T. Yamamoto, M. Nakamura, J. Ishizuki, T. Deguchi, S. Ando, H. Nakanishi and S. Chichibu, "Use of diethylselenide as a less-hazardous source for preparation of $CuInSe_2$ thin films by selenization of metal precursors," *Journal of Physics and Chemistry of Solids,* vol. 64, pp. 1855-1858, 9, 2003.

[146] A. A. Kadam and N. G. Dhere, "Highly efficient $CuIn_{1-x}Ga_xSe_{2-y}S_y$/CdS thin-film solar cells by using diethylselenide as selenium precursor," *Solar Energy Mater. Solar Cells,* vol. 94, pp. 738-743, 5, 2010.

[147] S. Verma, R. D. Varrin Jr., R. W. Birkmire and T. W. F. Russel, "Critical process issues in selenization," in *Conference Record of the Twenty Second IEEE Photovoltaic Specialists Conference,* 1991, pp. 914-919 vol.2.

[148] S. Niki, M. Contreras, I. Repins, M. Powalla, K. Kushiya, S. Ishizuka and K. Matsubara, "CIGS absorbers and processes," *Prog Photovoltaics Res Appl,* vol. 18, pp. 453-466, 2010.

[149] S. Verma, T. W. F. Russell and R. W. Birkmire, "The effect of O_2 on H_2Se selenization in a continuous flow reactor," in *Conference Record of the Twenty Third IEEE Photovoltaic Specialists Conference,* 1993, pp. 431-436.

[150] D. Albin, J. Carapella, A. Gabor, A. Tennant, J. Tuttle, A. Duda, R. Matson, A. Mason, M. Contreras and R. Noufi, "Fundamental thermodynamics and experiments in fabricating high efficiency $CuInSe_2$ solar cells by selenization without the use of H_2Se," *AIP Conf. Proc.,* vol. 268, pp. 108-121, 1992.

[151] K. Geisler, A. Jacobs, A. Kuenzler, M. Mathes, I. Girrleit, B. Zimmermann, E. Bulka, W. Pfeiffer and P. Langer, "Efficient Synthesis of Primary Selenocarboxylic Amides by Reaction of Nitriles with Phosphorous(V) Selenide," *Synlett,* vol. 2002, pp. 1983, 2002.

[152] A. Z. Al-Rubaie, L. Z. Yousif and A. J. H. Al-Hamad, "Palladium-catalyzed formation of 3,5-diaryl-1,2,4-selenadiazoles from arylselenocarboxamide," *Journal of Organometallic Chemistry,* vol. 656, pp. 274-280, 8/15, 2002.

[153] G. Hua, Y. Li, A. M. Z. Slawin and J. D. Woollins, "Synthesis of Primary Arylselenoamides by Reaction of Aryl Nitriles with Woollins' Reagent," *Org. Lett.,* vol. 8, pp. 5251-5254, 11/01; 2012/02, 2006.

[154] A. Alphonse, "Thioacetamide as a Sulfur Precursor for Chalcopyrite Thin Film Solar Cells," Master's Thesis, University of Texas at Arlington, 2009.

[155] T. Murai, "Thio-, Seleno-, Telluro-Amides," *Topics in Current Chemistry,* vol. 251, pp. 247, 2005.

[156] V. Alberts and R. Swanepoel, "Structural analysis of $CuInSe_2$ thin films prepared by selenization of Cu-In films," *Journal of Materials Science: Materials in Electronics,* vol. 7, pp. 91-99, 1996.

[157] D. S. Albin, G. D. Mooney, J. Carapella, A. Duda, J. Tuttle, R. Matson and R. Noufi, "The phase behavior of evaporated copper and indium precursors for selenization," *Solar Cells,* vol. 30, pp. 41-46, 5, 1991.

[158] C. von Klopmann, J. Djordjevic and R. Scheer, "Real-time studies of phase transformations in Cu–In–Se–S thin films: 1. Intermetallic phase transformations," *J. Cryst. Growth,* vol. 289, pp. 113-120, 3/15, 2006.

[159] J. Djordjevic, E. Rudigier and R. Scheer, "Real-time studies of phase transformations in Cu–In–Se–S thin films—3: Selenization of Cu–In precursors," *J. Cryst. Growth,* vol. 294, pp. 218-230, 9/4, 2006.

[160] H. Okamoto, "Cu-In (copper-indium)," *Journal of Phase Equilibria and Diffusion,* vol. 26, pp. 645-645, 2005.

[161] A. Brummer, V. Honkimäki, P. Berwian, V. Probst, J. Palm and R. Hock, "Formation of $CuInSe_2$ by the annealing of stacked elemental layers—analysis by in situ high-energy powder diffraction," *Thin Solid Films,* vol. 437, pp. 297-307, 8/1, 2003.

[162] S. Verma, N. Orbey, R. W. Birkmire and T. W. F. Russell, "Chemical reaction analysis of copper indium selenization," *Prog Photovoltaics Res Appl,* vol. 4, pp. 341-353, 1996.

[163] J. R. Tuttle, M. Contreras, M. H. Bode, D. Niles, D. S. Albin, R. Matson, A. M. Gabor, A. Tennant, A. Duda and R. Noufi, "Structure, chemistry, and growth mechanisms of photovoltaic quality thin-film $Cu(In,Ga)Se_2$ grown from a mixed-phase precursor," *J. Appl. Phys.,* vol. 77, pp. 153-161, 1995.

[164] S. Kim, W. K. Kim, R. M. Kaczynski, R. D. Acher, S. Yoon, T. J. Anderson, O. D. Crisalle, E. A. Payzant and S. S. Li, "Reaction kinetics of $CuInSe_2$ thin films grown from bilayer InSe/CuSe precursors," *J. Vac. Sci. Technol. A,* vol. 23, pp. 310-315, 2005.

[165] W. K. Kim, S. Kim, E. A. Payzant, S. A. Speakman, S. Yoon, R. M. Kaczynski, R. D. Acher, T. J. Anderson, O. D. Crisalle, S. S. Li and V. Craciun, "Reaction kinetics of α-$CuInSe_2$ formation from an In2Se3/CuSe bilayer precursor film," *Journal of Physics and Chemistry of Solids,* vol. 66, pp. 1915-1919, 11, 2005.

[166] W. K. Kim, E. A. Payzant, S. Yoon and T. J. Anderson, "In situ investigation on selenization kinetics of Cu–In precursor using time-resolved, high temperature X-ray diffraction," *J. Cryst. Growth,* vol. 294, pp. 231-235, 9/4, 2006.

[167] M. Marudachalam, R. W. Birkmire, H. Hichri, J. M. Schultz, A. Swartzlander and M. M. Al-Jassim, "Phases, morphology, and diffusion in $CuIn_xGa_{1-x}Se_2$ thin films," *J. Appl. Phys.,* vol. 82, pp. 2896-2905, 1997.

[168] B. M. Basol, V. K. Kapur, A. Halani, C. R. Leidholm, J. Sharp, J. R. Sites, A. Swartzlander, R. Matson and H. Ullal, "Cu (In,Ga)Se_2 thin films and solar cells prepared by selenization of metallic precursors," *J. Vac. Sci. Technol. A,* vol. 14, pp. 2251-2256, 1996.

[169] K. Kushiya, A. Shimizu, A. Yamada and M. Konagai, "Development of High-Efficiency $CuIn_xGa_{1-x}Se_2$ Thin-Film Solar Cells by Selenization with Elemental Se Vapor in Vacuum," *Jpn. J. Appl. Phys.,* vol. 34, pp. 54, 1995.

[170] M. Marudachalam, H. Hichri, R. Klenk, R. W. Birkmire, W. N. Shafarman and J. M. Schultz, "Preparation of homogeneous Cu(InGa)Se_2 films by selenization of metal precursors in H_2Se atmosphere," *Appl. Phys. Lett.,* vol. 67, pp. 3978-3980, 1995.

[171] R. Krishnan, W. K. Kim, E. A. Payzant, Y. Sohn, B. Yao and T. J. Anderson, "Synthesis of CIGS absorber layers from bilayer metal precursors," in *37th IEEE Photovoltaic Specialists Conference (PVSC),* 2011, pp. 000393-000395.

[172] T. Wada, N. Kohara, S. Nishiwaki and T. Negami, "Characterization of the Cu(In,Ga)Se_2/Mo interface in CIGS solar cells," *Thin Solid Films,* vol. 387, pp. 118-122, 5/29, 2001.

[173] S. Wei, S. B. Zhang and A. Zunger, "Effects of Ga addition to $CuInSe_2$ on its electronic, structural, and defect properties," *Appl. Phys. Lett.,* vol. 72, pp. 3199-3201, 1998.

[174] M. A. Contreras, J. Tuttle, A. Gabor, A. Tennant, K. Ramanathan, S. Asher, A. Franz, J. Keane, L. Wang and R. Noufi, "High efficiency graded bandgap thin-film polycrystalline Cu(In,Ga)Se_2-based solar cells," *Solar Energy Mater. Solar Cells,* vol. 41–42, pp. 231-246, 6, 1996.

[175] J. Herrero, M. T. Gutiérrez, C. Guillén, J. M. Doña, M. A. Martínez, A. M. Chaparro and R. Bayón, "Photovoltaic windows by chemical bath deposition," *Thin Solid Films,* vol. 361–362, pp. 28-33, 2/21, 2000.

[176] I. Kaur, D. K. Pandya and K. L. Chopra, "Growth Kinetics and Polymorphism of Chemically Deposited CdS Films," *J. Electrochem. Soc.,* vol. 127, pp. 943-948, 1980.

[177] M. Kim, B. Min, C. Kim, S. Lee, H. T. Kim, S. K. Jung and S. Sohn, "Study of the physical property of the cadmium sulfide thin film depending on the process condition," *Current Applied Physics,* vol. 10, pp. S455-S458, 5, 2010.

[178] K. Wilchelmi, D. Förster, A. Neisser and R. Schomäcker, "Kinetic Studies of CdS Formation for a Better Understanding of Chemical Buffer Layer Deposition," *MRS Online Proceedings Library,* vol. 1165, 2009.

[179] R. Ortega-Borges and D. Lincot, "Mechanism of Chemical Bath Deposition of Cadmium Sulfide Thin Films in the Ammonia-Thiourea System," *J. Electrochem. Soc.,* vol. 140, pp. 3464-3473, 1993.

[180] J. M. Dona and J. Herrero, "Chemical Bath Deposition of CdS Thin Films: An Approach to the Chemical Mechanism Through Study of the Film Microstructure," *J. Electrochem. Soc.,* vol. 144, pp. 4081-4091, 1997.

[181] S. Tec-Yam, R. Patiño and A. I. Oliva, "Chemical bath deposition of CdS films on different substrate orientations," *Current Applied Physics,* vol. 11, pp. 914-920, 5, 2011.

[182] J. R. Welty, C. E. Wicks, R. E. Wilson and G. L. Rorrer, *Fundamentals of Momentum, Heat, and Mass Transfer.* Wiley, 2008.

[183] B. R. Munson, D. F. Young and T. H. Okiishi, *Fundamentals of Fluid Mechanics.* Wiley, 2002.

[184] R. Wang, H. Lin, S. Chen, Y. Lai and M. Huang, "Boundary layer-assisted chemical bath deposition of well-aligned ZnO rods on Si by a one-step method," *Applied Physics A: Materials Science & Processing,* vol. 96, pp. 775-781, 2009.

[185] R. C. Weast, Ed., *Handbook of Chemistry and Physics.* CRC Press, 1988.

[186] M. Froment, M. C. Bernard, R. Cortes, B. Mokili and D. Lincot, "Study of CdS Epitaxial Films Chemically Deposited from Aqueous Solutions on InP Single Crystals," *J. Electrochem. Soc.,* vol. 142, pp. 2642-2649, 1995.

[187] J. Lee and T. Tsakalakos, "Influences of growth conditions on physical, optical properties, and quantum size effects of CdS nanocluster thin films," *Nanostructured Materials,* vol. 8, pp. 381-398, 7, 1997.

[188] X. L. Tong, D. S. Jiang, W. B. Hu, Z. M. Liu and M. Z. Luo, "The comparison between CdS thin films grown on Si(111) substrate and quartz substrate by femtosecond pulsed laser deposition," *Applied Physics A: Materials Science & Processing,* vol. 84, pp. 143-148, 2006.

[189] J. R. Molina-Contreras, C. Medina-Gutiérrez, C. Frausto-Reyes, R. Trejo-Vázquez, F. J. Villalobos-Piña, G. Romo-Luevano and S. Calixto, "Surface dependent behaviour of CdS LO-phonon mode," *J. Phys. D,* vol. 40, pp. 4922, 2007.

[190] S. Adachi, *Optical Constants of Crystalline and Amorphous Semiconductors: Numeric Data and Graphical Information.* Kluwer Academic Publishers, 1999.

[191] P. E. J. Flewitt and R. K. Wild, *Grain Boundaries: Their Microstructure and Chemistry.* Wiley, 2001.

BIOGRAPHICAL INFORMATION

Mehmet Eray Erkan was born on August 23, 1979 in İstanbul, Turkey. He grew up in Karadeniz Ereğli, Zonguldak located near the Black Sea in Northern Turkey. After graduating from Türk Eğitim Derneği (TED, Turkish Education Association) High School, he moved to İstanbul for his college education. He earned his B.S. (2002) and M.S. (2005) degrees from Yıldız Technical University (YTU) in Metallurgical Engineering and Materials, respectively. After attending to the Ph.D. program at YTU for less than a year, he arrived at the Materials Science and Engineering (MSE) Department at the University of Texas at Arlington (UTA) in August 2006. He worked in an industry-funded project on aqueous corrosion of aluminum alloys at Dr. Pranesh B. Aswath's Tribology, Lubrication and Coating Laboratory for two years. The project he worked on was ended due to short funding at the beginning of 2009 and he needed to join to another research group at UTA. After spending around a semester at Dr. Kytai T. Nguyen's laboratory at the Bioengineering Department at UTA and getting hands-on experience on synthesis of materials used in drug delivery systems, such as polymer and magnetic nanoparticles, he joined to Dr. Michael H.-C. Jin's Photovoltaic Materials Laboratory (PVML) at MSE Department at UTA in August 2009. His work at PVML was on chalcopyrite thin film solar cells. He worked on all fabrication steps of chalcopyrite thin film solar cells. Apart from contributing to the routine work done on solar cell fabrication at the PVML, he worked on three different projects over the course of the time he was at PVML which are presented in this dissertation. After graduation, he would like to continue his research career in photovoltaic materials field.